Theory, Modelling, and Applications of Advanced Electromagnetic Materials

Ph.D Thesis

Submitted in partial fulfillment of the requirements of the
Degree of Doctor of Philosophy from the
Queen Mary University of London, London, United Kingdom

by

Majid Naeem
School of Electronic Engineering and Computer Science

April 11, 2017

I, Majid Naeem, confirm that the research included within this thesis is my own work or that where it has been carried out in collaboration with, or supported by others, that this is duly acknowledged below and my contribution indicated. Previously published material is also acknowledged below.

I attest that I have exercised reasonable care to ensure that the work is original, and does not to the best of my knowledge break any UK law, infringe any third partys copyright or other Intellectual Property Right, or contain any confidential material.

I accept that the College has the right to use plagiarism detection software to check the electronic version of the thesis.

I confirm that this thesis has not been previously submitted for the award of a degree by this or any other university.

Signature:

Date:

Details of collaboration and publications:

Journal Papers

1. M. Naeem and Yang Hao, Controlling electromagnetic waves using composites employing high-Q or plasmonic scatterers, scientific reports, (Ready for publication)

2. Naeem M & Hao Y: Homogenization of composites using full-wave point-dipole model. EPJ Appl. Metamat. 2016, 3, 6.

3. B Wu, HM Tuncer, M Naeem, B Yang, MT Cole, WI Milne, Y Hao, Experimental demonstration of a transparent graphene millimetre wave absorber with 28% fractional bandwidth at 140 GHz, Scientific Reports 4, 2014.

Conference Papers

1. M. Naeem, T. M. McManus and Y. Hao, A generalized dipole moment based approach for modelling of nanoparticles," The 30th International Review of Progress in Applied Computational Electromagnetics, 23-27 mar. 2014.

2. M. Naeem, T. M. McManus and Y. Hao, An Overview of the Generalized Dipole Moment Based Approach for Modelling of Nanoparticles," 8th International Congress on Advanced Electromagnetic Materials in Microwaves and Optics, aug. 2014.

3. Liu Y, Chen H, Naeem M, Infinite Maxwell fish-eye in a finite area. Advanced Electromagnetic Materials in Microwaves and Optics (METAMATERIALS), 2015 9th International Congress on; 2015 7-12 Sept. 2015.

Abstract

A multitude of recent work predicts many novel concepts based on the availability of non-natural materials; some prominent examples include transformation optics (TO) and perfect lens. The interest in this field has grown dramatically due to speculated possibility to allow for continuously varying material properties to steer the incident wave at will, such as for the TO. The posed challenges for their realisation include the limitations of numerical modelling and manufacturing techniques. A design scheme has been proposed, in this thesis, for composite materials: the desired electromagnetic properties of composites can be engineered by judiciously varying the volume fraction of the inclusion-to-host materials, by manipulating the geometric arrangement of inclusions, or by altering their dielectric contrast. The analysis of the homogenised response of the designed materials at macro-scale requires effective medium modelling techniques. The existing effective medium approximation techniques have been discussed, and their pros and cons outlined. A homogenization scheme has been introduced that is based on the interaction of the incident wave and the nanoparticles at the micro-scale, which further requires efficient electromagnetic modelling. The conventional nanoparticle modelling techniques, as well as the state of the art, have been reviewed and a dipole-moment-based method to efficiently solve modern nanoparticle-based electromagnetic problems has been outlined. The applicability of the proposed scheme has been demonstrated by employing it to design various EM devices. An improved permittivity extraction scheme has been proposed for the homogenization of composites. Unlike classical homogenization schemes, the extracted parameters, using the proposed technique, follow the relation between the real and imaginary parts, that is, Kramers-Kronig relations. Several random

and periodic structures have been simulated for the purpose of extracting the effective electromagnetic properties and interpreting the results so as to establish a connection between them.

Contents

1 Introduction **1**

1.1 Background 1

1.2 Challenges to Material Design and Manufacture 4

1.3 Challenges to Material Modelling 5

1.4 Organization of the Thesis 8

1.5 Summary 10

2 Review of Material Modelling **11**

2.1 Review of Existing Models 11

2.1.1 Effective Medium Approximation of Bulk Material 13

2.1.2 Effective Medium Approximation of a Metafilm 20

2.2 Dielectric Relaxation Models 21

2.2.1 Circuit-Equivalent Models 21

2.2.2 Atomistic Models 25

2.3 Kramers-Kronig Relationships 26

2.4 Summary 29

3 Oveview of EM Modelling and the Proposed 3D-Modelling Scheme 31

3.1 Brief Review of Computational Electromagnetic Methods 31

3.2 Review of Nanoparticles Modelling Techniques 34

3.3 Full-Wave Point-Dipole Method 35

3.4 The Proposed Technique for Nanoparticles Modelling 38

3.4.1 The Model 40

3.4.2 Numerical Results & Discussion 41

3.4.3 Surface Waves 44

3.4.4 Lens Simulation 44

3.5 Summary 47

4 Point-Dipole Method 49

4.1 Introduction 50

4.2 Mathematical Problem Formulation 50

4.2.1 The Volume Equivalence Principle 52

4.2.2 The Electric-Field Integral Equation (EFIE) 55

4.3 The Method of Weighted Residuals (MWR) 57

4.4 Choice of Basis and Testing Functions 60

4.4.1 Basis Function Selection 60

4.4.2 Selection of Weighting Functions 61

4.5 Computation of the Moment Matrix Elements 62

4.5.1 The Self-Term Z_{nn} 62

4.5.2 The Off-Diagonal Moment Matrix Term Z_{mn} $(m \neq n)$ 63

4.6 Summary 66

5 Numerical Modelling of 2D EM Materials and Material-Design Scheme **67**

5.1 The Numerical-Modelling Scheme in 2D 68

5.2 Effective Medium Approximation 71

5.3 2D Lüneburg Lens Design and Validation 75

5.4 Absorber Design using Lüneburg Lens 76

5.5 Maxwell's Fisheye Lens 79

5.6 Summary 80

6 Effective Medium Modelling Using Full-Wave Point-Dipole Method 82

6.1 Homogenization 82

6.2 Brief Description of Classic Homogenization Techniques 84

6.3 Proposed Homogenization Scheme 85

6.4 Results 87

6.4.1 Gradient Index Materials 90

6.5 Random Medium 92

6.5.1 Homogenization of Random Materials 96

6.5.2 Sample Size Consideration 96

6.6 Sphere Versus Cube 98

6.7 Summary 99

7 Applications of the Proposed Homogenisation Scheme 101

7.1 Introduction 101

7.2 Principle and design of composites 104

7.3 Result and discussions 109

7.4 Summary 112

8 Frequency Dispersion in Material's Homogenization and EM Mod-

elling **120**

8.1 Introduction 120

8.2 Dispersion in a Periodic Array of Scatterers 124

8.3 Frequency Dependent Effective Properties of Composites 128

8.4 Discussion on Frequency-Dependent MG 130

8.5 Summary 132

9 Summary and Future Work **133**

9.1 Summary 133

9.2 Key Contribution 135

9.3 Future Work 138

9.3.1 Beam Focusing Device for Energy Harvesting 139

9.3.2 Radiation Shielding Box 139

List of Figures

1.1 The state-of-the-art techniques for obtaining a cloaking design: (a) A ring resonator based design for achieving the negative refractive index [9] (b) A dielectric resonator based design for achieving the negative refractive index [7] (c) A graphical demonstration of transformation optics for a cloaking application [10]. 3

1.2 A hierarchical description of material design from modelling to applications. 6

2.1 The hierarchy describes how homogenisation can ward-off the numerical-modelling bottleneck of simulating the composite materials by representing the composite as a continuum. 13

2.2 Periodic arrangement of dielectric scatterers of constitutive parameters $(\mu_0, \varepsilon_{\mathrm{r}})$ embedded in a background medium of permittivity (μ_0, ε_0). Arrows inside the scatterers indicate the depolarization field under the application of an incident field $\boldsymbol{E}_{\mathrm{i}}$. The symbol $\boldsymbol{E}_{\mathrm{Cell}}$ represents the total field in a cubic unit-cell. 16

2.3 The Nicolsson-Ross-Weir(NRW) settings for material-parameters extraction. An equivalent signal flow graph is helpful in determining the scattering parameters. The figure is redrawn from Ref. [1]: (a) A coaxial line with an annular piece of test material (shaded area) (b) Signal flow graph of the coaxial-line scheme to extract the effective constitutive parameters of a given sample. 19

2.4 Plots (a), (b) and (c) represent the frequency dependence of real and imaginary parts of permittivity. Plots (d), (e) and (f) represent the Argand diagram of permittivity. (a) Debye (b) Cole-Cole (c) Cole-Davidson (d) Debye (e) Cole-Cole (f) Cole-Davidson. 24

2.5 Plots (a) and (b) represent the frequency dependence of real and imaginary parts of permittivity. Plots (c) and (d) represent the real versus imaginary parts of permittivity. (a) Lorentz (b) Drude (c) Lorentz (d) Drude 27

3.1 The EM scattering from a dielectric object of arbitrary shape. 35

3.2 Graphical illustration of the problem when subdivided by microcubes and CBF blocks. (a) 62361 micro-domain basis functions (b) 169 CBF-blocks, of which only 1 block is unique (c) Unique CBF-block consisting of 369 micro-domain basis. 39

3.3 Comparison between the results obtained by the Full-Wave Point-Dipole Method and COMSOL for both dielectric and metallic meta-atoms of sub-wavelength dimension at 300 MHz. The field probe line is placed perpendicular to the surface (from -0.25m to 0.25m). (a) The EM scattering from a metasurface composed of cubic meta-atoms (b) Metasurface (dielectric scatterers (c) Metasurface (metallic scatterers). 42

3.4 Comparison between the Full-Wave Point-Dipole Method and COMSOL results for electrically large dielectric and metallic spherical nanoparticles at 400 THz. The field probe line is placed 97.4 nm above the surface (from $-5.25\mu m$ to $5.25\mu m$). (a) The EM scattering from a metasurface composed of spherical meta-atoms (b) Metasurface (dielectric scatterers) (c) Metasurface (metallic scatterers). 43

3.5 Surface waves supported by an electrically large dielectric and metallic spherical nanoparticles at 400 THz. The field probe line is placed 97.4 nm above the surface (from $-5.25\mu m$ to $5.25\mu m$). (a) The EM scattering from a metasurface composed of spherical meta-atoms (b) Metasurface (dielectric scatterers) (c) Metasurface (metallic scatterers). 46

3.6 An electrically large but finite size metasurface placed perpendicular to the incident plane-wave. The surface plot depicted from $-0.7\mu m$ to $0.7\mu m$ in each dimension represents the field values. (a) The EM scattering from a metasurface composed of spherical meta-atoms (b) Electric field response of the scatters. 47

4.1 Volume equivalence principle: the presence of dielectric is incorporated in the equivalent currents present in the free space. (a) Object present (b) Object removed. 54

4.2 The microdomain basis function. 61

5.1 Selection rules for the effective permittivity modelling of a 2D material. A desired value of the effective permittivity can be achieved by using lossless dielectric wires in a host medium. Free-space is considered as the host. . . 75

5.2 A 2D Lüneburg lens validation. The relative permittivity of the wires is 4, and the loss tangent is 0. The radius of the inclusion cylinders is $\lambda/60$ and that of the lens is 4λ. The simulation frequency is 3GHz. (a) The EM scattering from a metasurface composed of spherical meta-atoms (b) The 2D Lüneburg lens simulated electric field using MEDM (c) The 2D Lüneburg lens simulated electric field (normalised) using CST by representing each discretised layer as having uniform permittivity. 77

5.3 A microwave absorber design using a random arrangement of the wire medium. The relative permittivity of the wires is 4, and the loss tangent is 5. The simulation frequency is 3GHz. The radius of the inclusion cylinders is $\lambda/60$ and that of the lens is 2λ. (a) The geometry of the 2D Lüneburg lens. The cylinders are located based on normal distribution (b) Field values of the polarisation component (i.e., z-component). 78

5.4 A 2D version of Maxwell's Fisheye lens using a random arrangement of the wire medium, where the wires were located according to a normal distribution. The relative permittivity of the wires is 8, and the loss tangent is 0. The simulation frequency is 3GHz. The radius of the inclusion cylinders is $\lambda/60$ and that of the lens is 4λ. (a) The geometry of the 2D Maxwell's Fisheye lens. The cylinders are located based on normal distribution (b) Field values of the polarisation component (i.e., z-component). 80

6.1 Effective permittivity extraction of a periodic material using various homogenization techniques. We used full wave finite element method to simulate based Nicolson Ross Weir (FEM-NRW) technique, Maxwell-Garnett (MG) periodic, MG finite along one dimension (z-direction), MG finite (finite along each direction), two scale convergence homogenization (TSCH) technique and the proposed technique (MEDM) to extract the effective parameters. A cubic sample of the composite is considered, and the full geometric and simulation settings are given in Table 6.1. (a) Effective permittivity as a function of the permittivity of the inclusion material. The lattice period d is three-times the edge-length of the basis a (b) Effective permittivity as a function of the lattice period. Relative permittivity of the inclusion is 6. 88

6.2 The effect of the finite thickness of the sample on the extracted parameters. The extracted permittivity of two-dimensional arrangement of scatterers (in good agreement for both CST and the proposed scheme) is higher than the bulk permittivity. Full geometric and simulation settings are the same as Fig. 6.1b except the single layer consideration. 89

6.3 Effective permittivity of a gradient material; lattice spacing along x- and y-directions is fixed, but variable along the z-direction. See Table 6.1 for the simulation parameters. (a) Fixed lattice spacing along x- and y-axis, but varies logarithmically along the z-direction (horizontal axis) of the Cartesian coordinate system (b) Effective permittivity of the gradient material (c) Frequency dependence of the effective permittivity layers. . . 91

6.4 Effective permittivity of a gradient material; lattice spacing along x- and y-directions is fixed, but variable along the z-direction. See Table 6.1 for the simulation parameters. (a) Fixed lattice spacing along x- and y-axis, but varies logarithmically along the z-direction (horizontal axis) of the Cartesian coordinate system (b) Effective permittivity of the gradient material (c) Frequency dependence of the effective permittivity layers. . . 93

6.5 The geometry of the cube composed of cubic meta-atoms placed in a random arrangement according to a Gaussian distribution; the volume fraction is decreasing gradually as follows: (a) 0.1, (b) 0.2, (c) 0.3. The relative permittivity of the inclusions is 6, inclusion edge-length is 30mm, and sample-cube edge-length is 750mm. 94

6.6 Computed values of absolute electric field scattered from random composites in Fig. 6.5 using the dipole averaging method. The operating frequency is 0.1GHz in each case. Absolute value of the scattered field along z-axis and passing through the centre of the cube of the following volume fractions: (a) 0.1 (b) 0.2 (c) 0.3. 95

6.7 Effective permittivity values of a random composite using the dipole averaging method. The effective permittivity values are computed over a number of random arrangements of the inclusions, and the ensemble is averaged to get the effective permittivity of the random composite. 96

6.8 Effective permittivity extraction of a random material using the Maxwell-Garnett and the method of equivalent dipole moment. A cubic sample is considered whose characteristics are given in Table 6.1. (a) Effective permittivity as a function of the permittivity of the inclusion material (b) Effective permittivity as a function of the volume fraction of inclusion-to-host (c) Effective permittivity as a function of frequency. 97

6.9 Analysis of the influence of the long distance scatterers at the test scatterer. The horizontal axis represents the increase in the edge-length of the cubic sample in terms of the edge-length of the cubic scatterer. Ten iterations were averaged to calculate each data sample. For specifications of the considered problem, see Table 6.1 98

7.1 Selection rules for the effective permittivity modelling. A desired value of the effective permittivity can be achieved by using either dielectric inclusions (in microwaves) or plasmonic inclusions (in optics). Dielectric inclusions require higher volume fraction as compared to that of plasmonic inclusions. Both the dielectric and plasmonic inclusions are considered lossless.) 105

7.2 Graded-permittivity profile of Lüneburg lens using six layers. The graded permittivity in each layer is the homogenized version of the permittivity value in the center of the layer. (a) Lüneburg lens profile using 6 discrete dielectric layers. The labeled numbers represent the effective values of the relative permittivities of the discretized rings. (b) Lüneburg lens graded-permittivity profile using six distinct composite layers. The graded permittivity in each layer is the homogenized version of the permittivity value in the center of the layer. 108

7.3 Component y of electric field values. The excitation source (a y-polarised Hertzian dipole) is placed at the focal point ($x = 0, y = 0, z = -0.18$). The diameter of the lens is 0.34m and that of the scatterers is 0.006m. The relative permittivity of the inclusion scatterers is 40. Simulation frequency is 4GHz. (a) Near electric field in $y = 0$ plane using a composite based on dielectric inclusions (using point-dipole method) (b) Near electric field in $y = 0$ plane using a composite based on plasmonic inclusion (relative permittivity of -16) (c) Near electric field of dipole (with lens) in $y = 0$ plane at 4GHz using discrete dielectric layers in CST (commercial EM software). 113

7.4 Component y of the electric-field. Dipole is placed at the focus ($x = 0, y = 0, z = -0.18$) and is polarized along y-axis. The lens is placed symmetrically at the origin of the Cartesian coordinate system. The diameter of the lens is 0.34m, and that of the scatterers is 0.006m. The relative permittivity of the scatterers is 40. (a) Dipole field (with lens) at 4GHz (b) Dipole field (with lens) at 3GHz (c) Dipole field (with lens) at 2GHz. . . . 114

7.5 Component x of electric field values. The incident plane wave is polarized along x-axis. The diameter of the lens is 0.34m, and that of the scatterers is 0.006m. (a) A plane wave incident on the lens which is placed symmetrically at the origin of the Cartesian coordinate system. The wave frequency is 4GHz (b) A plane wave incident on the lens which is placed symmetrically at the origin of the Cartesian coordinate system. The wave frequency is 3GHz (c) A plane wave incident on the lens which is placed symmetrically at the origin of the Cartesian coordinate system. The wave frequency is 2GHz. 115

7.6 Dipole gain in the presence of a microwave Lüneburg lens. The lens radius is 2λ. The inclusion scatterer radius is 0.0414λ; the inclusion relative permittivity is 37.1 and the quality factor is 5000. A y-polarized dipole is varied on the focal curve in 10 steps (from 180° to 360°) in the azimuthal plane. The design was simulated at 10GHz. The legend in the linear plot indicates the source location angle in the azimuthal plane while the source is located at the surface of the lens. (a) Labels on the outer circle indicate the ϕ variation (in degrees) in the azimuthal plane, gain labels on circles are in dB, and the gain values below 0dB have been suppressed (b) Gain (Linear plot). 116

7.7 Dipole gain in the presence of an optical Lüneburg lens. The lens radius is 1.4um. The inclusion scatterer radius is 46.5nm; the inclusion relative permittivity is -16 and the imaginary part of permittivity is 0.7033. A y-polarized dipole is varied on the focal curve in 10 steps (from 180° to 360°) in the azimuthal plane. The design was simulated at 429.8THz. The legend in the linear plot indicates the source location angle in the azimuthal plane while the source is located at the surface of the lens. (a) Labels on the outer circle indicate the ϕ variation (in degrees) in the azimuthal plane, gain labels on circles are in dB, and the gain values below 0dB have been suppressed (b) Gain (Linear plot). 117

7.8 Dipole gain (from 5.5GHz to 10GHz in 10 equal steps) in the presence of a microwave Lüneburg lens. The lens radius is fixed to 2λ at 10GHz. The inclusion scatterer radius is 0.0414λ; the inclusion relative permittivity is 37.1 and the quality factor is 5000. A y-polarized dipole is placed in the azimuthal plane at $\phi = 180°$. The variable "f" indicates the simulation frequency. 118

7.9 Dipole gain (from 350THz to 500THz in 16 equal steps) in the presence of a optical Lüneburg lens. The lens radius is fixed to 2λ at 429.8THz. The inclusion scatterer radius is 46.5nm; the inclusion relative permittivity is is calculated from the Drude model. A y-polarized dipole is placed in the azimuthal plane at $\phi = 180°$. 118

8.1 The dispersion characteristics of a three-dimensional arrangement of scatterers. The symbol k_0 denotes the free-space wavenumber and d denotes the period of the lattice. The relative permittivity of the inclusions is 20. The host medium is considered free space. (a) The EM scattering from a cubic arrangement of spherical meta-atoms in three dimensions. The radius of the inclusion is $62.03\mu m$. The lattice period is $215.44\mu m$ (b) Dispersion characteristics using the proposed analytical method, the proposed numerical method that also considers the coupling between the inclusions, the eigenvalue method presented in Ref. [120, 121], and the Maxwell-Garnett technique. 124

8.2 Frequency dependent extraction of the effective parameters of a composite composed of a periodic arrangement of scatterers. The radius of the inclusion is $62.035\mu m$; the lattice period is $215.44\mu m$, and the relative permittivity of the inclusions is 20. The matrix is free space. (a) Extracted values of the permittivity (b) Extracted values of the polarisability (c) Extracted values of the electric field inside the inclusion scatterer. 131

9.1 Theory, modelling, and applications of advanced electromagnetic materials. (a) The background of the problem has been discussed, and the material homogenization schemes have been classified based on their applications in the specified frequency regime (b) Rigorous modelling and homogenization schemes have been proposed to composite modelling and homogenization, respectively (c) The applications of the material modelling and design schemes. 136

9.2 A single layer of absorbing Lüneburg lenses stitching the periphery of the printed circuit board. For better operation of the device the separation between the lenses is less than a quarter the operating wavelenth 140

9.3 A single layer of array of absorbing 3D Lüneburg lenses. The device can absorb any polarization incident on it from any direction. It isolates the internal electronic circuitry from outside and vice versa. 140

List of Tables

2.1 General information on the applicability of the circuit equivalent (dielectric relaxation) and atomistic models. 30

3.1 Specifications of the simulated metasurfaces 45

6.1 Specifications of the simulated geometries. The superscript 3 indicates the periodicity in the three orthogonal directions; likewise for the superscript 2. Host relative permittivity is set to one in each case. $z^a \in \{178.62\ 182.16\ 189.40\ 198.45\ 211.95\ 241.70\ 263.30\ 241.70\ 211.95\ 198.45\ 189.40\ 182.16\ 178.62\}$ and $z^b \in \{228.16\ 224.44\ 216.38\ 206.71\ 194.17\ 172.77\ 158.58\ 172.77\ 194.17\ 206.71\ 216.38\ 224.44\ 228.16\}$ . . . 92

6.2 Specifications of the simulated problems. 97

Acknowledgements

My sincere gratitude goes to my supervisor Prof. Yang Hao: My thanks to him for not only providing me with the opportunity to work under his supervision but also for providing me with full financial support throughout my stay with him as a PhD student, my thanks to him for not only enlightening me with the forefront of research in scientific community but also for putting his trust in me in overcoming the challenges that the community has been facing, and my gratitude to him for timely processing of my PhD stages. His guidance and support has been real motivational force in achieving my goals.

I would like to thank Dr Khalid Rajab and Prof. Clive Parini for their expert feedback on my work, and also for providing thoughtful comments on the reports of my PhD stages.

My relationship with my colleagues in the Antenna group has been the force in motivating me throughout my PhD. So, my thanks to all of them.

List of Acronyms[1]

Acronym	Definition
CBF	Characteristic Basis Function
CBFM	Characteristic Basis Function Method
CM	Clausius-Mossoti
DC	Direct Current
DM	Dipole Moments
EM	Electromagnetic
EMA	Effective Medium Approximation
EMC	Electromagnetic Compatibility
EMI	Electromagnetic Interference
FDTD	Finite Difference Time Domain
FEM	Finite Element Method
GSTC	Generalized Sheet Transition Condition
HPBW	Half Power BeamWidth
KK	Kramer-Kronig
LHM	Left Handed Metamaterial
MEDM	Method of Equivalent Dipole Moments
MG	Maxwell-Garnett
MM	MetaMaterials

[1] Acronyms are listed alphabetically

Acronym	Definition
MoM	Method of Moments
MW	MicroWave
NRW	Nicolson Ross Wier
PCB	printed Circuit Boards
PL	Perfect lens
RWG	Rao-Wilton-Glisson
SP	Scalar Potential
SP	Scalar Potential
SVD	Singular Value Decomposition
TE	Transverse Electric
TEM	Transverse ElectroMagnetic
TM	Tranverse Magnetic
TMM	Transfer Matrix Method
TO	Transformation Optics
UDR	Universal Dielectric Response
VP	Vector Potential

Chapter 1

Introduction

Materials are the backbone of all the technological advancements reshaping our lives. A contextual background reviewing the applications requiring non-natural material properties is discussed in this chapter to justify the need for more advanced electromagnetic materials, and key challenges to overcome in engineering materials are outlined. Considering the problem size a metric, the past contribution to obtain a numerical solution to nanoparticle-based electromagnetic problems has been discussed, and different numerical modelling methods have been classified to function in specified wavelength regime. Finally, a framework of the thesis is provided.

1.1 Background

The technological marvels around us are an outcome of the centuries of progress in theory put forward by researchers and scientists in the past. The developments in the engineering techniques set us on a stimulating course to harness those discoveries to practical ends. However, many theoretical concepts still need sophisticated design techniques for their realisation; metamaterial is the one among such theoretical

concepts. Their realisation can revolutionise many walks of life including antennae, cloaking devices and lenses.

Metamaterials have been a topic of discussion since Veselago coined the term left-handed material (LHM), i.e., materials possessing negative permittivity and permeability, in 1967 [2]. More than four decades after their conception, broadband metamaterials are still limited to analytical derivations and numerical simulations, and their experimental demonstration remains hard to come by. Two major approaches to realise metamaterials are metallic resonant structures and dielectric resonant particles. These are two distinct approaches and should be discussed separately.

The first ever theoretical technique to demonstrate negative permeability at microwaves was based upon metallic sheets warped on each other in cylinders split-ring configuration. Pendry et al. [3] theoretically showed that a subwavelength array of these split-ring cylinders could be tuned to exhibit a negative permeability. The technique served as a basic building block to further research into the realisation of a negative refractive index. However, Pendry did not demonstrate negative permittivity in conjunction with permeability to manifest a negative refractive index. Taking a cue from Pendry's work, Smith et al. numerically demonstrated negative refractive index using a combination of metallic split-ring resonators and metallic rods placed at an electrically short distance but in parallel to the metallic strips [4]. Negative refractive index demonstration was revolutionary and opened up new avenues in a quest to realise broadband metamaterials or an invisible cloak, on an exciting account. Since the first demonstration of negative refractive index, a lot of research has been conducted in a bid to harness various fundamental parameters of metamaterials such as wider bandwidth, isotropy, and to overcome manufacturing limitations at optical frequencies.

The second type of metamaterials utilises the Mie-resonances of the dielectric parti-

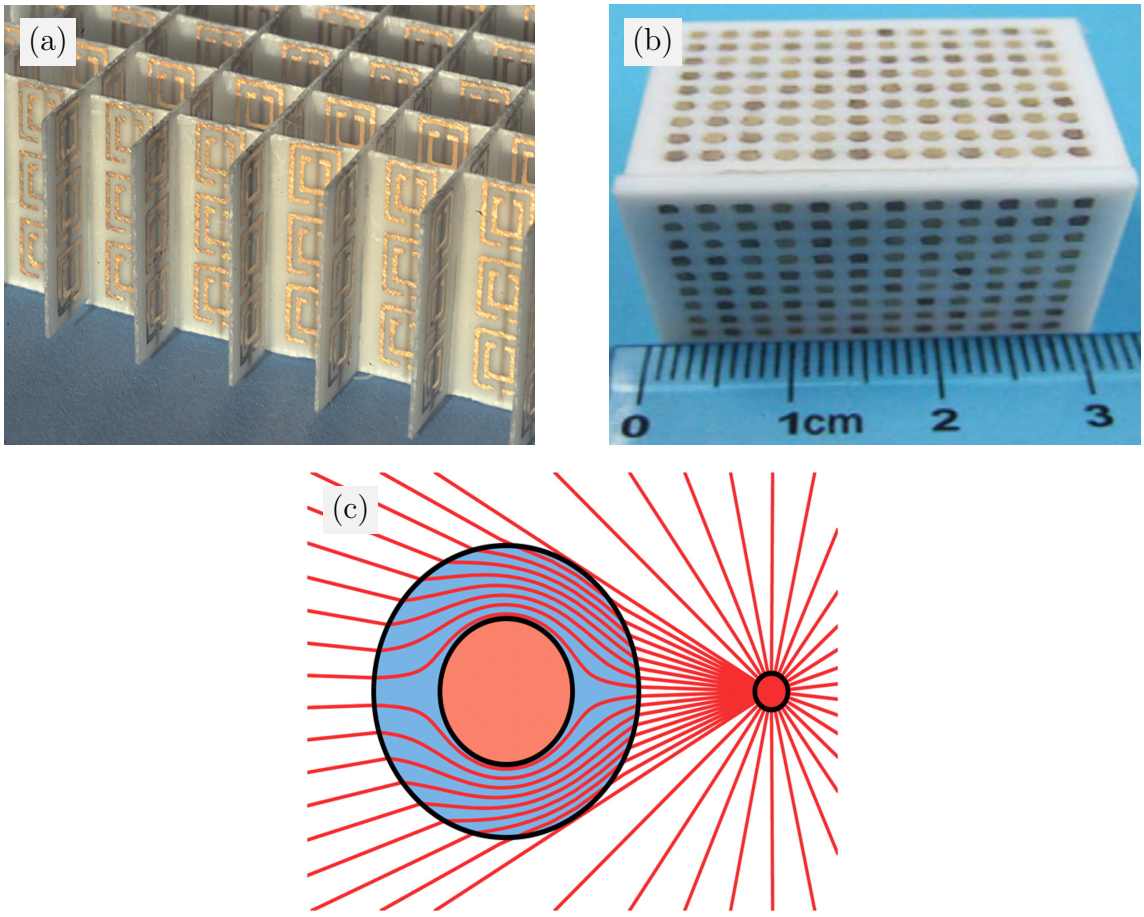

Figure 1.1: The state-of-the-art techniques for obtaining a cloaking design: (a) A ring resonator based design for achieving the negative refractive index [9] (b) A dielectric resonator based design for achieving the negative refractive index [7] (c) A graphical demonstration of transformation optics for a cloaking application [10].

cles as demonstrated by Brien [5]. The first demonstration presented negative effective permeability value only but was encouraging enough to provide a fresh impetus to achieve the goal of negative refractive index, which was experimentally demonstrated later by Zhao [6, 7]. One common phenomenon between the two variants of metamaterials discussed above is that the distance between the resonant structures is of subwavelength dimension and allows us to apply field averaging techniques to calculate the effective properties of the material under consideration [8].

The transformation optics (TO) [11, 12] is a design scheme that is used to design

intelligent materials that can guide the electromagnetic waves along the desired trajectory. Underpinning physics in the TO is lent from lens design and is different from that of the resonant structures discussed above. In this type of metamaterials, light is bent around an object along a specified trajectory, and the operation exploits the materials' electrical properties (permittivity and permeability) to achieve this. This theory was practically demonstrated in a contemporary paper by Schurig et al. [13] using an array of metallic resonators along the radial direction. A more realistic practical implementation, however, requires continuously varying electrical properties of the material, which are difficult to achieve under the current technology [14]. It would be pertinent to mention that the first demonstration of light deflection or bending by varying refractive index of the material was based on the Einstein's general theory of relativity, which served as an archetype of various advancements made in the fields of lens design and light manipulation by varying material properties. The scope of this thesis lies mainly in the design and modelling of the composites to realise TO-based applications.

1.2 Challenges to Material Design and Manufacture

Nanomaterials have recently gained increasing popularity owing to the overwhelming interest in physical traits such as polaritons [15], Fano resonance [16], and material anisotropy, etc. Besides, some new technologies, such as metamaterials (MMs) and TO, stand in need for manipulation of material properties at the nanoscale. Silicon, which has served for long as a material prima in the electronic industry, is less attractive for the TO-based designs due to manufacturing limitations at the nanoscale. In contrast, nanomaterials allow us to manipulate material properties at the scales much less than the wavelength of operation. Various techniques are being

used to synthesise nanoparticles depending upon the application required. A recent review of the synthesis methods and limitations imposed on them by the specific applications can be found in [17].

There has been an outpouring of demand for the engineered materials recently, and there exist techniques to numerically and experimentally model them. One contribution to tune gold nanoparticle dispersion can be found in [18], while nanoparticle manufacturing techniques can be found in [17].

The key challenges considered for nanocomposites design are the following:

- The existing electromagnetic simulation software are inefficient to solve electromagnetic problems involving nanoparticles having subwavelength dimensions due to some issues such as low-frequency breakdown and increased computational cost etc.
- The niche in manufacturing nanoparticle materials need to be addressed, and techniques to mass produce nanoparticles' based materials are of great importance.
- Rigorous effective-medium-approximation techniques are required to assess the properties of the materials composed of constituent particles.

1.3 Challenges to Material Modelling

Due to increasing number of applications requiring material properties non-existent in nature (e.g., metamaterials as discussed above), the research in this field has been heightened, recently. Metallic resonance based materials are no longer on the cards due to the drawbacks discussed above. We, therefore, opt to design dielectric

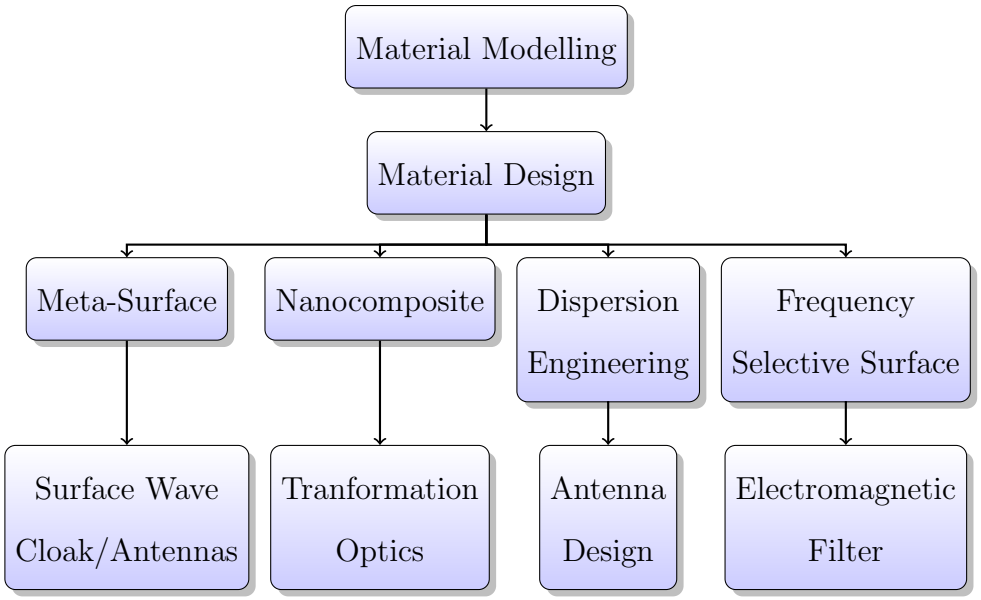

Figure 1.2: A hierarchical description of material design from modelling to applications.

materials to control the material dispersion so as to guide the incident wave (e.g., transformation optics). In principle, material properties can be tuned by manipulating the volume fraction of nanoparticles in a unit volume according to a judicial or random placement [18]. However, the understanding of the electromagnetic waves interaction with the particles, constituting material, at microscale is one of the key aspects considered for designing the materials; and this requires accurate and computationally efficient numerical modelling techniques for nanoparticles' simulation, which are far beyond reach at present.

If the electrical size of a particle-based electromagnetic problem is considered to be a metric, electromagnetic modelling techniques can be classified into the following four basic schemes:

1. **When particle radius is much larger than the mean free path of conduction electrons but much less than the operating wavelength.** This is a widely explored area in the electromagnetic modelling and has sophisti-

cated numerical methods to solve a problem of interest. Deficiency remains, however, regarding low-frequency breakdown but that can be addressed using various existing techniques [19].

2. **When particle radius is much larger than the mean free path of conduction electrons but comparable to the operating wavelength.** Standard numerical modelling methods can be used to solve problems that fall in this wavelength regime. Slow convergence can be dealt with by hybridising the modelling method with certain efficiency enhancement techniques such as fast multipole method and characteristic basis functions method.

3. **When particle radius is much larger than the mean free path of conduction electrons but much larger than the operating wavelength.** A satisfactory analytical solution in this wavelength regime would require the addition of a vast number of modes (approaching infinity) excited in the geometry. Therefore, standard numerical modelling methods would poorly converge. But ray-based numerical techniques, such as the physical theory of diffraction and geometrical theory of diffraction (extension of geometrical optics), perform efficiently under these circumstances.

4. **When nanoparticle radius is comparable to the mean free path of conduction electrons.** In this case, nanoparticle radius is comparable to the mean free path of conduction electrons and standard numerical electromagnetic techniques can not be applied directly. Instead, a modified dielectric function is derived, that phenomenologically takes finite size effects into account by increasing the damping rate of the conduction electrons that contribute to the permittivity, as [20]

$$\varepsilon(\omega) + \frac{\omega_p^2}{\omega(\omega + i\tau^{-1})} - \frac{\omega_p^2}{\omega(\omega + i\tau^{-1} + i\nu_F/R)}. \tag{1.1}$$

In the above equation ε is the bulk permittivity, ω is the operating frequency, τ^{-1} is the damping rate of conduction electrons, ν_F is the Fermi velocity, and

R is the radius of the particles. Electromagnetic modelling of materials when the operating wavelength becomes comparable to mean free path of conduction electrons is beyond the scope of this thesis and will not be discussed further.

Mean free path is the average distance travelled by a moving electron before successive collision. There exist electromagnetic modelling techniques that are applicable in a broad spectrum. However, each method outperforms in particular frequency regime and circumstances only. The deficiency, however, remains in view of computational and time complexity to solve a particle-based electromagnetic problem that is composed of a large number of the inclusion particles, be they electrically large or small. Solving for the electromagnetic scattering in a large number of particles is the primary reason to develop a new numerical modelling technique that is efficient, mainly to address particle-based problems.

1.4 Organization of the Thesis

The discussion in the forthcoming chapters is organised as follows:

- Chapter 2: This chapter discusses the classical homogenization techniques developed to date, and their applicability in the specified conditions (frequency or state of matter) is explained. Various frequency and time response based methods are described and classified according to their applicability in the frequency regime in the spectrum.

- Chapter 3: The chapter provides a brief review of electromagnetic modelling techniques and outlines the proposed method for nanoparticle simulation. The scheme to hybridise the technique with characteristic basis functions has been explained to simulate electrically large scatterers, and the results are validated

in comparison with commercial electromagnetic software.

- Chapter 4: Details of the point-dipole method used to calculate the scattering from spherical inclusions in a composite have been discussed in this chapter, and the procedure to formulate a full moment-matrix based on the proposed scheme has been explained.

- Chapter 5: A 2D-modelling scheme is proposed and validated in comparison with a commercial EM software. Also, a 2D-homogenization material-design scheme is proposed and validated, and a few applications of the schemes are outlined.

- Chapter 6: A 3D effective-medium-modelling scheme is proposed for the homogenization of both random and periodic composites. A general trend in various homogenization parameters is demonstrated.

- Chapter 7: A 3D-material-design scheme is proposed and applied to simulate a Lüneburg lens in both microwaves as well as in optics. The lens function at a broader frequency regime and various lens parameters are discussed.

- Chapter 8: In this chapter, we demonstrate the applicability of the proposed method at frequencies close to the resonances in the spherical and cubic inclusions in a composite, and we also develop a rigorous frequency-dependent homogenization scheme. Various metasurface and lens structures are simulated to demonstrate the dispersion feature of the developed method.

- Chapter 9: A summary of the thesis and key contributions are highlighted at the end of the thesis. Recommendations for the future work are also provided.

1.5 Summary

In this chapter, we discussed the background of the problem to be solved. Then we discussed the challenges that the electromagnetic community has been facing from material design, modelling, and manufacturing aspects. Considering the problem size a metric, we detailed the challenges to material modelling. Finally, an outline of the discussion in the rest of the chapters has been provided.

Chapter 2

Review of Material Modelling

Instead of simulating the quantum mechanics of the elementary particles, materials' modelling offers a simplified route to represent the material as a continuum called effective medium. We provide a brief overview of the effective-medium-approximation (EMA) techniques in a historical context. Both two- and three-dimensional materials have been covered from the effective-medium viewpoint. Also, the classical dielectric relaxation models and the physical constraints on the extracted material parameters have been described.

2.1 Review of Existing Models

Materials at the core level are composed of atoms, molecules, or ions placed randomly (as in liquids) or in a certain arrangement (as in solids), but those geometrical details can not be resolved in the visible wavelengths. This limitation is imposed by the diffraction limit of light which limits object's resolution at the level of wavelength only. Diffraction limit, however, is a general phenomenon and applies at every length scales. In this section, we will review some of the homogenization techniques

that are predominantly being used in microwave community. Under these schemes, we derive closed-form mathematical expressions to represent a heterogeneous material as a homogeneous material. Effective medium techniques have a long-standing history that dates back to 19th century, when Ottaviano-Fabrizio Mossotti analysed the relationship between the dielectric constants of two different media and Rudolf Clausius derived an explicit expression in terms of indices of refraction [21, 22]. It was a contemporary work by four scientists who claimed independent contribution and therefore is named after the quartet as Clausius-Mossotti (CM) or Lorentz-Lorenz equation. Consider a random distribution of scatterers (having equal axial ratio) with permittivity ε_{r} embedded in a background material of permittivity ε. The closed form expression for the effective permittivity of the heterogeneous material when expressed in terms of the polarizabilities of the scatterers (the CM formula) [23] can be expressed as

$$\varepsilon_{\mathrm{eff}} = \varepsilon \left[\frac{1 + \frac{2n_0\alpha^{\mathrm{p}}}{3\varepsilon}}{1 - \frac{n_0\alpha^{\mathrm{p}}}{3\varepsilon}} \right], \tag{2.1}$$

where n_0 denotes the number of scatterers per unit volume, and α^{p} denotes the polarizability of the inclusion particles, which can be expressed as

$$\alpha^{\mathrm{p}} = 3\varepsilon v_0 \left[\frac{\varepsilon_{\mathrm{r}} - \varepsilon}{\varepsilon_{\mathrm{r}} + 2\varepsilon} \right]. \tag{2.2}$$

We will discuss the pros and cons of the most popular techniques developed to date, which will highlight that even centuries of effort in this field could not take us out of the woods yet and materials and electromagnetics communities still need a rigorous method applicable to a wide range of circumstances.

The effective medium approximation (EMA) can be derived for both linear and nonlinear composites [24]. Linear composites are those materials in which there is a linear relationship between curl-free electric field and a divergence free current density or in simple terms the problem at macroscopic and microscopic scales is uncoupled. A similar analogy applies to nonlinear composites. The numerical techniques to simulate linear problems are quite mature and will be discussed in detail in

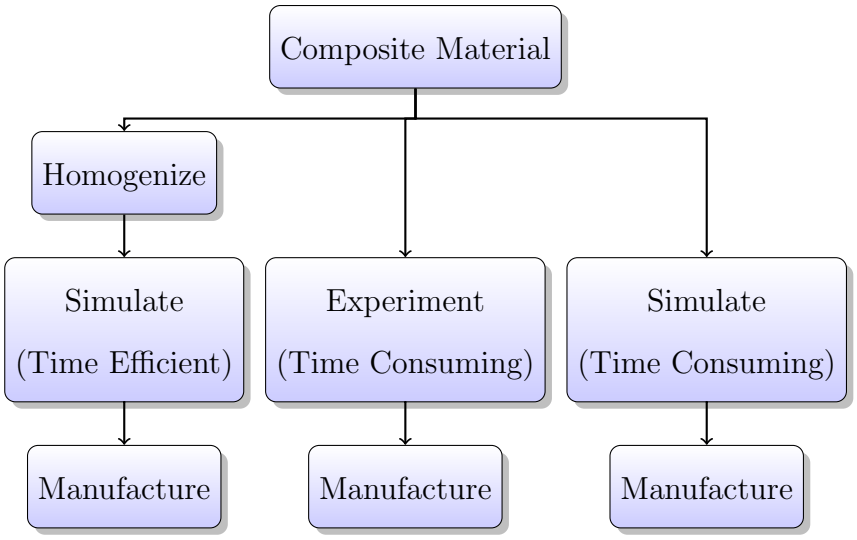

Figure 2.1: The hierarchy describes how homogenisation can ward-off the numerical-modelling bottleneck of simulating the composite materials by representing the composite as a continuum.

this chapter. However, the approximation techniques to find estimated solution to nonlinear problems are on a less firm footing and beyond the scope of this research project.

Both the CM and MG have been derived in electrostatic settings and provide reasonably accurate results when the electrical size of the inclusions is small compared to the wavelength. Other limitations of these methods include low dielectric-contrast between inclusions and host materials, and 0 dB axial-ratio of the inclusions.

2.1.1 Effective Medium Approximation of Bulk Material

One widely used type of composites is metal nanoparticles dispersed in a dielectric background medium. There exist various approximation techniques to model the electromagnetic response of this type of materials, and Maxwell-Garnett (MG) model is one of the most famous techniques to approximate this response [25]. Many

extensions to the classical MG model have been made since its inception to derive a closed form expression for non-spherical and multiphase inclusions [26, 27]. Independent of the MG work, it was Lewin who first derived analytical expressions, based on first harmonics of Mie-series, to extract the effective permittivity of a heterogeneous material composed of an arranged version of particles [28]. In the derivations, Lewin also made certain approximations such as ignoring multiple scattering between the particles and covering only the first harmonic of the scattered field. The advantage of Lewin's model over polarizability based models, such as the MG and Clausius-Mossoti, is that Lewin's model can also take into account the material losses. All the models discussed so far are limited to single phase inclusions only, viz., only one type of inclusion particles embedded in a homogeneous background medium.

In 1965 Taylor [29] extended the theory of average field approximation to deal with the lossy host or inclusion material in a composite media. Later in 1973, he introduced a generalised approach to approximate the dielectric constant of a multiphase mixture with confocal ellipsoidal spheroids [30]. Sihvola et al. [31] contributed to the topic by deriving a mixing formula for ellipsoidal scatterers immersed in a host medium. With different choices of the parameters, Sihvola showed that the result leads to various well-known approximations such as Lorentz-Lorenz formula, the Polder-van Santen formula, and the coherent potential-quasicrystalline approximation formula. Later in 1999, Sihvola summarised effective medium approximation techniques in his book [32].

A comparison of the EMA and MG theory with that of the experimental results revealed the certain critical failure of these approximations as disagreement kept on increasing with an increase in the relative density of the inclusion materials. Another critical observation was the failure of these theories as the percolation exceeded a certain threshold. Though Bruggeman's symmetrical theory is able to predict a threshold [33], it yields good results for a higher concentration of particles. Another

failure of polarizability based formulas is that they are not applicable to arrays of resonant metallic particles such as a material composed of split ring resonators and wires to render the negative refractive index. Calame proposed a finite difference-based numerical technique to simulate frequency response of conductor-insulator composites [34]. The basic theory behind the success of his technique was a percolation prevention algorithm. He later explained the work in a greater detail in Ref. [35].

Clausius-Mossoti and Maxwell-Garnett Formula

The closed-form expressions of CM and MG, discussed in the previous sections, will be derived in this section. Recall that the methods have some limitations regarding their electrical-size, dielectric-contract of inclusions to host, and the inclusions axial-ratio. Consider an infinitely large periodic arrangement of scatterers (having equal axial ratio) with permittivity ε_{r} embedded in a background material of permittivity ε_0 as illustrated in Fig. 2.2. The CM derivation assumes a fictitious cavity at the interior of a heterogeneous material: the contribution of the scatterers exterior to the cavity is calculated by integrating the contribution of the surface charges at the cavity, while the field of the interior scatterers is added one by one. The local(loc) field at the fictitious cavity is then the sum of the incident(i) field, and the field contribution by the rest of the scatterers in the background (test scatterer removed) [36]

$$\boldsymbol{E}_{\mathrm{loc}} = \boldsymbol{E}_{\mathrm{i}} + \boldsymbol{E}_{\mathrm{P}}. \tag{2.3}$$

In the case of identical inclusions, the field observed at the centre of the removed scatter, $\boldsymbol{E}_{\mathrm{loc}}$, is the sum of the fields scattered by the rest of the scatterers in the array; its value is equal to the field inside a standalone scatterer[37, 38]. The local field can thus be given as

$$\boldsymbol{E}_{\mathrm{loc}} = \boldsymbol{E}_{\mathrm{i}} + \frac{\boldsymbol{P}}{3\varepsilon_0}. \tag{2.4}$$

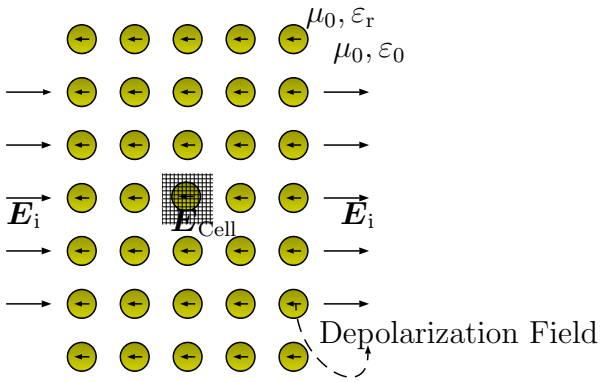

Figure 2.2: Periodic arrangement of dielectric scatterers of constitutive parameters (μ_0, ε_r) embedded in a background medium of permittivity (μ_0, ε_0). Arrows inside the scatterers indicate the depolarization field under the application of an incident field $\boldsymbol{E}_i$. The symbol $\boldsymbol{E}_{Cell}$ represents the total field in a cubic unit-cell.

The use of the above expression for the local field in the polarisation formula of the test scatterer $\boldsymbol{P} = n_0 \alpha^p \boldsymbol{E}_{loc}$ yields:

$$\boldsymbol{P} = n_0 \alpha^p \left(\boldsymbol{E}_i + \frac{\boldsymbol{P}}{3\varepsilon_0} \right), \tag{2.5}$$

where, n_0 is the number of scatterers per unit volume, and α^p is the polarizability of the inclusion particles. The above equation can be rearranged to give

$$\boldsymbol{P} = \frac{n_0 \alpha^p \boldsymbol{E}_i}{\left(1 - \frac{n_0 \alpha^p}{3\varepsilon_0}\right)}. \tag{2.6}$$

Equating Eq. 2.6 with $\boldsymbol{P} = \varepsilon_0 (\varepsilon_r - 1) \boldsymbol{E}_i$, we get

$$\frac{\varepsilon_r - 1}{\varepsilon_r + 2} = \frac{n_0 \alpha^p}{3\varepsilon_0}. \tag{2.7}$$

The above equation can further be rearranged to give a closed form expression for the effective permittivity of the heterogeneous material; expressed in terms of the polarizabilities of the scatterers, the CM equation [38] is obtained as

$$\varepsilon_{eff} = \varepsilon_0 \left[\frac{1 + \frac{2 n_0 \alpha^p}{3\varepsilon_0}}{1 - \frac{n_0 \alpha^p}{3\varepsilon_0}} \right]. \tag{2.8}$$

Notice that the CM equation suffers from the singularity for $n_0 \alpha^p / 3\varepsilon_0 = 1$, which is called the Mossotti catastrophe; this catastrophe can be dealt with by an accurate

representation of the cavity field, but the treatment would be beyond the scope of this thesis.

The difference between the MG [39] and CM is that the MG writes the effective permittivity of the heterogeneous material in terms of the constituent parameters (instead of polarizabilities) as

$$\frac{\varepsilon_{\text{eff}} - \varepsilon}{\varepsilon_{\text{eff}} + 2\varepsilon} = f\frac{\varepsilon_{\text{r}} - \varepsilon}{\varepsilon_{\text{r}} + 2\varepsilon}. \tag{2.9}$$

Field Averaging Method

Instead of averaging the polarizabilities of particles in a material as in the MG or CM relations, it is also possible to average the fields in a material; one such relation is the homogenization of periodic structures [8]. Field averaging is also an approximation approach as we ignore the higher-order Fourier harmonics in the material parameter extraction. Physically these modes correspond to the coupling with the neighbouring particles.

Nicolson-Ross-Wier (NRW) Method

The Nicolson-Ross-Wier (NRW) method was proposed to calculate the frequency domain complex permittivity and permeability of the material from time domain measurement data. Here, we will summarise the technique, for details see Ref. [1].

Consider an annular piece of test material placed in an air filled coaxial waveguide for instance [as depicted in Fig. 2.3a] at the zero phase of a uniform transverse electromagnetic (TEM) field. Suppose d be the thickness of the sample such that $z = e^{-jkd}$, where k is the propagation constant in the sample. Assuming d to be infinite in one direction, a TEM-wave E_{inc} incident at the semi-infinite interface can

be used to calculate the reflection coefficient of the medium under consideration as

$$\Gamma = \frac{Z_d - Z_0}{Z_d + Z_0} = \frac{\sqrt{\mu_R/\varepsilon_R} - 1}{\sqrt{\mu_R/\varepsilon_R} + 1}, \tag{2.10}$$

where Z_0 is the impedance of the free space, while Z_d that of the test material. Similar analogy applies to $\mu(\mu_R)$ and $\varepsilon(\varepsilon_R)$, respectively. We incorporate signal flow graph to calculate the scattering coefficients using Fig. 2.3b, which yields

$$S_{21}(\omega) = \frac{V_B}{V_{\text{inc}}} = \frac{(1+\Gamma)(1-\Gamma)z}{1-\Gamma^2 z^2} = \frac{(1-\Gamma^2)z}{1-\Gamma^2 z^2}, \tag{2.11a}$$

$$S_{11}(\omega) = \frac{V_A}{V_{\text{inc}}} = \frac{(1-z^2)\Gamma}{1-\Gamma^2 z^2}. \tag{2.11b}$$

In order to write the reflection coefficient in terms of the scattering parameters, we introduce symbols V_1 and V_2 which represent the sum and differences of the scattering coefficients, respectively; namely,

$$V_1 = S_{21} + S_{11}, \tag{2.12a}$$

$$V_2 = S_{21} - S_{11}. \tag{2.12b}$$

After certain mathematical manipulations, Γ can be written as

$$\Gamma = X \pm \sqrt{X^2 - 1}, \tag{2.13}$$

where $\pm$ is chosen such that the $|\Gamma| \leq 1$ and

$$X = \frac{1 - V_1 V_2}{V_1 - V_2}. \tag{2.14}$$

Using Eq. 2.10 along with Eq. 2.13, the extracted permittivity and permeability of the material can be calculated as

$$\varepsilon_R = \sqrt{c_1 c_2}, \tag{2.15a}$$

$$\mu_R = \sqrt{c_1} c_2. \tag{2.15b}$$

In the above equations

$$c_2 = -\left[\frac{c}{wd}\ln\left(\frac{1}{z}\right)\right]^2, \tag{2.16a}$$

$$c_1 = \left(\frac{1+\Gamma}{1-\Gamma}\right), \tag{2.16b}$$

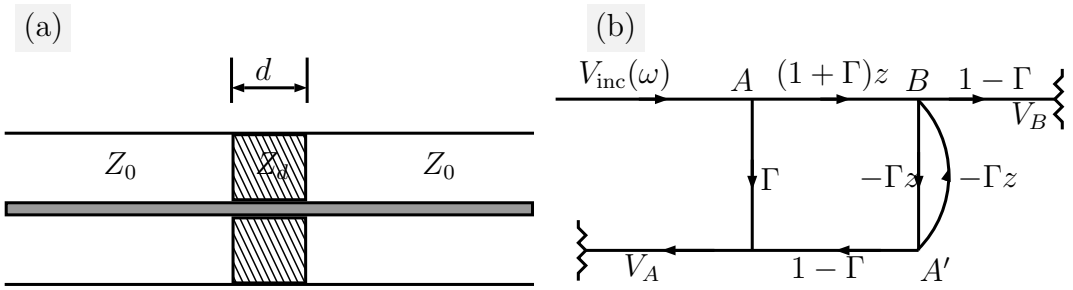

Figure 2.3: The Nicolsson-Ross-Weir(NRW) settings for material-parameters extraction. An equivalent signal flow graph is helpful in determining the scattering parameters. The figure is redrawn from Ref. [1]: (a) A coaxial line with an annular piece of test material (shaded area) (b) Signal flow graph of the coaxial-line scheme to extract the effective constitutive parameters of a given sample.

where Γ is the reflection coefficient, w is the operating frequency and c is the luminous velocity in vacuum. The procedure mentioned above can be applied to both measurements as well as numerical or analytical based extracted reflection coefficient.

- **Measurement Method** This was the first proposed technique to extract the material parameters [1]. The scattering parameters are obtained, using this method, by placing an annular piece of test material in a coaxial line connected to the input and output ports of a network analyser.

- **Simulation Method** Numerical methods discussed in Chapter 3 can be used to extract the reflection and transmission coefficients of the test material, and the extracted parameters are used in the NRW method for the extraction of the constitutive parameters of the test material.

- **Analytic Calculation** By far we have belaboured about the applicability of the effective-medium approximation for the case when the operating wavelength is much less than the dimensions of the scatterers and spacing between them. However, as long as the host medium permittivity is such that the ef-

fective wavelength is much smaller than the distance between the particles but the permittivity of the inclusion particles results in internal resonances, it is still possible to approximate the material properties by using the transfer matrix method (TMM). One such example is the bandgap photonic crystal. By expanding the field in terms of harmonics and calculating the reflection from the solution of one cylinder and doubling cylinders to calculate the reflection coefficient [5], we can use the same procedure as NRW method described above to calculate the effective material parameters.

One inherent disadvantage of the NRW approach is that it often yields nonphysical solutions at relatively higher frequencies because of the multiple scattering in the multilayer structure. The drawback is manifested while extracting the effective parameters when the sample thickness is close to the Bragg resonances of the scatters. Except for a few analytical solutions of well-defined shapes for the reflection and transmission coefficients, the extraction is usually performed using numerical computations. Effective parameters are then calculated using the closed-form expressions given in Eq. 2.15.

2.1.2 Effective Medium Approximation of a Metafilm

Metafilms–also known as metasurfaces–are considered a two-dimensional analogue of a bulk metamaterial. The term metafilm was first used by Kuester et al., [40], when they proposed the generalised sheet transition condition to extract the effective material properties of an array of two-dimensional scatterers. The method got increased popularity when it was demonstrated that such structures could also be used to exhibit negative refractive index [41, 42], which earned them the name metasurface. Later it was also found that metasurfaces support guided modes just like surface plasma on the metal-dielectric interface of a bulk material. These guided modes

were verified via numerical simulation [43]. Above mentioned is a brief overview of the topic, but a detailed description of the theory and applications of metasurfaces can be found in [44].

2.2 Dielectric Relaxation Models

On theoretical grounds and at the macroscopic level, the energy applied to a dielectric material, placed between two metallic capacitor plates, would result in storage in the form of polarisation of the dielectric molecules or ions and would also result in the dissipation of energy. It was observed that there is an intimate relation between the energy stored and lost in any dielectric material. This relation has extensively been studied in the past, but here we only mention some of the most widely accepted models. It would be pertinent to mention that each material has individual characteristics and thereby individual response, thereby, different models are needed for the characterization of each material under consideration.

2.2.1 Circuit-Equivalent Models

These models are effectively suitable for liquids that have permanent electric dipoles, such as water (H_2O) or Methanol (CH_3OH). At low frequencies the field incident on the permanent-dipoles results in the reorientation of these dipoles along the direction of the applied field yielding larger values of the depolarization fields, and thereby the response of liquids is stronger than that of the dielectric solids. As the period of the incident wave becomes comparable the relaxation time of the permanent dipoles, the dipoles can not reorient themselves in the direction of the incident field, which results in energy dissipation. The mechanism of dipoles relaxing is called dielectric relaxation and for ideal dipoles is described by classic Debye relaxation.

The dielectric response of most of the liquids can be approximated by using one of the following circuit equivalent models [32, 45]:

- Peter Debye [46] was first to model the response of a material using circuit model of a resistor and capacitor [47]. This model well describes the dielectric response of liquids which have permanent electric dipole moments such as a liquid. In the presence of an applied electric field, the liquid molecules reorient themselves in a certain amount of time. In Fourier domain, Debye relation reads

$$\varepsilon(\omega) = \varepsilon_\infty + \frac{\varepsilon_s - \varepsilon_\infty}{1 + j\omega\tau}, \tag{2.17}$$

  where τ is the relaxation time of the molecules of the liquid or solid, i.e., the time required for the dipole moments to fully respond to the applied field, or revert to the original state after removal of the applied field. And symbols ε_s and ε_∞ are hyperactivities of the material at the static and high frequency (optical). It is pertinent to mention that the Debye relaxation is an approximation under ideal circumstances and does not take into account the coupling between the dipoles. In the monograph published in 1929, Debye himself predicted the non-applicability of his model at increasingly high frequencies and very high applied field values.

- Cole represented the dielectric dispersion in the form of an Argand diagram, which showed that Debye's model looks like a semicircle in Argand diagram. Cole also verified experimentally that Debye's model was limited to certain materials, while there exist materials where Argand diagram results in a circular arc rather than a semicircle. The transition from semicircular to circular arc also results for the materials which obey Debye's model; as the temperature of the experiment is reduced, the semicircle starts to deviate from semicircular to a circular arc. This effect was accounted for in Cole-Cole equation [48]:

$$\varepsilon(\omega) = \varepsilon_\infty + \frac{\varepsilon_s - \varepsilon_\infty}{1 + (j\omega\tau)^{1-\alpha}}, \tag{2.18}$$

where $\alpha < 1$.

- Later experiments revealed some materials reveal a semicircle at low frequencies and result in a skewed arc at high frequencies of interest. Davidson and Cole [49] presented experimental proof of skewed arc in Argand diagram at high frequencies, and provided a modified Debye equation at higher frequencies.

$$\varepsilon(\omega) = \varepsilon_\infty + \frac{\varepsilon_s - \varepsilon_\infty}{(1 + j\omega\tau)^{1-\beta}}, \tag{2.19}$$

where $\beta <= 1$.

Apart from the three major dielectric relaxation models described above, a number of relaxation models have been directly or indirectly derived from them. For example, Havariliak-Negami relaxation was derived from Debye relaxation model in 1967 [50] to account for the asymmetry and broadness of the dielectric dispersion curve. This relation is given as

$$\varepsilon(\omega) = \varepsilon_\infty + \frac{\varepsilon_s - \varepsilon_\infty}{(1 + (j\omega\tau)^\alpha)^\beta}, \tag{2.20}$$

where the exponents α and β describe the asymmetry and broadness of the corresponding spectra, respectively. For $\alpha = 1$ the above equation reduces to Cole-Davidson equation, while for $\beta = 1$ it reduces to the Cole-Cole equation. There remains, however, the questions on the physical phenomenon giving rise to this anomalous behaviour. Many assumptions have been made to explain this behaviour such as the one by Calderwood [51], however, a qualitative explanation to the corresponding physics is still at large.

In 1977, Jonscher proved the universality in time and frequency responses of a variety of solids [52]. He later explained his findings in a monograph in 1983 [45], where he provided a detailed experimental evidence of the universality in both frequency and time domain for a broad range of materials. The universality he observed in the dielectric behaviour of solids is known as the universal dielectric response (UDR).

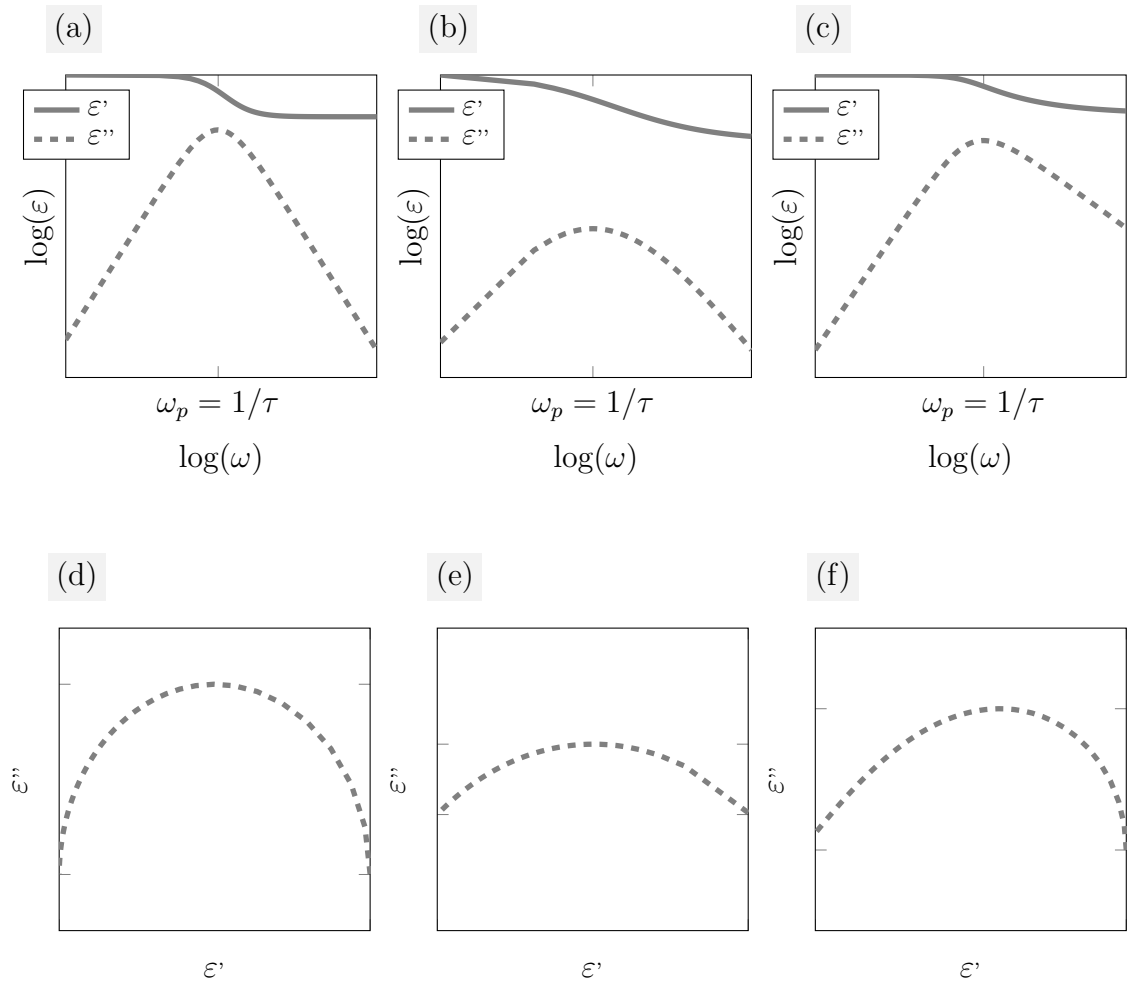

Figure 2.4: Plots (a), (b) and (c) represent the frequency dependence of real and imaginary parts of permittivity. Plots (d), (e) and (f) represent the Argand diagram of permittivity. (a) Debye (b) Cole-Cole (c) Cole-Davidson (d) Debye (e) Cole-Cole (f) Cole-Davidson.

Jonscher also proposed an approach based on many-body interactions.

A remarkable effort to characterise the dielectric and conductive properties of polymers was made by Truong [53, 54], who tried to control the dielectric properties of conducting polymer composites. In a later work, he proposed a model to describe the complex conductivity of a conducting polymer composite as a function of frequency. Another approach to estimating the electrical properties of materials was to model a composite material by a combination of resistors or capacitors connected in a network arrangement. In 2003, Almond highlighted the similarity between the near-universal dielectric response of solids and the corresponding dielectric response of solids modelled by the resistor-capacitor network [55], and later presented an experimental proof of his findings [56].

2.2.2 Atomistic Models

Circuit-Equivalent models cover only macroscopic details while effectively representing properties of a material and are applicable in a broad but low-frequency regime only. But at high frequencies, atomistic details of the material are inevitable for an accurate analysis. Here we will outline two most traditional atomistic models developed in early 20th century, i.e., Drude and Lorentz models [57]. Both models are based on the motion of electrons in different analogies constituent to each model.

- Lorentz model approximates the permittivity of the material by considering the elastic movement of the electrons that are bound to their atoms, and form dipole moments under the influence of the externally applied field. When the period of the incident wave becomes comparable to that of the atomic scale, the resonance effects arise due to the vibrations of atoms, ions, or electrons. Therefore, these processes are observed in the neighborhood of characteristic

absorption frequencies of material atoms.

$$\varepsilon(\omega) = \varepsilon_\infty + \varepsilon_0 \frac{\omega_p^2}{\omega_0^2 - \omega^2 + j\omega\nu}, \tag{2.21}$$

where ω_p and ω_0 are the plasma and resonance frequencies, respectively; while ν is the damping amplitude.

- Drude model was developed to treat the optical properties of metals and, unlike Lorentz model, considers electrons to be separated from the nuclei and free to move under an externally applied field. Drude model can be obtained from Lorentz model by setting the resonant frequency ω_0 to zero in Eq. 2.21, which gives

$$\varepsilon(\omega) = \varepsilon_\infty - \varepsilon_0 \frac{\omega_p^2}{\omega^2 - j\omega\nu}. \tag{2.22}$$

Spectral-dependent responses of Debye, Cole-Cole and Cole-Davidson models have been plotted in Fig. 2.4 for $\omega = 0.001 - 50GHz$, $\tau = 5ns$, $\varepsilon_s = 5$, and $\varepsilon_\infty = 2$. Lorentz and Drude model response is given in Fig. 2.5 for $\omega = 0.1KHz - 10THz$, $\tau = 5ns$, $\varepsilon_s = 5$, $\varepsilon_\infty = 2$, $\omega_0 = 1GHz$ and $\omega_p = 1THz$. Argand diagrams in all cases are provided to observe the loss dependent permittivity and hence carries no important information in case of nonpolarized materials such as metals (Drude model).

Table 2.1 provides general information on the applicability of each of these models. All models discussed in this Chapter are applicable under specific circumstances and in a particular frequency regime only.

2.3 Kramers-Kronig Relationships

In the previous sections, we only discussed the frequency-domain response of the material with no mention of the time domain kinematics. Herein, we discuss the

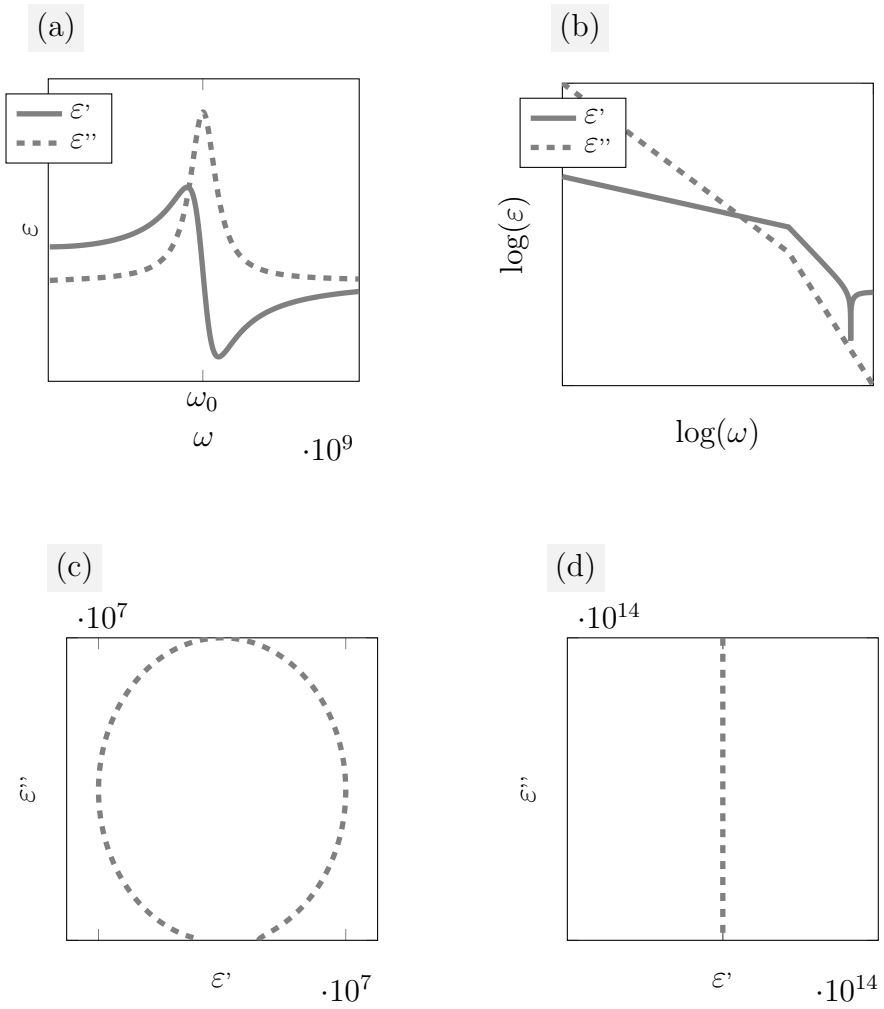

Figure 2.5: Plots (a) and (b) represent the frequency dependence of real and imaginary parts of permittivity. Plots (c) and (d) represent the real versus imaginary parts of permittivity. (a) Lorentz (b) Drude (c) Lorentz (d) Drude

time-domain response of a material and demonstrate that the causality of the constituent parameters demands that the real and imaginary parts of the constituent parameter have strong correlation; and the information about one of them [real (imaginary) part] prompts the calculation of the other [imaginary (real) part], Titchmarsh's theorem [58]. To find this relation between the real and imaginary parts of the constituent parameter, we proceed with the time domain analysis in this section. Let us consider the well-known relation between the electric field [$\boldsymbol{E}(t)$] and electric displacement field [$\boldsymbol{D}(t)$] in time-domain:

$$\boldsymbol{D}(t) = \varepsilon_0 \boldsymbol{E}(t) + \boldsymbol{P}(t), \tag{2.23}$$

where $\boldsymbol{P}(t)$ is the delayed polarisation due to the incident field as a convolution between the incident field and the dielectric response function

$$\boldsymbol{P}(t) = \varepsilon_0 \int_0^\infty \chi(\tau) \boldsymbol{E}(t-\tau) d\tau. \tag{2.24}$$

In the above equation, the response function [$\chi(t)$] can be written in the frequency domain using Fourier transform as

$$\chi(\omega) = \chi'(\omega) - i\chi''(\omega) = \int_0^\infty \chi(t) e^{-iwt} dt. \tag{2.25}$$

The above equality gives us some useful information: i) $\chi'(\omega)$ is an even function of frequency. ii) $\chi''(\omega)$ is an odd function of frequency. iii) $\chi(\omega)$ is holomorphic (analytic in the upper half plane.). Following the Titchmarsh's theorem, these conditions let us write the real and imaginary parts of the susceptibility as Hilbert transforms of each other as

$$\chi'(\omega) = \frac{1}{\pi} PV \int_{-\infty}^{\infty} \frac{\chi'(\omega')}{\omega - \omega'} d\omega', \tag{2.26a}$$

$$\chi''(\omega) = \frac{1}{\pi} PV \int_{-\infty}^{\infty} \frac{\chi''(\omega')}{\omega - \omega'} d\omega', \tag{2.26b}$$

where, PV denotes the principal-value integral. Real and imaginary parts of the susceptibility are strongly correlated, and the information about the one allows us

to calculate the other. This is an important relationship that imposes the physical constraints on the applicability of any of the homogenization scheme, be it Debye, Lorentz or Drude model. In fact, many schemes proposed in the past(famously the MG) violate the causality condition and were rectified recently so as to follow the Kramers-Kronig relations. In the subsequent chapters, we will propose a homogenisation scheme that is derived following a rigorous mathematical procedure and, thus, inherently follows the Cramers-Kronig relations.

2.4 Summary

A detailed overview of the existing material homogenization schemes has been provided in this chapter. A few traditional homogenization techniques such as Maxwell-Garnett and Nicolson-Ross-Weir methods were discussed in detail, and both 2D- and 3D-materials were discussed from material homogenization viewpoint. A few well-known dielectric relaxation models were reviewed to provide the reader with an overview of the relaxation phenomenon on the calculation of the effective permittivity of the material. For the permittivity calculations at higher frequencies, Lorentz model has been discussed, and for the calculation of the plasmonic materials (such as gold and silver) Drude model was explained. The applicability of the presented models has been explained based on the frequency spectrum and the nature of the matter such as metal, dielectric, and liquid. And a link between the real and imaginary parts of the material permittivity was explained.

Table 2.1: General information on the applicability of the circuit equivalent (dielectric relaxation) and atomistic models.

Model	Applicability	Homogenization Parameter	DC∼MWs Frequency	MWs∼Opt. Frequency	Opt.∼X-Rays Frequency
Lorentz	Dielectrics/ Metals	Permittivity	χ	χ	$\surd$
Drude	Metals	Conductivity	$\surd$	$\surd$	χ
Debye	Fluids	Permittivity	$\surd$	χ	χ
Cole-Cole	Dielectric	Permittivity	$\surd$	χ	χ
Cole-Davidson	Dielectric	Permittivity	$\surd$	χ	χ

Chapter 3

Oveview of EM Modelling and the Proposed 3D-Modelling Scheme

A review of the existing general-purpose computational electromagnetic methods as well as specific numerical techniques to solve nanoparticle-based electromagnetic problems have been discussed. A full-wave numerical modelling technique has been outlined and incorporated to simulate nanoparticle-based geometries. The proposed technique has been further demonstrated to simulate electrically large meta-atoms, a surface-based array of which results in metasurfaces.

3.1 Brief Review of Computational Electromagnetic Methods

Electromagnetic modelling of nanomaterials is a challenging task because the existing commercial software reach their limit (namely, they pose problems such as low-frequency breakdown and computational overhead of a large number of unknowns)

to model these materials composed of a large number of electrically small scatterers (predominantly spheres, spheroids or carbon nanotubes, etc.). Myriad of theories to characterise the nanomaterials have been developed, to study the bulk material interaction with microwave, each having their pros and cons. Effective medium approaches are limited to low-frequency approximations as discussed in the preceding chapter. In contrast with the Maxwell-Garnett (MG) and Clausius-Mossotti (CM) formulas, multiple scattering theories, which are applicable in the high-frequency regime, add an extra burden on the computational cost of the numerical solution. Apart from the above mentioned classical approaches, random phase approximation and generalised sheet transition conditions (GSTCs) are one of the widely known. In time-domain, a point dipole like approach to model energy transfer in a chain of periodic metal nanoparticles has been introduced by Watson et al [59]. However, the basic research to manifest properties of nanomaterials, and the efforts to devise sophisticated manufacturing techniques is still on the go; so is the research to find their applications in future miniaturised and transparent electronics. Some electronic properties of materials can be approximately expressed in a closed-form using a tight binding model [60]. The tight-binding model makes the approximation that the wave functions of the individual atoms in the lattice are localised within the first Brillouin zone of the atom and do not affect the other atoms in the lattice. Under this assumption, the allowed energy bands in a solid structure can be approximated using superposition of wave functions for isolated atoms (Floquet-Block theorem). However, under circumstances when the contribution of higher order modes is vital, a more sophisticated technique needs to be applied. Considering the need for a generalised numerical approach (applicable in wider frequency regime) and industrial manufacturing needs, we decided to add our contribution in this field.

Since the scope of existing computational methods is vast, we discuss here only a few widely recognised computational methods. A thorough exposition of these methods can be found in computational electromagnetics text books [61, 62, 63]. In short,

the most commonly applied methods are the following [64]:

- **FDTD (Finite Difference Time Domain)** [65] In this method, we discretize Maxwell's time-dependent curl equations and approximate the field solution iteratively. A few salient features of this approach include parallelizability and simplicity. However, the FDTD alone is not very attractive for solving electrically large problems or for handling slowly decaying transients due to a maximum allowable time step during each iteration needed for obtaining a stable scheme (Courant criterion), while requiring a large number of time steps at the same time to get a convergent result. The latter is also related to the algorithm stability. The method is particularly suitable for small computational domains and broadband computations.

- **FEM (Finite Element Method)** [61] The main step in this method is to set the weighted residual of Maxwell's curl equations to zero to solve for the unknown set of expansion coefficients. A couple of attractive features of this method are the ability to deal with complex structures and capacity to handle dispersive media, while a major disadvantage of a straightforward implementation is the extensive computation time and memory complexity; therefore, it is not suitable for solving the open-boundary problems. The method is frequently applied for solving mechanical as well as electromagnetic problems and is particularly suitable for small computational domains.

- **MoM (Method of Moments)** [66] In this scheme, we form a set of equations through discretizing a boundary or volume integral equation for the surface or volume current, respectively, by imposing boundary conditions on the electric and/or magnetic field. It has the ability to handle dispersive media but is not well suited for complex problems employing non-uniform media. This method is particularly suitable for simulating the open-boundary problems.

As evident from its title, the FDTD is implemented in time-domain, while FEM and MoM are used to simulate the problems in the frequency domains.

3.2 Review of Nanoparticles Modelling Techniques

Nanoparticles have garnered increased attention in recent years due to advancements in manufacturing technology and their applications in a variety of fields such as biomedicine, chemistry, physics, and engineering. Metasurfaces, created by the judicial placement of nanoparticles on a surface, are a promising application of nanoparticles due to many applications they offer including wave-guiding structures, absorbers, filters, and metamaterials. Electromagnetic modelling of metasurfaces, composed of so-called meta-atoms of nanoscale dimension, is a challenging task and has been a matter of concern in the past. The challenge being faced is that the use of conventional numerical methods to discretize a few scatterers yields an incredibly high number of unknowns (suppose N), resulting in problems surrounding storage and CPU time which scale as $\mathcal{O}(N^2)$ and $\mathcal{O}(N^3)$, respectively. The huge storage demand renders the numerical solution to the problem intractable, if not impossible. The low-frequency breakdown is another challenge that needs to be addressed while dealing with geometries of electrically small dimensions. One proposed solution is to discretize each scatterer with a dipole and use Foldy-Lax multiple-scattering approach to approximate the solution [67]. Effective medium approximation [40] is another approximation technique that is analogous to Clausius-Mossotti-Lorentz-Lorenz procedure to extract the effective material properties of a material composed of the volume fraction of small scatterers as discussed in the previous chapter. These major techniques to find the electromagnetic solution to metasurface problems have their own pros and cons and the scope of this thesis limits us from this discussion.

3.3 Full-Wave Point-Dipole Method

In this section, we outline a full-wave numerical-modelling method that is particularly suitable to simulate the nanoscale problem. The method was first introduced in [68], while its in-depth details have been discussed in Chapter 4. Figure 3.1 illustrates a dielectric object with volume $\mathcal{V}$, permittivity ε, and a permeability μ identical to that of free space, μ_0. The object is illuminated by an electromagnetic field $\boldsymbol{E}^{\mathrm{i}}$. After invoking the volume equivalence principle, the object is replaced by the surrounding medium (vacuum), while the equivalent electric current $\boldsymbol{J}_{\mathrm{eq}}$ inside the object gives rise to the originally scattered field $\boldsymbol{E}^{\mathrm{s}}(\boldsymbol{J}_{\mathrm{eq}})$, such that the field consistency condition $\boldsymbol{J}_{\mathrm{eq}} = j\omega(\varepsilon - \varepsilon_0)\boldsymbol{E}$, for $\boldsymbol{r} \in \mathcal{V}$ holds, where $\boldsymbol{E} = \boldsymbol{E}^{\mathrm{i}} + \boldsymbol{E}^{\mathrm{s}}(\boldsymbol{J}_{\mathrm{eq}})$, and

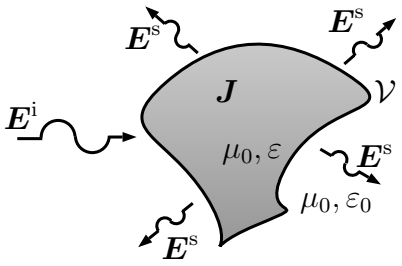

Figure 3.1: The EM scattering from a dielectric object of arbitrary shape.

$$\boldsymbol{E}^{\mathrm{s}}(\boldsymbol{r}, \boldsymbol{J}_{\mathrm{eq}}) = -j\omega\mu_0 \boldsymbol{A}(\boldsymbol{r}, \boldsymbol{J}_{\mathrm{eq}}) - \boldsymbol{\nabla}\Phi(\boldsymbol{r}, \boldsymbol{J}_{\mathrm{eq}}), \tag{3.1}$$

where $\boldsymbol{A}$ and Φ are the electric vector and scalar potentials, respectively, expressed as

$$\boldsymbol{A} = \iiint_{\mathcal{V}} G(\boldsymbol{r} - \boldsymbol{r}')\boldsymbol{J}_{\mathrm{eq}}(\boldsymbol{r}')\,\mathrm{d}V', \tag{3.2a}$$

$$\Phi = \frac{-1}{j\omega\varepsilon_0} \iiint_{\mathcal{V}} G(\boldsymbol{r} - \boldsymbol{r}')\boldsymbol{\nabla} \cdot \boldsymbol{J}_{\mathrm{eq}}(\boldsymbol{r}')\,\mathrm{d}V'. \tag{3.2b}$$

In the above equations, G is the scalar free-space Green's function given by $\exp(-jk_0|\boldsymbol{r} - \boldsymbol{r}'|)/(4\pi|\boldsymbol{r} - \boldsymbol{r}'|)$. Similar to the conventional MoM discretization, we proceed in Full-Wave Point-Dipole Method by expanding the volume-equivalent current as $\boldsymbol{J}_{\mathrm{eq}} = \sum_{n=1}^{N} I_n \boldsymbol{f}_n(\boldsymbol{r})$, where $\{\boldsymbol{f}_n\}_{n=1}^{N}$ are the N micro-basis functions,

and $\{I_n\}_{n=1}^N$ are the corresponding expansion coefficients. We use the collocation method for testing the field at the centroid $\boldsymbol{r}_m$ of the mth microcube supporting the corresponding basis function, for $m = 1, \ldots, N$. In the proposed method, the collocation method is equivalent to Galerkin's method because the field is uniform inside the basis. The testing yields the MoM matrix equation $\mathbf{V} = \mathbf{ZI}$, where

$$\begin{aligned} \mathsf{Z}_{mn} = \frac{1}{j\omega(\varepsilon - \varepsilon_0)} &\langle \boldsymbol{f}_n(\boldsymbol{r}), \hat{\boldsymbol{p}}\delta(\boldsymbol{r} - \boldsymbol{r}_m)\rangle \\ &- \langle \boldsymbol{E}^{\mathrm{s}}(\boldsymbol{f}_n(\boldsymbol{r})), \hat{\boldsymbol{p}}\delta(\boldsymbol{r} - \boldsymbol{r}_m)\rangle\,, \end{aligned} \tag{3.3a}$$

$$\mathsf{V}_m = \left\langle \boldsymbol{E}^{\mathrm{i}}, \hat{\boldsymbol{p}}\delta(\boldsymbol{r} - \boldsymbol{r}_m)\right\rangle. \tag{3.3b}$$

In the above equations, the scalar product $\langle \boldsymbol{a} \cdot \boldsymbol{b}\rangle = \iiint_{\mathcal{V}_\infty} \boldsymbol{a} \cdot \boldsymbol{b}\,\mathrm{d}V$, and $\hat{\boldsymbol{p}} \in \{\hat{\boldsymbol{x}}, \hat{\boldsymbol{y}}, \hat{\boldsymbol{z}}\}$. The choice of the polarization $\hat{\boldsymbol{p}}$ is similar to that of the micro-basis function $\boldsymbol{f}_n$. Specifically,

$$\boldsymbol{f}_n(\boldsymbol{r}) = \begin{cases} \hat{\boldsymbol{x}}, & \boldsymbol{r} \in \mathcal{V}_n, n \in \{1, \ldots, N/3\} \\ \hat{\boldsymbol{y}}, & \boldsymbol{r} \in \mathcal{V}_n, n \in \{N/3 + 1, \ldots, 2N/3\} \\ \hat{\boldsymbol{z}}, & \boldsymbol{r} \in \mathcal{V}_n, n \in \{2N/3 + 1, \ldots, N\}. \end{cases}$$

where $\mathcal{V}_n$ is the cubic support of $\boldsymbol{f}_n$ with edge length a and volume a^3.

For non-overlapping basis functions, the field $\boldsymbol{E}^{\mathrm{s}}$, generated by $\boldsymbol{f}_n$ in (3.3a) closely resembles that of the dipole. For instance, for a z-oriented dipole with dipole moment $Il = a^3$ (since we have a uniform current of unit amplitude in each microcube), the radiated electric near field at $\boldsymbol{r}_m$ becomes

$$E_x = \frac{a^3 C_{mn}}{4\pi j\omega\varepsilon_0} xz e^{-jk_0|\boldsymbol{r}_{mn}|}, \tag{3.4a}$$

$$E_y = \frac{a^3 C_{mn}}{4\pi j\omega\varepsilon_0} yz e^{-jk_0|\boldsymbol{r}_{mn}|}, \tag{3.4b}$$

$$\begin{aligned} E_z = \frac{a^3}{4\pi j\omega\varepsilon_0} &\left[C_{mn} z^2 + \frac{k_0^2}{|\boldsymbol{r}_{mn}|} \cdots \right. \\ &\left. - \frac{jk_0}{|\boldsymbol{r}_{mn}|^2} - \frac{1}{|\boldsymbol{r}_{mn}|^3} \right] e^{-jk_0|\boldsymbol{r}_{mn}|}, \end{aligned} \tag{3.4c}$$

where k_0 is the free-space propagation constant, ω is the angular frequency, $\boldsymbol{r}_{mn} =$

$\boldsymbol{r}_m - \boldsymbol{r}_n$, and

$$C_{mn} = -\frac{k_0^2}{|\boldsymbol{r}_{mn}|^3} + \frac{3jk_0}{|\boldsymbol{r}_{mn}|^4} + \frac{3}{|\boldsymbol{r}_{mn}|^5}. \tag{3.5}$$

The self-term Z_{nn}, for $m = n$, can be calculated analytically using the singularity-subtraction method. This can be done by expanding the dynamic part of the Green's function in terms of a Taylor-series and considering the static-term only while ignoring the higher order dynamic terms. After some mathematical manipulation, we obtain the approximation

$$\mathsf{Z}_{nn} \approx \frac{a^3}{j\omega\varepsilon_0}\left[\frac{\varepsilon}{(\varepsilon - \varepsilon_0)} - \frac{4}{\pi}\arctan\left(\frac{1}{\sqrt{3}}\right)\right]. \tag{3.6}$$

Once a well-conditioned moment-matrix equation is constructed, we can solve for the unknown expansion coefficient vector $\mathsf{I} = \mathsf{Z}^{-1}\mathsf{V}$. The matrix fill and solution times, with respective time complexities of $\mathcal{O}(N^2)$ and $\mathcal{O}(N^3)$, can be reduced significantly by using the CBFM [69].

In CBFM, the original problem is subdivided into smaller sub-blocks [see e.g. Fig. 3.2b]; each sub-block supports a higher level basis function (CBF) constructed from a lower-level group of micro-domain basis functions having predetermined fixed expansion coefficients. In CBFM, $\boldsymbol{J}_{\text{eq}}$ is therefore expanded as

$$\boldsymbol{J}_{\text{eq}}(\boldsymbol{r}) = \sum_{n=1}^{P} I_n^{\text{CBF}} \boldsymbol{J}_n^{\text{CBF}}(\boldsymbol{r}), \tag{3.7}$$

where P denotes the total number of CBFs employed for the macro-level discretisation of the problem; $\boldsymbol{J}_n^{\text{CBF}}$ represents the nth CBF and I_n^{CBF} represents the nth unknown expansion coefficient for the correspoinding CBF. Each CBF is then expanded in terms of micro-basis functions with known expansion coefficients $\{\alpha_l^n\}_{l=1}^N$, as: $\boldsymbol{J}_n^{\text{CBF}}(\boldsymbol{r}) = \sum_{l=1}^N \alpha_l^n \boldsymbol{f}_l(\boldsymbol{r})$, where most elements of the column vector $\boldsymbol{\alpha}^n = [\alpha_1^n, \ldots, \alpha_N^n]^T$ are zero, since the CBF has a local support. To determine the nonzero entries only the small-scale problem (Fig. 3.2c) is solved by illuminating it by a plane wave spectrum (PWS). A singular value decomposition (SVD) is applied on the resultant CBFs, which reduces the redundancy in CBFs. The

threshold value of the SVD determines the trade-off between the accuracy of the method and the method efficiency. The CBFs generated are independent of the incidence direction due to the application of the PWS and can be used to solve the scattering problem for multiple incident angles without the need to generate them anew for each angle. Let us introducing a sparse $N \times Q$ column-augmented matrix as follows: $\mathbf{J}_{\mathrm{CBF}} = [\boldsymbol{\alpha}^1, \ldots, \boldsymbol{\alpha}^Q]$, where Q is the total number of CBFs. By using the above sparce matrix we get the reduced moment matrix equation as follows: $\mathbf{Z}^{\mathrm{CBF}}\mathbf{I}^{\mathrm{CBF}} = \mathbf{V}^{\mathrm{CBF}}$, where

$$\mathbf{Z}^{\mathrm{CBF}} = \mathbf{J}_{\mathrm{CBF}}^{\mathrm{T}}\mathbf{Z}\mathbf{J}_{\mathrm{CBF}}, \tag{3.8a}$$

$$\mathbf{V}^{\mathrm{CBF}} = \mathbf{J}_{\mathrm{CBF}}^{\mathrm{T}}\mathbf{V}, \tag{3.8b}$$

and where the rank of Z is Q. This matrix equation can be solved rapidly for $\mathbf{I}^{\mathrm{CBF}}$ by using standard Gaussian elimination techniques.

The CBFM is a highly efficient technique to solve problems which result in same set of CBFs. For the purpose of applications in this thesis, where equal-sized particle based problems are considered which are separated apart, the CBFM results in a high accuracy as well as efficiency. However, if the sizes of the particles or their properties vary individually, the application of the method results in reduced efficiency.

3.4 The Proposed Technique for Nanoparticles Modelling

The Full-Wave Point-Dipole Method[64, 68], outlined in the previous section, can be efficiently applied to the numerical modelling of composite surfaces. The method was originally developed to calculate the dielectric scattering from arbitrarily shaped geometries with cube-shaped basis. In this thesis, we adapt the method to include the spherical basis, and employ it for the analysis of particle based composites,

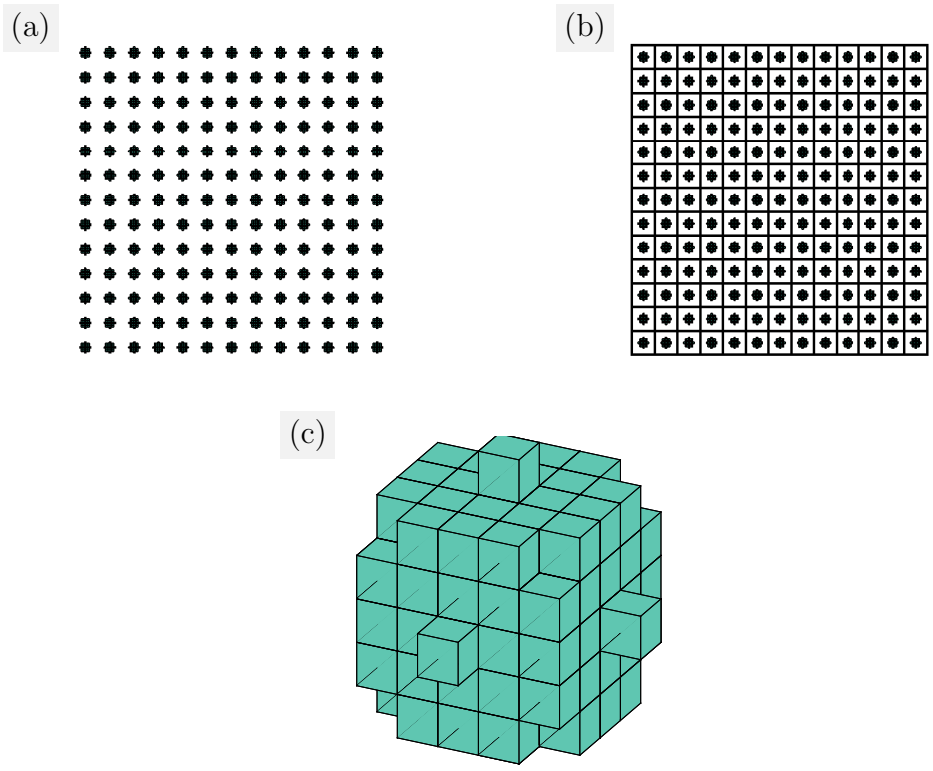

Figure 3.2: Graphical illustration of the problem when subdivided by microcubes and CBF blocks. (a) 62361 micro-domain basis functions (b) 169 CBF-blocks, of which only 1 block is unique (c) Unique CBF-block consisting of 369 micro-domain basis.

where the method yields higher accuracy because of accurate calculation of the coupling between the composite inclusions. The basis functions used are at least two orders of magnitude smaller than that of the operating wavelength which makes this technique particularly suitable for the simulation of materials composed of sub-wavelength particles. To simulate the problem at relatively high frequency (i.e., where the wavelength becomes comparable to that of the meta-atom edge-length), we further discretize each meta-atom into subdomain basis functions and invoke Characteristic Basis Function Method (CBFM)[70, 71] to overcome the storage and computational overhead of solving for a large number of unknowns. In the next section, we will elaborate the dipole moment technique in more detail and outline the CBFM method followed by a comparison with commercial software (COMSOL).

3.4.1 The Model

Let us consider a metasurface composed of discrete meta-atoms as depicted in Fig. 3.3a. We make use of the volume equivalence principle in the first step to replacing each scatterer by free-space and incorporate the effect of displacement current in an equivalent current density $\boldsymbol{J}_{\text{eq}}$. In low- and mid-frequency regimes, the Full-Wave Point-Dipole Method replaces each meta-atom with a dipole in the following analogy: when the field is incident on a particle, it displaces the electron cloud of the atoms, thereby forming a dipole moment. In contrast to the conventional numerical approaches to discretize the surface of each meta-atom using patches, the Full-Wave Point-Dipole Method represents each scatterer as one unknown.

The self-coupling term (on-diagonal term in the moment matrix) has been analytically computed using an electrostatic approximation as the field is constant in the scatterer while the coupling terms are calculated by replacing each scatterer with a dipole having an equivalent dipole moment to that of the scatterer and sensing the

field at the observation point.

Electrically large problems can be addressed by hybridising the Full-Wave Point-Dipole Method with the CBFM, whereby each meta-atom is subdivided into smaller micro-domain basis functions, and the meta-atom itself supports a higher level basis function called the Characteristic Basis Function(CBF). The CBFM needs to solve only one meta-atom, and the solution (CBF) is cloned to the rest of the meta-atoms without the loss of accuracy.

3.4.2 Numerical Results & Discussion

A metasurface composed of cubic particles arranged in a square lattice has been simulated at 300 MHz using both the Full-Wave Point-Dipole Method and COMSOL, and the overlaid results have been depicted in Figs. 3.3b and 3.3c in the case of dielectric and metallic scatterers, respectively. It is evident that both the responses agree to a good level of accuracy. The discrepancy in amplitude in between the scatterers in the metallic case is of less significant importance as this is in the immediate vicinity of the scatterers.

After validating the Full-Wave Point-Dipole Method in the microwave, we consider a metasurface composed of spherical particles arranged in a triangular lattice at the nanoscale and simulate it at 400 THz. In this case, owing to the electrically large size of the problem, it renders the meta-atom dimensions comparable to that of the operating wavelength, where the dipole moment approximation is no longer valid. Therefore, we invoke the CBFM to solve this electrically large problem. The results are compared with that of COMSOL (cf., Fig. 3.4) and are found to be in good agreement. However, the proposed method (implemented in MATLAB) required only 34 KB of storage requirement, and 4.5 minutes to simulate the dielectric metasurface (cf., Fig. 3.4c) on a desktop computer having the following specifications:

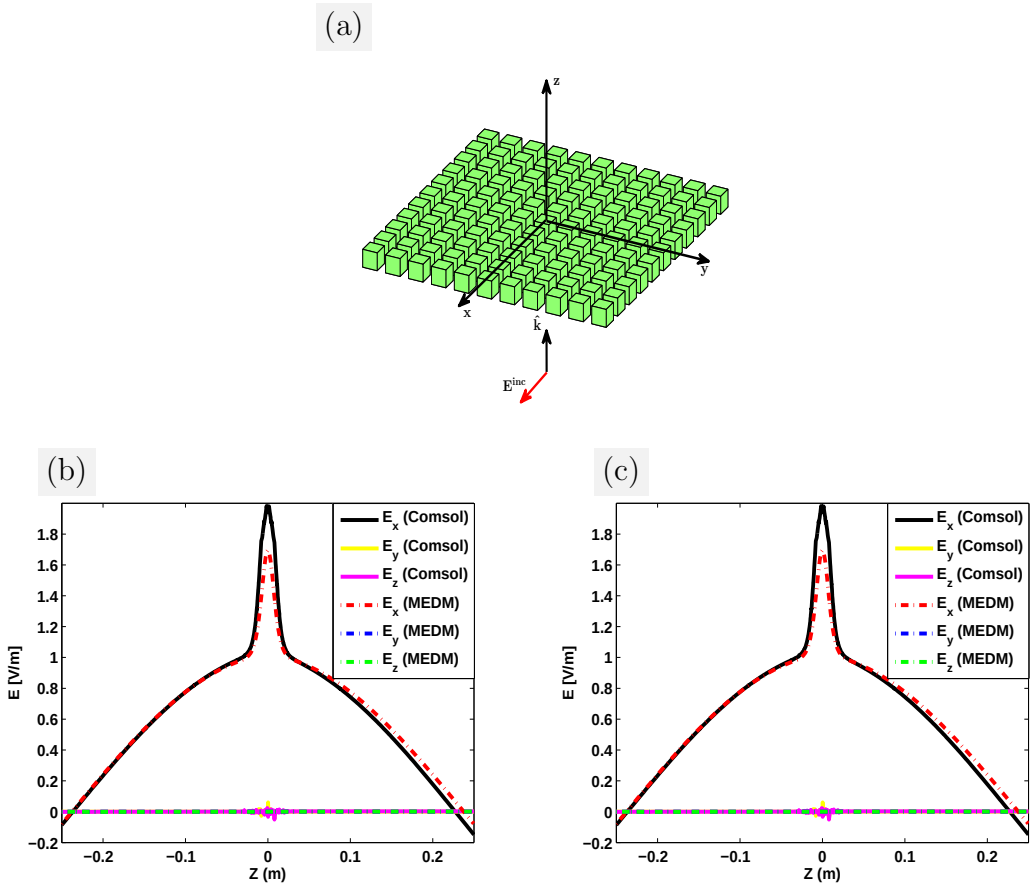

Figure 3.3: Comparison between the results obtained by the Full-Wave Point-Dipole Method and COMSOL for both dielectric and metallic meta-atoms of subwavelength dimension at 300 MHz. The field probe line is placed perpendicular to the surface (from -0.25m to 0.25m). (a) The EM scattering from a metasurface composed of cubic meta-atoms (b) Metasurface (dielectric scatterers (c) Metasurface (metallic scatterers).

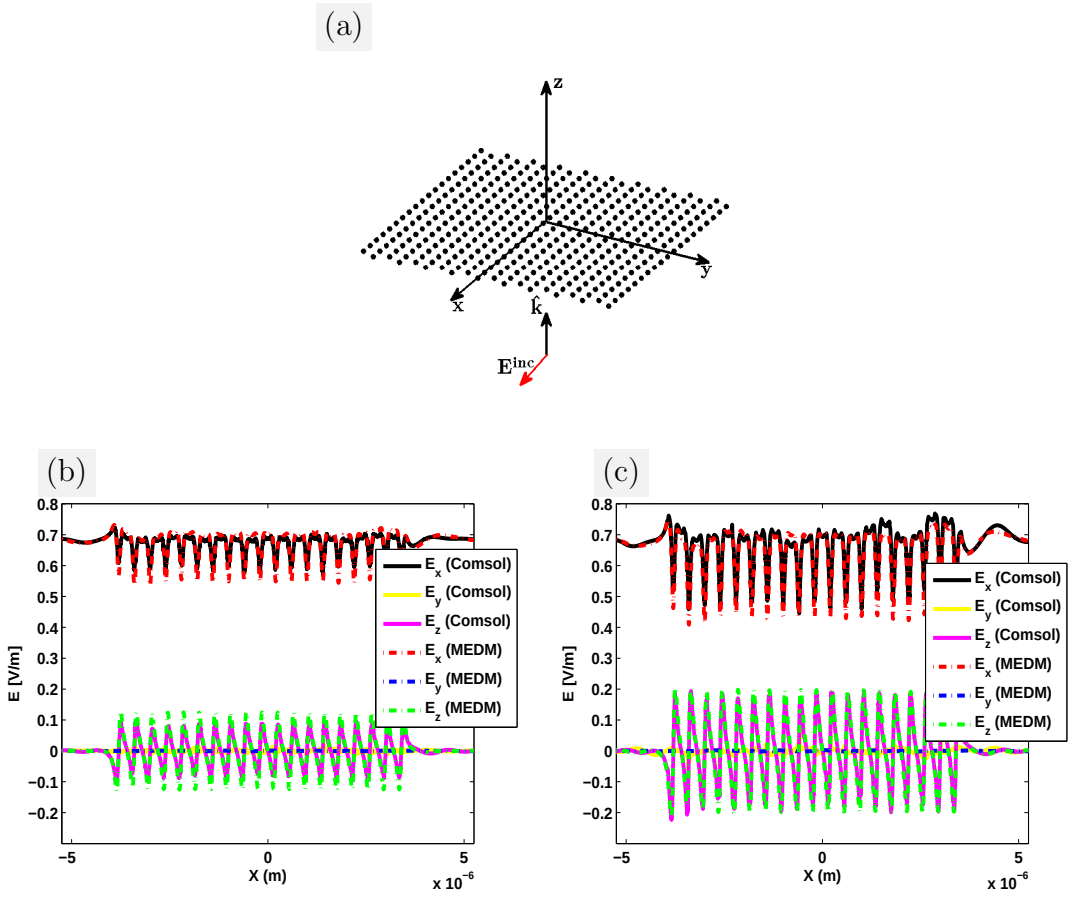

Figure 3.4: Comparison between the Full-Wave Point-Dipole Method and COMSOL results for electrically large dielectric and metallic spherical nanoparticles at 400 THz. The field probe line is placed 97.4 nm above the surface (from $-5.25\mu m$ to $5.25\mu m$). (a) The EM scattering from a metasurface composed of spherical meta-atoms (b) Metasurface (dielectric scatterers) (c) Metasurface (metallic scatterers).

CORE(TM) i7-3770CPU@3.4GHz processor and 16 GB of RAM. This is in stark contrast to that of COMSOL, where we had more than 2.7 million unknowns and the solution, using a direct solver, needed around 38 GB of RAM and 17 minutes of simulation time to solve the same problem. COMSOL simulations were done on a computer with the following specifications: XEON(R) CPU E5-4260@2.2GHz processor and 512 GB of RAM.

Table 3.1 summarises the specifications for each of the problem discussed in this section along with the problem reference. Free space permeability is assumed in all

the cases. In this section, we have demonstrated the applications of cubical and spherical objects. However, the suggested numerical approach is generalised and allows for the efficient computation of periodic structures composed of arbitrarily shaped objects such as nanorods[72] among others.

3.4.3 Surface Waves

Here we study the waves at the surface of a periodic material. In the case of interaction between an external field and the particles arranged on a surface, the interaction between the external field and the particles results in the localised surface resonance. In a surface based application where particles are excited by a plane wave incident on the plane of the surface excites localised surface waves as shown in Fig 3.5. The intensity of this resonance is vividly higher in the case of metallic spheres. A particular case of interest would be to simulate these surfaces at frequencies that result in the internal resonances in the spheres.

3.4.4 Lens Simulation

Consider again a periodic arrangement of spherical scatters but in this case two-dimensional only. The radius of the scatters is 0.00124m, and the period is 0.02559m. The relative permittivity of the sphere is 2, and the conductivity is 1.5080e+8S/m. A plane wave that is polarised in the x-direction and incident perpendicular to the plane of the scatterers has been used for the excitation. The real part of the electric field has been depicted in the $y = 0$ plane in Fig. 3.6. The field view is in two dimensions from $-0.7\mu m$ to $0.7\mu m$ in each dimension as in Fig. 3.6. As discussed in the preceding discussion, when the size of the inclusion scatters is large we can employ the CBFM that can enhance the simulation time and memory.

Table 3.1: Specifications of the simulated metasurfaces

Problem Ref.	Basis Edge-Length (m)	Basis Radius (m)	Period (m)	Permittivity (Relative)	Cond. (S)	No. of Atoms in xy-Plane
Fig. 3.3b	0.01611	N-A	0.02559	2	0	31×31
Fig. 3.3c	0.01611	N-A	0.02559	1	1×10^{8}	31×31
Fig. 3.4b	N-A	58.4×10^{-9}	400×10^{-9}	6	0	19×20
Fig. 3.4c	N-A	58.4×10^{-9}	400×10^{-9}	1	6.3×10^{7}	19×20

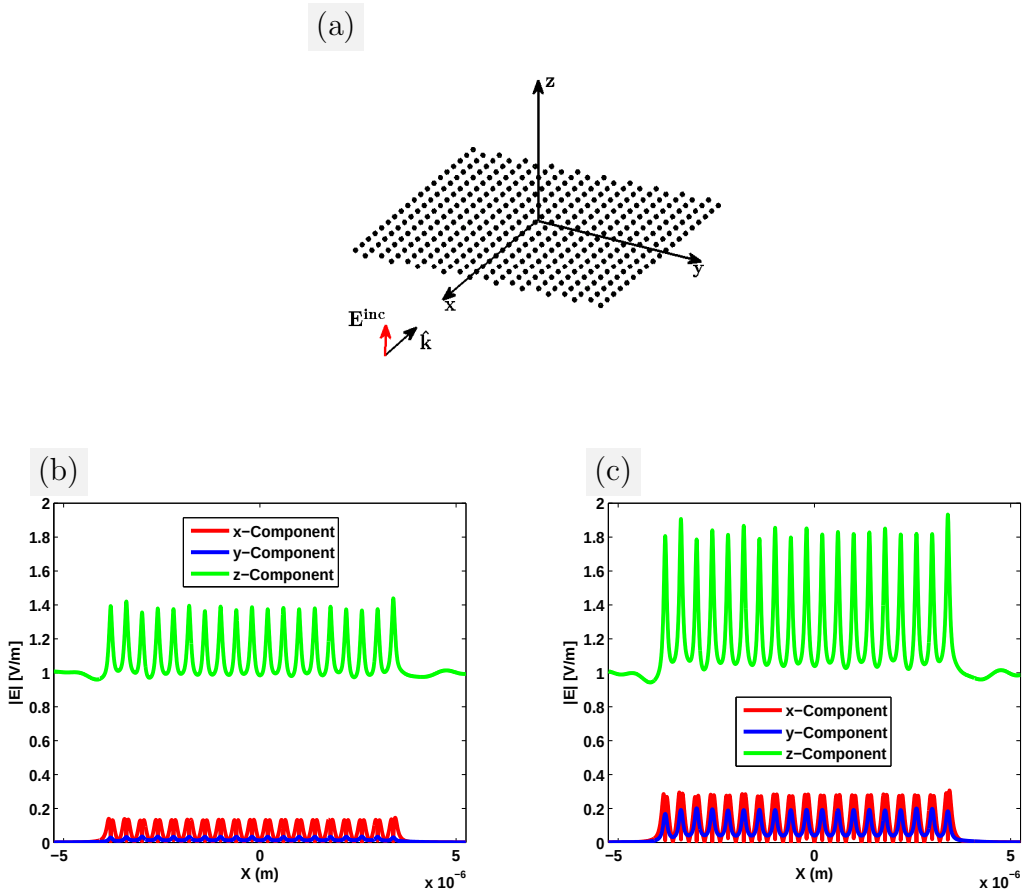

Figure 3.5: Surface waves supported by an electrically large dielectric and metallic spherical nanoparticles at 400 THz. The field probe line is placed 97.4 nm above the surface (from $-5.25\mu m$ to $5.25\mu m$). (a) The EM scattering from a metasurface composed of spherical meta-atoms (b) Metasurface (dielectric scatterers) (c) Metasurface (metallic scatterers).

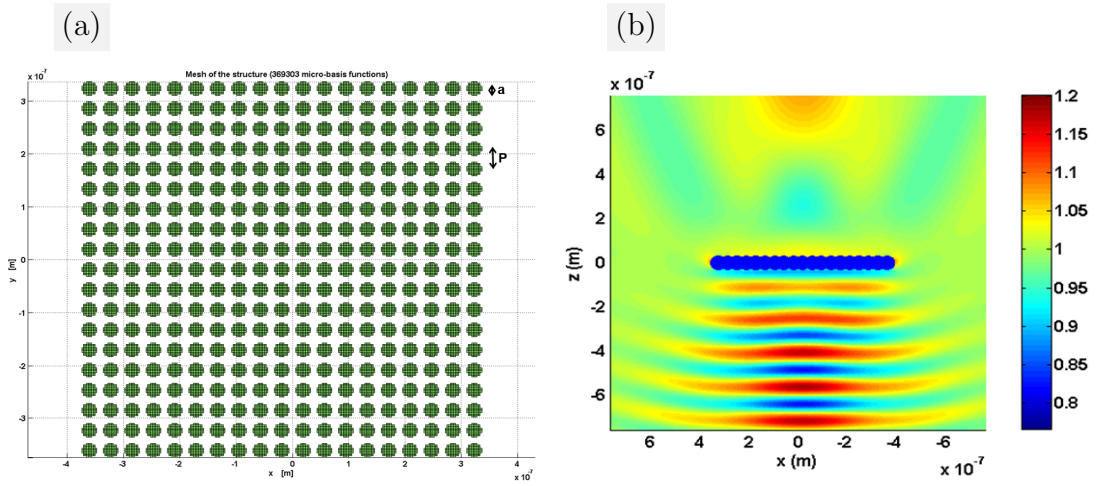

Figure 3.6: An electrically large but finite size metasurface placed perpendicular to the incident plane-wave. The surface plot depicted from $-0.7\mu m$ to $0.7\mu m$ in each dimension represents the field values. (a) The EM scattering from a metasurface composed of spherical meta-atoms (b) Electric field response of the scatters.

3.5 Summary

Traditional computational electromagnetic models have been briefly explained in this chapter. Also, the past contribution towards nanoparticle modelling schemes has been described. A dipole-moment-based method has been proposed to simulate nanoparticles by analytically subtracting the singularity in the centre of the cube, and the cross-coupling terms have been calculated by representing each scatterer as a Hertzian dipole and calculating the field radiated by it in the centres of the rest of the cubes. The procedure is repeated for each scatterer to formulate a complete moment matrix.

The dipole-moment-based method is then hybridised with a characteristic basis function method (CBFM) to solve the scattering from electrically large scatterers. The CBFM is an efficiency enhancement method that allows subdividing a given EM problem into small chunks, because of symmetries in the divided blocks only a few unique small-scale problems need to be solved. The unique subblocks are solved

through a spectrum of plane waves incident in equidistant angles isotropically. Hence the solution to each sub-block is independent of the angle of incidence. However, while simulating the scatterer-based geometries, only one CBF need to be generated. Therefore, the CBFM makes possible the accurate solution to scatter-based electrically large problems at reduced computational complexity.

Chapter 4

Point-Dipole Method

In this Chapter, we develop an in-depth mathematical formulation for the full-wave point-dipole method discussed in Chapter 3. The volume equivalence principle is invoked, and the electric field integral equation (EFIE) is formulated to determine the equivalent currents inside the dielectric volume. The EFIE is discretized through the method of weighted residuals using Galerkin's method (effectively point-matching method), which then leads to a moment matrix equation that can be solved for the unknown currents inside the discretised-elements. The selection of the basis and weighting functions in the MoM plays a key role in both the numerical solution accuracy and computational efficiency. Theoretical aspects of basis and weighting functions with a description of the restrictions on their choice are described, leading to a discussion on the implication of Galerkin and non-Galerkin moment-method approaches. The microdomain basis functions are discussed with pros and cons compared to present types of basis functions, thereby motivating our particular choice of microdomain basis functions. The self-generated field in the centre of a microdomain basis function is derived analytically as well as for the field outside of the source cube. This allows us to develop closed-form expressions for the diagonal moment matrix elements.

4.1 Introduction

In this Chapter, we will consider the scattering and the absorption of composites composed of spherical inclusions. The procedure has been discussed in Ref. [64] for scattering from arbitrarily shaped dielectrics. The problem is solved through the method-of-moments by employing micro-domain basis functions for the electric current. The support of these basis functions is one to two orders smaller in terms of wavelength than the typically employed basis functions with radius less than $\lambda/10$. The advantageous feature is that the radiated field of a micro-basis function simply equals the field of an electrically small dipole and, hence, this field can be derived in closed-form. As a result, this significantly eases the computation of the moment matrix elements since all the matrix elements, including the self-term whose field is tested inside the canonical object, can be computed analytically. To some extent, the proposed method bypasses the Green's function approach as the method employs distributed currents as basis functions as opposed to infinitely small concentrated ones. Furthermore, it does not suffer from the low-frequency breakdown problem and enables us to solve problems involving a mixture of conductor and dielectric materials with little to no modification to the formulation.

4.2 Mathematical Problem Formulation

Fig. 3.1 depicts a dielectric domain of arbitrary shape occupying a volume $\mathcal{V}$. The object is made of dielectrics with constitutive parameters $\{\mu_0, \varepsilon\}$ and is placed in free space $\{\mu_0, \varepsilon_0\}$. Furthermore, $k = \omega\sqrt{\mu_0\varepsilon}$ is the wavenumber of the interior medium. The object is illuminated by an electric field $\boldsymbol{E}^{\mathrm{i}}$ which induces an electric current $\boldsymbol{J}$ inside the object. The scattered field is denoted by $\boldsymbol{E}^{\mathrm{s}}$. Our objective is to compute the induced current inside this dielectric object, whose solution will be synthesised

indirectly by electrically small micro-basis functions. Another major advantage of taking an electrically small basis functions is that the associated radiated field can be computed in closed form. When the problem size becomes unmanageable, larger-domain basis functions can be constructed from smaller ones through a multi-level approach (the CBFM).

With reference to Fig. 3.1, the relation between the incident field $\boldsymbol{E}^{\mathrm{i}}$, the total electric current $\boldsymbol{J}$, the medium parameters ε and ε_0, and the scattered electric field $\boldsymbol{E}^{\mathrm{s}}$ is readily found from Maxwell's equations. In frequency domain, Maxwell's equations (assuming $e^{j\omega t}$ convention) for the fields and currents inside the volume $\mathcal{V}$ of homogeneously filled dielectrics are given as follows [125]:

$$\boldsymbol{\nabla} \times \boldsymbol{E} = -j\omega\mu_0 \boldsymbol{H}, \tag{4.1a}$$

$$\boldsymbol{\nabla} \times \boldsymbol{H} = \boldsymbol{J}_{\mathrm{prim}} + j\omega\varepsilon \boldsymbol{E}, \tag{4.1b}$$

$$\boldsymbol{\nabla} \cdot \boldsymbol{H} = 0, \tag{4.1c}$$

$$\boldsymbol{\nabla} \cdot \boldsymbol{E} = \rho/\varepsilon, \tag{4.1d}$$

where

$\boldsymbol{E}(\boldsymbol{r}, \omega)$ is called the electric field strength [Vm^{-1}],

$\boldsymbol{H}(\boldsymbol{r}, \omega)$ is called the magnetic field strength [Am^{-1}],

$\boldsymbol{J}_{\mathrm{prim}}(\boldsymbol{r}, \omega)$ is called the impressed electric current density [Am^{-2}],

$\boldsymbol{J} = \boldsymbol{J}_{\mathrm{prim}} + j\omega\varepsilon\boldsymbol{E}$ is called the total electric current density [Am^{-2}],

$\rho(\boldsymbol{r}, \omega)$ is called the electric charge density [Cm^{-3}].

In the equations above, we have used that the complex-valued permittivity $\varepsilon = \varepsilon_0\varepsilon_r - j\sigma/\omega$, where σ is the conductivity of the medium.

The electromagnetic properties of material are characterised through the effective permittivity and permeability of the material. The real part of the dielectric material represents the elastic response of the material, while imaginary part accounts for the loss in the material. We consider only the dielectric response here, while magnetic

response follows the same analogy. In any dielectric material, the polarisation and electron flux density are related by

$$\boldsymbol{D} = \varepsilon_0 \boldsymbol{E} + \boldsymbol{P}, \tag{4.2}$$

where

$$\boldsymbol{P} = \varepsilon_0(\chi^{(1)}\boldsymbol{E} + \chi^{(2)}\boldsymbol{E}^2 + \chi^{(3)}\boldsymbol{E}^3 + \ldots). \tag{4.3}$$

Increasing parametric order in the above equation represents the modes of polarisation of an electromagnetic wave. The first term responds linearly to the applied field while the rest of the terms represent the nonlinear responses to the applied field, and are considerable only when the excitation signal exceeds the energy binding the electrons to the atoms. We will, however, only consider the linear responses, which is given by the first term in the above expression; the material response can then wholly be represented by

$$\boldsymbol{D} = \varepsilon_0 \left(1 + \chi^{(1)}\right) \boldsymbol{E}. \tag{4.4}$$

Henceforth, we will represent the linear term $\chi^{(1)}$ without the superscript (i.e., χ).

4.2.1 The Volume Equivalence Principle

The volume equivalence principle is used here to replace the dielectric medium by vacuum, which can be done if the total current $\boldsymbol{J}$ is replaced by an equivalent current $\boldsymbol{J}_{\text{eq}}$ which is radiating in free space and gives rise to the correct scattered field $\boldsymbol{E}^{\text{s}}$ [126, pp. 327,328]. In fact, it is easily seen that the right-hand side of (4.1b) can be written as

$$\boldsymbol{J}_{\text{prim}} + j\omega\varepsilon\boldsymbol{E} = \boldsymbol{J}_{\text{prim}} + j\omega(\varepsilon - \varepsilon_0)\boldsymbol{E} + j\omega\varepsilon_0\boldsymbol{E} = \boldsymbol{J}_{\text{eq}} + j\omega\varepsilon_0\boldsymbol{E}, \tag{4.5}$$

where

$$\boldsymbol{J}_{\text{eq}} = \boldsymbol{J}_{\text{prim}} + j\omega(\varepsilon - \varepsilon_0)\boldsymbol{E} \tag{4.6}$$

is the equivalent current, which includes the primary impressed, the polarisation, and conduction currents. Upon substituting (4.5) in (4.1b), one readily observes that the equivalent current $\boldsymbol{J}_{\text{eq}}$ is radiating in free space. i.e.,

$$\boldsymbol{\nabla} \times \boldsymbol{E} = -j\omega\mu_0 \boldsymbol{H}, \tag{4.7a}$$

$$\boldsymbol{\nabla} \times \boldsymbol{H} = \boldsymbol{J}_{\text{eq}} + j\omega\varepsilon_0 \boldsymbol{E}, \tag{4.7b}$$

$$\boldsymbol{\nabla} \cdot \boldsymbol{H} = 0, \tag{4.7c}$$

$$\boldsymbol{\nabla} \cdot \boldsymbol{E} = \rho_{\text{eq}}/\varepsilon_0, \tag{4.7d}$$

where ρ_{eq} is related via the continuity equation for charges and currens as $\boldsymbol{\nabla} \cdot \boldsymbol{J}_{\text{eq}} = -j\omega\rho_{\text{eq}}$. The above equations are known as the free-space Maxwell's equations. Hence, we have removed the dielectric by incorporating its presence into the equivalent current $\boldsymbol{J}_{\text{eq}}$. This is generally referred to as the volume equivalence principle and illustrated graphically in Fig. 4.1.

In our configuration, the total electric field $\boldsymbol{E}$ is the superposition of the incident and scattered field $\boldsymbol{E}^{\text{i}}$ and $\boldsymbol{E}^{\text{s}}$, i.e., $\boldsymbol{E} = \boldsymbol{E}^{\text{i}} + \boldsymbol{E}^{\text{s}}(\boldsymbol{J}_{\text{eq}})$, where the scattered field is generated by the equivalent current $\boldsymbol{J}_{\text{eq}}$ radiating in free space. Using that $\boldsymbol{E} = \boldsymbol{E}^{\text{i}} + \boldsymbol{E}^{\text{s}}(\boldsymbol{J}_{\text{eq}})$ in (4.6), we conclude that the fields and currents inside the dielectric domain must satisfy the relation

$$\boldsymbol{J}_{\text{eq}} = \boldsymbol{J}_{\text{prim}} + j\omega(\varepsilon(\boldsymbol{r}) - \varepsilon_0)\left[\boldsymbol{E}^{\text{i}}(\boldsymbol{r}) + \boldsymbol{E}^{\text{s}}(\boldsymbol{J}_{\text{eq}})\right], \tag{4.8}$$

which is the consistency condition for the electric field and currents everywhere throughout $\mathbb{R}^3$. Assuming that the object in Fig. 4.2 has no internal sources, (4.8) simplifies to

$$\boldsymbol{J}_{\text{eq}} = j\omega(\varepsilon - \varepsilon_0)[\boldsymbol{E}^{\text{i}}(\boldsymbol{r}) + \boldsymbol{E}^{\text{s}}(\boldsymbol{J}_{\text{eq}})], \qquad \boldsymbol{r} \in \mathcal{V}. \tag{4.9}$$

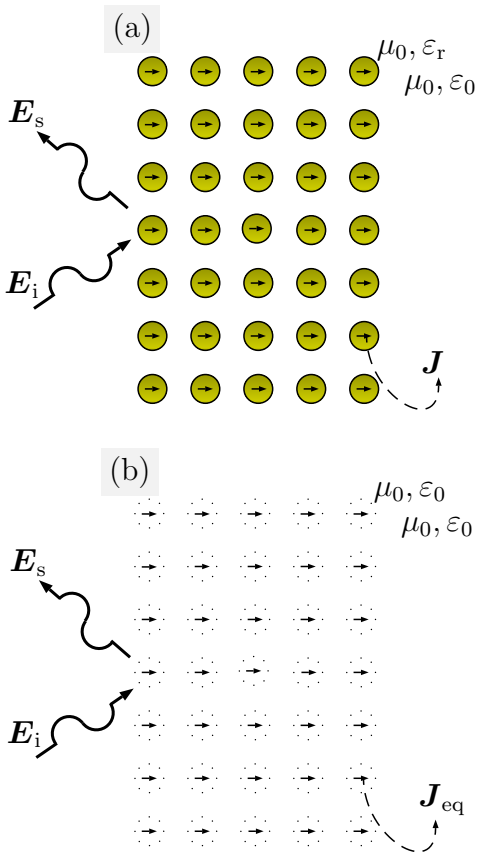

Figure 4.1: Volume equivalence principle: the presence of dielectric is incorporated in the equivalent currents present in the free space. (a) Object present (b) Object removed.

4.2.2 The Electric-Field Integral Equation (EFIE)

Equation (4.9) can be formulated as an integral equation for the unknown electric current $\boldsymbol{J}_{\text{eq}}$. To demonstrate this, we need to develop the integral representation of the scattered electric field $\boldsymbol{E}^{\text{s}}$ as a function of the current $\boldsymbol{J}_{\text{eq}}$ [127].

To this end, we proceed with (4.7a) and (4.7b) as described in [128]. Because $\boldsymbol{H}$ is solenoidal [$\boldsymbol{\nabla} \cdot \boldsymbol{H} = 0$ in (4.7)], we can express this field in terms of a magnetic vector potential $\boldsymbol{A}$, i.e.,

$$\boldsymbol{H} = \boldsymbol{\nabla} \times \boldsymbol{A}. \tag{4.10}$$

Substituting the above equation in (4.7a) and (4.7b), we get

$$\boldsymbol{\nabla} \times (\boldsymbol{E} + j\omega\mu_0 \boldsymbol{A}) = \boldsymbol{0}, \tag{4.11a}$$

$$\boldsymbol{\nabla} \times \boldsymbol{\nabla} \times \boldsymbol{A} = \boldsymbol{J}_{\text{eq}} + j\omega\varepsilon_0 \boldsymbol{E}. \tag{4.11b}$$

The curl in (4.11a) is operating on a conservative (irrotational) vector field. Hence the general solution to (4.11a) can be formulated mathematically as:

$$\boldsymbol{E} = -j\omega\mu_0 \boldsymbol{A} - \boldsymbol{\nabla}\Phi, \tag{4.12}$$

where Φ is an electric scalar potential, yet to be determined. Substituting (4.12) in (4.11b), and utilizing the vector identity $\boldsymbol{\nabla} \times \boldsymbol{\nabla} \times \boldsymbol{A} = \boldsymbol{\nabla}(\boldsymbol{\nabla} \cdot \boldsymbol{A}) - \boldsymbol{\nabla}^2 \boldsymbol{A}$, leads to the following result

$$\boldsymbol{\nabla}^2 \boldsymbol{A} + k_0^2 \boldsymbol{A} = -\boldsymbol{J}_{\text{eq}} + \boldsymbol{\nabla}(\boldsymbol{\nabla} \cdot \boldsymbol{A} + j\omega\varepsilon_0 \Phi), \tag{4.13}$$

where $k_0 = \omega\sqrt{\mu_0\varepsilon_0}$. The vector field $\boldsymbol{A}$ is defined uniquely if both its curl and divergence are specified, provided that $\boldsymbol{A}$ is known in a single point or vanishes at infinity. With reference to definition (4.10), and in view of (4.13), it is advantageous to set

$$\boldsymbol{\nabla} \cdot \boldsymbol{A} = -j\omega\varepsilon_0 \Phi, \tag{4.14}$$

which is known as Lorentz gauge. Upon substituting this result in (4.13), one arrives at the inhomogeneous Helmholtz wave equation:

$$\boldsymbol{\nabla}^2\boldsymbol{A} + k_0^2\boldsymbol{A} = -\boldsymbol{J}_{\mathrm{eq}}, \tag{4.15}$$

which can be solved for a given forcing function $\boldsymbol{J}_{\mathrm{eq}}$. The radiation condition imposed on $\boldsymbol{A}$ at infinity requires that only outward travelling wave solutions are physically possible. It can be shown that the well-known general solution to (4.15) is [129, pp. 78-80]:

$$\boldsymbol{A}(\boldsymbol{r}) = \iiint_{\mathcal{V}} G(\boldsymbol{r}-\boldsymbol{r}')\boldsymbol{J}_{\mathrm{eq}}(\boldsymbol{r}')\,\mathrm{d}V', \qquad (\boldsymbol{r} \text{ outside } \mathcal{V}), \tag{4.16}$$

with the scalar free-space Green's function $G = \exp(-jk_0R)/(4\pi R)$ and $R = |\boldsymbol{r}-\boldsymbol{r}'|$. Upon taking the divergence of (4.12), and by using (4.14) as well as that $\boldsymbol{\nabla}\cdot\boldsymbol{E} = \rho/\varepsilon_0$, one readily arrives at the inhomogeneous wave equation for the electric scalar potential, which reads as follows:

$$\boldsymbol{\nabla}^2\Phi + k_0^2\Phi = -\frac{\rho}{\varepsilon_0}, \tag{4.17}$$

and has the generic solution:

$$\Phi(\boldsymbol{r}) = \frac{1}{\varepsilon_0}\iiint_{\mathcal{V}} G(\boldsymbol{r}-\boldsymbol{r}')\rho(\boldsymbol{r}')\,\mathrm{d}V'. \tag{4.18}$$

Substituting the continuity equation $\boldsymbol{\nabla}'\cdot\boldsymbol{J}_{\mathrm{eq}}(\boldsymbol{r}') = -j\omega\rho(\boldsymbol{r}')$ in the above expression for Φ, we get:

$$\Phi(\boldsymbol{r}) = -\frac{1}{j\omega\varepsilon_0}\iiint_{\mathcal{V}} G(\boldsymbol{r}-\boldsymbol{r}')\boldsymbol{\nabla}'\cdot\boldsymbol{J}_{\mathrm{eq}}(\boldsymbol{r}')\,\mathrm{d}V'. \tag{4.19}$$

By substituting (4.19) and (4.16) in (4.12), the radiated free-space electric field $\boldsymbol{E}^{\mathrm{s}}$ is determined as:

$$\begin{aligned}\boldsymbol{E}^{\mathrm{s}}(\boldsymbol{r},\boldsymbol{J}_{\mathrm{eq}}) = -j\omega\mu_0 \iiint_{\mathcal{V}} \boldsymbol{J}_{\mathrm{eq}}(\boldsymbol{r}')\frac{e^{-jk_0|\boldsymbol{r}-\boldsymbol{r}'|}}{4\pi|\boldsymbol{r}-\boldsymbol{r}'|}\,\mathrm{d}V' \\ - \frac{1}{j\omega\varepsilon_0}\iiint_{\mathcal{V}} \boldsymbol{\nabla}'\cdot\boldsymbol{J}_{\mathrm{eq}}(\boldsymbol{r}')\boldsymbol{\nabla}'\left(\frac{e^{-jk_0|\boldsymbol{r}-\boldsymbol{r}'|}}{4\pi|\boldsymbol{r}-\boldsymbol{r}'|}\right)\mathrm{d}V'.\end{aligned} \tag{4.20}$$

The EFIE is obtained by substituting (4.20) in (4.9), i.e.,

$$\boldsymbol{J}_{\mathrm{eq}} = j\omega(\varepsilon - \varepsilon_0)\left[\boldsymbol{E}^{\mathrm{i}}(\boldsymbol{r}) - j\omega\mu_0 \iiint\limits_{\mathcal{V}} \boldsymbol{J}_{\mathrm{eq}}(\boldsymbol{r}')\frac{e^{-jk_0|\boldsymbol{r}-\boldsymbol{r}'|}}{4\pi|\boldsymbol{r}-\boldsymbol{r}'|}\,\mathrm{d}V' \right. \\ \left. -\frac{1}{j\omega\varepsilon_0}\iiint\limits_{\mathcal{V}} \boldsymbol{\nabla}'\cdot\boldsymbol{J}_{\mathrm{eq}}(\boldsymbol{r}')\boldsymbol{\nabla}'\left(\frac{e^{-jk_0|\boldsymbol{r}-\boldsymbol{r}'|}}{4\pi|\boldsymbol{r}-\boldsymbol{r}'|}\right)\mathrm{d}V'\right]. \quad (4.21)$$

The exact solution to the above equation can only be found analytically in a few cases e.g., through Wiener-Hopf techniques. However, there exist a number of numerical techniques to find the approximate solution to the EFIE in (4.21). One of those techniques is discussed in the next section.

4.3 The Method of Weighted Residuals (MWR)

The MWR is an approximation technique for solving differential and integral equations [130]. Using the MWR, an approximate solution is constructed for the current as a linear combination of known basis functions for the current with unknown expansion coefficients. These unknown coefficients can be obtained by solving a matrix equation, which is formed through testing the EFIE in (4.21) at least at an equal number of test points as the number of basis functions. The MWR can be further classified into many sub-methods depending on the choice of testing functions. Among the most well-known techniques, we mention the collocation method and Galerkin method [62].

At this moment, we proceed generally and discretize (4.21) by expanding the current $\boldsymbol{J}_{\mathrm{eq}}$ as follows [66]:

$$\boldsymbol{J}_{\mathrm{eq}} = \sum_{n=1}^{N} \alpha_n \boldsymbol{f}_n(\boldsymbol{r}), \quad (4.22)$$

where $\boldsymbol{f}_n$ are the N basis functions and $\{\alpha_n\}_{n=1}^{N}$ is the corresponding set of N expansion coefficients. Detailed mathematical studies exist for the appropriate selection

of basis and test functions for certain formulations involving integrodifferential operators [131]. A modest exposition about this can be found in detail in [126]. Herein, we only proceed with the general formalism (i.e., by not yet assuming explicit forms for the basis and test functions). Substituting (4.22) in (4.9), yields the following:

$$\begin{aligned}\boldsymbol{J}_{\mathrm{eq}} &= \sum_{n=1}^{N} \alpha_n \boldsymbol{f}_n(\boldsymbol{r}) \\ &= j\omega(\varepsilon - \varepsilon_0)\left[\boldsymbol{E}^{\mathrm{i}}(\boldsymbol{r}) + \boldsymbol{E}^{\mathrm{s}}\left(\sum_{n=1}^{N} \alpha_n \boldsymbol{f}_n(\boldsymbol{r})\right)\right] \\ &= j\omega(\varepsilon - \varepsilon_0)\left[\boldsymbol{E}^{\mathrm{i}}(\boldsymbol{r}) + \sum_{n=1}^{N} \alpha_n \boldsymbol{E}^{\mathrm{s}}(\boldsymbol{f}_n(\boldsymbol{r}))\right], \end{aligned} \tag{4.23}$$

where $\{\alpha_1, \alpha_2, \ldots, \alpha_N\}$ are the N unknown expansion coefficients to be determined. The next step is to test (4.23) at N points to get N equations with N unknowns, which we can then solve for the m^{th} test point ($m = 1, 2, \ldots, N$). In general, one can test the above EFIE over a small region, that is, in a weak form using the symmetric product, which is defined as:

$$\langle \boldsymbol{a}, \boldsymbol{b} \rangle = \iiint_{S_{\mathrm{a}} \bigcap S_{\mathrm{b}}} \boldsymbol{a} \cdot \boldsymbol{b} \, \mathrm{d}V, \tag{4.24}$$

where S_{a} and S_{b} are the supports of the basis and test or weight functions a and b, respectively. Accordingly, we get:

$$\sum_{n=1}^{N} \alpha_n \left\langle \boldsymbol{f}_n(\boldsymbol{r}), \boldsymbol{w}_m(\boldsymbol{r}) \right\rangle = j\omega(\varepsilon - \varepsilon_0)\left[\left\langle \boldsymbol{E}^{\mathrm{i}}(\boldsymbol{r}), \boldsymbol{w}_m(\boldsymbol{r}) \right\rangle + \sum_{n=1}^{N} \alpha_n \left\langle \boldsymbol{E}^{\mathrm{s}}(\boldsymbol{f}_n(\boldsymbol{r})), \boldsymbol{w}_n(\boldsymbol{r}) \right\rangle\right], \tag{4.25}$$

for $m = 1, 2, \ldots, N$. The vector function $\boldsymbol{w}_m$ is the m^{th} weighting function with support S_m and $\boldsymbol{w}_m = \boldsymbol{0}$ outside of its support. The choice of the weighting function is also very important in terms of the accuracy of the result. As mentioned above, two important choices are Galerkin's method and the point matching method. For point matching: $\boldsymbol{w}_m = \delta(\boldsymbol{r} - \boldsymbol{r}_m)$, and for Galerkin's testing: $\boldsymbol{w}_m = \boldsymbol{f}_m$. Galerkin's method is known to be more accurate and leads to a well-conditioned matrix [132]. Note that, for Galerkin's method ($\boldsymbol{w}_m = \boldsymbol{f}_m$), Eq. (4.25) leads to the matrix equa-

tion:

$$\mathbf{ZI} = \mathbf{V}, \tag{4.26}$$

where,

$$\mathsf{Z}_{mn} = \frac{1}{j\omega(\varepsilon - \varepsilon_0)} \left\langle \boldsymbol{f}_n(\boldsymbol{r}), \boldsymbol{f}_m(\boldsymbol{r}) \right\rangle - \left\langle \boldsymbol{E}^{\mathrm{s}}(\boldsymbol{f}_n(\boldsymbol{r})), \boldsymbol{f}_m(\boldsymbol{r}) \right\rangle, \tag{4.27}$$

$$\mathsf{V}_m = \left\langle \boldsymbol{E}^{\mathrm{i}}, \boldsymbol{f}_m(\boldsymbol{r}) \right\rangle. \tag{4.28}$$

Using the integral representation in (5.4), we obtain,

$$\mathsf{Z}_{mn} = \frac{1}{j\omega(\varepsilon - \varepsilon_0)} \iiint\limits_{\mathcal{V}} \boldsymbol{f}_n \cdot \boldsymbol{f}_m \, \mathrm{d}V - \iiint\limits_{\mathcal{V}} \boldsymbol{E}^{\mathrm{s}}(\boldsymbol{f}_n) \cdot \boldsymbol{f}_m \, \mathrm{d}V, \tag{4.29}$$

where the first entry in the above equation is non-zero if $\boldsymbol{f}_n$ and $\boldsymbol{f}_m$ partially overlap. We refer to the self-term in case $\boldsymbol{f}_n$ and $\boldsymbol{f}_m$ fully overlap ($m = n$). The moment matrix equation in (4.26), that is,

$$\begin{bmatrix} \mathsf{Z}_{11} & \cdots & \mathsf{Z}_{1N} \\ \vdots & \ddots & \vdots \\ \mathsf{Z}_{N1} & \cdots & \mathsf{Z}_{NN} \end{bmatrix} \begin{bmatrix} \alpha_1 \\ \vdots \\ \alpha_N \end{bmatrix} = \begin{bmatrix} \mathsf{V}_1 \\ \vdots \\ \mathsf{V}_N \end{bmatrix}, \tag{4.30}$$

can be solved using direct Gaussian elimination techniques provided that the matrix condition number is sufficiently low to obtain a unique solution [133, Sec. 2.2.4.3]. It is important to realise that, typically, the Gaussian elimination method, or any other matrix inversion technique, has a time complexity $\mathcal{O}(N^3)$, while the filling of $\mathbf{Z}$ has complexity $\mathcal{O}(N^2)$.

The time needed to solve the equation $\mathbf{I} = \mathbf{Z}^{-1}\mathbf{V}$ can be further reduced by a number of matrix acceleration/compression techniques. A suitable technique is selected and discussed in Chapter 3.

4.4 Choice of Basis and Testing Functions

The choice of a suitable set of basis and weighting functions is dependent on both mathematical and physical requirements. The general discretization process through the MWR has been explained in previous section; hence, the next step is to select explicit mathematical formulation for the basis and weighting functions. The procedure has been described in-depth in Ref. [64], here we mention a part of the procedure only.

4.4.1 Basis Function Selection

In practice, basis functions can be classified into two types: subdomain basis functions and entire domain basis functions [126, pp. 683-689]. Subdomain basis functions are nonzero only over an electrically small part of the domain, while entire domain basis functions are nonzero over a larger or even the entire domain of the considered object. Both types of basis functions should have the ability to accurately represent or resemble the anticipated unknown function, which is the equivalent electric current $\boldsymbol{J}_{\text{eq}}$ in our case. Because entire domain basis functions of an analytical type are for specific structures only and are difficult to use for forming a matrix equation (self-term), we choose to employ low-order subdomain basis functions. The size of these subdomain basis functions needs to be chosen small enough to approximate the solution with sufficiently high accuracy (typically $\lambda/10$ radius length). However, we will employ so-called microdomain basis functions of radius $\ll \lambda/10$ to obtain a potentially very accurate solution. A microdomain basis function has been depicted in Fig. 4.2 and can be defined mathematically as follows:

$$\boldsymbol{f}_n(\boldsymbol{r}) = \begin{cases} \hat{\boldsymbol{x}}, & \boldsymbol{r} \in \mathcal{V}_n; n \in \{1, \ldots, N/3\} \\ \hat{\boldsymbol{y}}, & \boldsymbol{r} \in \mathcal{V}_n; n \in \{N/3+1, \ldots, 2N/3\} \\ \hat{\boldsymbol{z}}, & \boldsymbol{r} \in \mathcal{V}_n; n \in \{2N/3+1, \ldots, N\}. \end{cases}$$

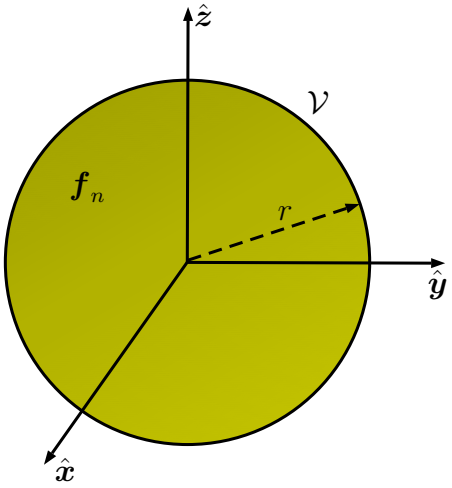

Figure 4.2: The microdomain basis function.

where $\mathcal{V}_n$ is the spherical support of $\boldsymbol{f}_n$ with constant volume $\frac{4}{3}\pi r^3$, which is equal to a cube-volume a^3 for a cube of equivalent volume with edge-length a, and $n \in \{1, \ldots, N\}$.

Although the moment matrix is larger than the case that entire-domain basis functions were to be employed, we can still solve electrically large problems by realising that entire-domain basis functions can be expanded through a fixed combination of micro-domain basis functions (using the CBFM).

4.4.2 Selection of Weighting Functions

After the discretization of the EFIE by assuming an explicit form of the basis functions, the next step in the MWR is to select the weighting functions. The appropriate choice of the weighting functions depends on the range space of the integrodifferential operator. Without justifying the choice, we will employ Galerkin's method since this option is known to yield accurate results for a large variety of problems [134]. In our case, however, we can also use the collocation method for testing the field, which is equivalent to Galerkin's method evaluated through the midpoint integration rule

(discussed in the following section).

4.5 Computation of the Moment Matrix Elements

The procedure to compute the moment matrix elements [see (5.12)] has been described in this section. In point-dipole method, we employ equal sized basis functions of low order, as a result of which the self-coupling moment matrix entries are all identical and can be computed analytically. The off-diagonal matrix elements can be computed via the dipole-moment approach as explained below.

4.5.1 The Self-Term Z_{nn}

With reference to (4.27), to compute an on-diagonal matrix element Z_{nn}, we have to evaluate

$$\mathsf{Z}_{nn} = \frac{1}{j\omega(\varepsilon - \varepsilon_0)} \langle \boldsymbol{f}_n(\boldsymbol{r}), \boldsymbol{f}_n(\boldsymbol{r}) \rangle - \langle \boldsymbol{E}^{\mathrm{s}}(\boldsymbol{f}_n(\boldsymbol{r})), \boldsymbol{f}_n(\boldsymbol{r}) \rangle \,. \tag{4.31}$$

The first term in the above equation is evaluated analytically in this section as $\langle \boldsymbol{f}_n, \boldsymbol{f}_n \rangle = \frac{4}{3}\pi r^3$. The second term has been evaluated in Chapter 8, and can be given as:

$$\boldsymbol{E}^{\mathrm{s}}(\boldsymbol{r}, \boldsymbol{J}_{\mathrm{eq}})|_{\boldsymbol{r}=0} = \hat{\boldsymbol{z}} \left[j\omega\mu_0 \frac{r^2}{2} - \frac{1}{j\omega 3\varepsilon_0} \right]. \tag{4.32}$$

This is the final expression of the self-generated field for a z-polarised basis function current. The unit vector $\hat{\boldsymbol{z}}$ can be replaced by $\hat{\boldsymbol{x}}$ or $\hat{\boldsymbol{y}}$ as defined in Fig. 4.2 to find the field of the other polarizations.

Upon substituting (4.32) in (4.29), and by using that $\langle \boldsymbol{f}_n, \boldsymbol{f}_n \rangle = \frac{4}{3}\pi r^3$, the expression

for the self-term becomes as follows:

$$\mathsf{Z}_{nn} = \frac{4}{3}\pi r^3 \frac{1}{j\omega(\varepsilon - \varepsilon_0)} - \frac{4}{3}\pi r^3 \left[j\omega\mu_0 \frac{r^2}{2} - \frac{1}{j\omega 3\varepsilon_0} \right], \tag{4.33}$$

where, we have used the mid-point integration rule, i.e.,

$$\langle \boldsymbol{E}^s(\boldsymbol{f}_n), \boldsymbol{f}_n \rangle = \iiint_{\mathcal{V}} \boldsymbol{E}^{\mathrm{s}}(\boldsymbol{f}_n) \cdot \boldsymbol{f}_n \, \mathrm{d}V \approx \frac{4}{3}\pi r^3 \boldsymbol{E}^{\mathrm{s}}(\boldsymbol{f}_n(\boldsymbol{r}_n)) \cdot \boldsymbol{f}_n, \tag{4.34}$$

where $\boldsymbol{r}_n$ is the centroid of the nth cube, and

$$\frac{4}{3}\pi r^3 = \iiint_{\mathcal{V}_n} \mathrm{d}V \tag{4.35}$$

is the volume of the n^{th} sphere. As long as $k_0 a \ll 1$, we can approximate Eq. (4.33) as follows:

$$\mathsf{Z}_{nn} \approx \frac{4}{3}\pi r^3 \frac{1}{j\omega(\varepsilon - \varepsilon_0)} - \frac{4}{3}\pi r^3 \left[-\frac{1}{j\omega 3\varepsilon_0} \right], \tag{4.36}$$

4.5.2 The Off-Diagonal Moment Matrix Term Z_{mn} $(m \neq n)$

The off-diagonal moment matrix entries are computed using the equivalent dipole moment approach. Using this approach, the field radiated by a basis function of uniform current is assumed to be equal to the field of an infinitesimal dipole placed at the centre of this spherical support with dipole moment $Il\hat{\boldsymbol{f}}$, where $\hat{\boldsymbol{f}} \in \{\hat{\boldsymbol{x}}, \hat{\boldsymbol{y}}, \hat{\boldsymbol{z}}\}$. The E-field of a z-oriented dipole can be easily computed using the following analytical expressions (derived in [64]).

$$E_x^{\mathrm{s}} = \frac{IlC_{mn}}{4\pi j\omega\varepsilon_0} xz e^{-jk_0|\boldsymbol{r}_{mn}|} \tag{4.37a}$$

$$E_y^{\mathrm{s}} = \frac{IlC_{mn}}{4\pi j\omega\varepsilon_0} yz e^{-jk_0|\boldsymbol{r}_{mn}|} \tag{4.37b}$$

$$E_z^{\mathrm{s}} = \frac{Il}{4\pi j\omega\varepsilon_0} \left[C_{mn} z^2 + \frac{k_0^2}{|\boldsymbol{r}_{mn}|} - \frac{jk_0}{|\boldsymbol{r}_{mn}|^2} - \frac{1}{|\boldsymbol{r}_{mn}|^3} \right] e^{-jk_0|\boldsymbol{r}_{mn}|}, \tag{4.37c}$$

where

$$C_{mn} = -\frac{k_0^2}{|\boldsymbol{r}_{mn}|^3} + \frac{3jk_0}{|\boldsymbol{r}_{mn}|^4} + \frac{3}{|\boldsymbol{r}_{mn}|^5}. \tag{4.38}$$

Substituting (4.37) in (4.29), and using that $\boldsymbol{f}_n \cdot \boldsymbol{f}_m = 0$ ($\forall\ m \neq n$), we get for a z-oriented basis function current

$$\mathsf{Z}_{mn} = -\frac{4}{3}\pi r^3 [E_x^{\mathrm{s}}\hat{\boldsymbol{x}} + E_y^{\mathrm{s}}\hat{\boldsymbol{y}} + E_z^{\mathrm{s}}\hat{\boldsymbol{z}}] \cdot \boldsymbol{f}_m. \tag{4.39}$$

Here, Z_{mn} is the electric field tested by the mth basis function which is radiated by the nth basis function current, which is assumed to be z-oriented.

The H-field of a z-oriented magnetic dipole can be easily computed using the following analytical expressions (derived using duality principle from(4.37)).

$$H_x^{\mathrm{s}} = \frac{IlC_{mn}}{4\pi j\omega\mu_0} xz e^{-jk_0|\boldsymbol{r}_{mn}|} \tag{4.40a}$$

$$H_y^{\mathrm{s}} = \frac{IlC_{mn}}{4\pi j\omega\mu_0} yz e^{-jk_0|\boldsymbol{r}_{mn}|} \tag{4.40b}$$

$$H_z^{\mathrm{s}} = \frac{Il}{4\pi j\omega\mu_0} \left[C_{mn} z^2 + \frac{k_0^2}{|\boldsymbol{r}_{mn}|} - \frac{jk_0}{|\boldsymbol{r}_{mn}|^2} - \frac{1}{|\boldsymbol{r}_{mn}|^3} \right] e^{-jk_0|\boldsymbol{r}_{mn}|}, \tag{4.40c}$$

where

$$C_{mn} = -\frac{k_0^2}{|\boldsymbol{r}_{mn}|^3} + \frac{3jk_0}{|\boldsymbol{r}_{mn}|^4} + \frac{3}{|\boldsymbol{r}_{mn}|^5}. \tag{4.41}$$

Substituting (4.40) in (4.29), and using that $\boldsymbol{f}_n \cdot \boldsymbol{f}_m = 0$ ($\forall\ m \neq n$), we get for a z-oriented basis function current

$$\mathsf{Z}_{mn} = -\frac{4}{3}\pi r^3 [H_x^{\mathrm{s}}\hat{\boldsymbol{x}} + H_y^{\mathrm{s}}\hat{\boldsymbol{y}} + H_z^{\mathrm{s}}\hat{\boldsymbol{z}}] \cdot \boldsymbol{f}_m. \tag{4.42}$$

Here, Z_{mn} is the electric field tested by the mth basis function which is radiated by the nth basis function current, which is assumed to be z-oriented.

By the same analogy, the magnetic field of a z-oriented dipole can be easily computed using the following analytical expressions.

$$H_x^{\mathrm{s}} = -\frac{Il}{4\pi} \left[\frac{1}{\boldsymbol{r}_{mn}^3} + \frac{jk_0}{\boldsymbol{r}_{mn}^2} \right] y e^{-jk_0|\boldsymbol{r}_{mn}|}, \tag{4.43a}$$

$$H_y^{\mathrm{s}} = \frac{Il}{4\pi} \left[\frac{1}{\boldsymbol{r}_{mn}^3} + \frac{jk_0}{\boldsymbol{r}_{mn}^2} \right] x e^{-jk_0|\boldsymbol{r}_{mn}|}, \tag{4.43b}$$

$$H_z^{\mathrm{s}} = 0. \tag{4.43c}$$

In the following, we will justify that we can choose for the strength of above dipole moment that $Il = \frac{4}{3}\pi r^3$. By substituting (4.14) in (4.12), we have that

$$\boldsymbol{E} = \frac{1}{j\omega\varepsilon_0}\left[\boldsymbol{\nabla}\left(\boldsymbol{\nabla}\cdot\boldsymbol{A}\right) + k_0^2\boldsymbol{A}\right]. \tag{4.44}$$

The magnetic vector potential $\boldsymbol{A}$ in (4.16) can be evaluated for $\boldsymbol{f}_n(\boldsymbol{r}') = Il\hat{\boldsymbol{z}}\delta(x')\delta(y')\delta(z')$ as

$$\begin{aligned}\boldsymbol{A} &= \iiint_V \boldsymbol{f}_n(\boldsymbol{r}')\frac{e^{-jk_0|\boldsymbol{r}-\boldsymbol{r}'|}}{4\pi|\boldsymbol{r}-\boldsymbol{r}'|}\,\mathrm{d}V' \\ &= \frac{Il}{4\pi}\hat{\boldsymbol{z}}\frac{e^{-jk_0|\boldsymbol{r}|}}{|\boldsymbol{r}|}.\end{aligned} \tag{4.45}$$

Substituting (4.45) in (4.44) gives the field of a dipole [64] which is then tested at the observation sphere to get Z_{mn}. However, instead of computing the field from a dipole, we have to evaluate the actual volumetric integral in (4.45) for the basis function $\boldsymbol{f}_n$. Assuming a sphere of z-oriented uniform current

$$\boldsymbol{f}_n(\boldsymbol{r}) = \begin{cases} \hat{\boldsymbol{z}}, & \boldsymbol{r} \in V_n \\ \boldsymbol{0}, & \boldsymbol{r} \notin V_n, \end{cases} \tag{4.46}$$

where $V_n = \frac{4}{3}\pi r^3$ represents the volume of the source sphere. Using (4.46) in (4.45), yields

$$\boldsymbol{A} = \int_{-a/2}^{a/2}\int_{-a/2}^{a/2}\int_{-a/2}^{a/2}\hat{\boldsymbol{z}}\frac{e^{-jk_0|\boldsymbol{r}-\boldsymbol{r}'|}}{4\pi|\boldsymbol{r}-\boldsymbol{r}'|}\,\mathrm{d}V'.$$

Then, using the mid-point integration rule,

$$\iiint_{\mathcal{V}_n}\boldsymbol{f}(\boldsymbol{r}')\,\mathrm{d}V' = \mathcal{V}_n\boldsymbol{f}(\boldsymbol{r}_0) = \frac{4}{3}\pi r^3\boldsymbol{f}(\boldsymbol{r}_0),$$

where $\boldsymbol{r}_0 = (\boldsymbol{0},\boldsymbol{0},\boldsymbol{0})$ is the center point of the sphere, and V_n is the sphere volume, we obtain

$$\begin{aligned}\boldsymbol{A} &= \int_{-a/2}^{a/2}\int_{-a/2}^{a/2}\int_{-a/2}^{a/2}\hat{\boldsymbol{z}}\frac{e^{-jk_0|\boldsymbol{r}-\boldsymbol{r}'|}}{4\pi|\boldsymbol{r}-\boldsymbol{r}'|}\,\mathrm{d}V' \\ &= \frac{\frac{4}{3}\pi r^3}{4\pi}\hat{\boldsymbol{z}}\frac{e^{-jk_0|\boldsymbol{r}|}}{|\boldsymbol{r}|},\end{aligned} \tag{4.47}$$

which shows that taking a dipole in (4.45) to represent the scattered field is equivalent to using a mid-point integration rule for evaluating $\boldsymbol{A}$ using the actual volumetric current distribution, provided that $Il = \frac{4}{3}\pi r^3$. Conclusively, subdividing the source cube into smaller sub-cubes each of which contains a dipole with associated dipole moment will, therefore, yield the same total radiated field as evaluating $\boldsymbol{A}$ through a composite mid-point integration rule using the actual sphere supporting a uniform current.

4.6 Summary

We discussed the theoretical formulation for the full-wave point-dipole method. The volume equivalence principle has been explained, and the electric field integral equation (EFIE) is formulated to determine the equivalent currents inside the dielectric volume. Both the point-matching and Galerkin Method were proven to yield approximately same results for the proposed scheme. The microdomain spherical basis functions have been discussed and their potential to highlight composites has been highlighted. A complete procedure to formulate the moment-matrix has been laid down, which is completely based on the closed-form expressions for both the diagonal and off-diagonal moment-matrix elements.

Chapter 5

Numerical Modelling of 2D EM Materials and Material-Design Scheme

The method to calculate the scattering by scatterer-based 3D-composites has been outlined in the previous chapter. In this chapter, we propose a 2D-material design scheme based on randomly distributed wires in a low-dielectric matrix. The design scheme is supplemented by a 2D numerical modelling method for numerically efficient calculations. A 2D Lüneburg lens for a beamforming application is designed and simulated, and the results are compared to a commercial electromagnetic software CST. In addition, a 2D Lüneburg lens is designed using lossy inclusions, which functions as an absorber in a broad frequency regime. Also, the industrial applications of the proposed broadband absorber are discussed. An imaging device Maxwell's Fisheye is designed, and its operation is highlighted by simulating it using the proposed numerical-modelling scheme.

5.1 The Numerical-Modelling Scheme in 2D

The fundamental principle in calculating the scattering by cylindrical basis is similar to that of the 3D calculations mentioned in the preceding chapter. The mathematical design, however, is distinct from that of the 3D derivations. In the following, we derive the mathematical basis for the 2D electromagnetic modelling of composites that consist of infinitely long, electrically thin, and axially symmetric dielectric or metallic rods. Suppose the cylinders are placed along the z-axis, and consider the transverse-magnetic (TM) incidence. In the TM case, the magnetic-field component is transverse to z; therefore, only E_z component exists along the z-axis. We begin the derivations by making use of the volume-equivalence principle (Eq. 4.6) as:

$$\boldsymbol{J}_{\text{eq}} = \boldsymbol{J}_{\text{prim}} + j\omega(\varepsilon - \varepsilon_0)(\boldsymbol{E}^{\text{i}} + \boldsymbol{E}^{\text{s}}). \tag{5.1}$$

The current density $\boldsymbol{J}_{\text{eq}}$ can be expanded in terms of N (total number of basis) unknowns $(\alpha_1 \dots \alpha_N)$ as:

$$\boldsymbol{J}_{\text{eq}} = \sum_{n=1}^{N} \alpha_n \boldsymbol{f}_n(\boldsymbol{\rho}), \tag{5.2}$$

$$\boldsymbol{f}_n(\boldsymbol{\rho}) = \begin{cases} \hat{\boldsymbol{z}}, & \boldsymbol{\rho} \in \mathcal{S}_n; n \in \{1, \dots, N\} \\ \boldsymbol{0}, & \boldsymbol{\rho} \notin \mathcal{S}_n, \end{cases}$$

where $\mathcal{S}_n$ denotes the cross-sectional area of the cylinder n, $\boldsymbol{f}_n$ denotes the nth basis functions, and α_n is the corresponding nth expansion coefficient. The symbol $\boldsymbol{\rho}$ denotes the radial vector in polar coordinates. Substituting Eq. (5.2) in (5.1), we get:

$$\begin{aligned} \boldsymbol{J}_{\text{eq}} &= \sum_{n=1}^{N} \alpha_n \boldsymbol{f}_n(\boldsymbol{\rho}) \\ &= j\omega(\varepsilon - \varepsilon_0) \left[\boldsymbol{E}^{\text{i}}(\boldsymbol{\rho}) + \boldsymbol{E}^{\text{s}} \left(\sum_{n=1}^{N} \alpha_n \boldsymbol{f}_n(\boldsymbol{\rho}) \right) \right] \\ &= j\omega(\varepsilon - \varepsilon_0) \left[\boldsymbol{E}^{\text{i}}(\boldsymbol{\rho}) + \sum_{n=1}^{N} \alpha_n \boldsymbol{E}^{\text{s}}(\boldsymbol{f}_n(\boldsymbol{\rho})) \right]. \end{aligned} \tag{5.3}$$

The next step is to test Eq. (5.3) at N points to get N equations with N unknowns, which we can then solve for the m^{th} test point ($m = 1, 2, \ldots, N$). In general, one can test the above equation over a small region, i.e., in a weak form using the symmetric product, which is defined as

$$\langle \boldsymbol{a}, \boldsymbol{b} \rangle = \iint\limits_{S_\text{a} \bigcap S_\text{b}} \boldsymbol{a} \cdot \boldsymbol{b} \, \mathrm{d}S, \tag{5.4}$$

where S_a and S_b are the supports of the basis and test or weight functions a and b, respectively. Our choice of test functions is the same as that of basis functions (i.e., pulse-shaped), and the testing scheme is called Galerkin's method. After application of the testing scheme, we get:

$$\sum_{n=1}^{N} \alpha_n \left\langle \boldsymbol{f}_n(\boldsymbol{\rho}), \boldsymbol{w}_m(\boldsymbol{\rho}) \right\rangle = j\omega(\varepsilon - \varepsilon_0) \left[\left\langle \boldsymbol{E}^\text{i}(\boldsymbol{f}_n(\boldsymbol{\rho})), \boldsymbol{w}_m(\boldsymbol{\rho}) \right\rangle + \sum_{n=1}^{N} \alpha_n \left\langle \boldsymbol{E}^\text{s}(\boldsymbol{f}_n(\boldsymbol{\rho})), \boldsymbol{w}_m(\boldsymbol{\rho}) \right\rangle \right], \tag{5.5}$$

where the total field is the sum of the incident and scattered fields, and the scattered field can be expressed in terms of a vector potential ($\boldsymbol{A}$) as:

$$\boldsymbol{E}^\text{s} = -j\omega \boldsymbol{A}. \tag{5.6}$$

Because the cylinders are infinitely long, the gradient of scalar potential ($\boldsymbol{\nabla}\phi$) vanishes for a normally incident transverse magnetic (TM) wave. On the contrary, the scalar potential term is inevitable for the normally incident transverse-electric (TE) illumination or in the case of cylinders' length comparable to that of the radius of the cylinders. For the TM wave excitation, the 2D vector potential can be calculated by the use of Ampere's law and can be given as (in terms of inhomogeneous vector potential):

$$A_\text{z} = \frac{\mu_0}{4j} \iint\limits_{\mathcal{S}} J_\text{eq}(\rho) H_0^{(2)}(k_0 \rho) \, \mathrm{d}S, \tag{5.7}$$

where $\rho = |\boldsymbol{\rho}|$, k_0 denotes the free-space wavenumber, and μ_0 denotes the free-space permeability. The symbol $H_i^{(2)}$ denotes the Hankel function of second kind and order i. In physical terms, it represents an outgoing wave. From Eqs. 5.6 and 5.7, the field scattered by an infinitely long cylinder, which has an electrically small radius, can be given as:

$$E_{\mathrm{z}}^{\mathrm{s}} = \frac{-j\omega\mu_0}{4j} \iint\limits_{\mathcal{S}} J_{\mathrm{eq}}(\rho) H_0^{(2)}(k_0\rho)\,\mathrm{d}S. \tag{5.8}$$

The above integral involves a singularity at the origin of the cylinder, which needs to be extracted analytically. For a uniform equivalent current density (i.e., $J_{\mathrm{eq}}(\rho)$ =Constant for $\rho < a$), the above integral has been analytically evaluated to give the following closed-form expression [73, 74]:

$$E_{\mathrm{z}}^{\mathrm{s}} = \alpha \begin{cases} -\frac{\eta\pi a}{2} J_0(k_0\rho) H_1^{(2)}(k_0 a) + \frac{j\eta}{k_0}, & \rho < 0 \\ -\frac{\eta\pi a}{2} J_1(k_0 a) H_0^{(2)}(k_0\rho), & \rho > 0 \end{cases} \tag{5.9}$$

where a denotes the radius of the cylinder and $J_0(k_0\rho)$ denotes the cylindrical Bessel-function of the first-kind and zeroth-order. In physical terms, it represents a standing wave. The incident field can thus be written in terms of the total and scattered fields and testing the basis (when $m = n$) from Eq. 5.5 as follows:

$$\begin{aligned} \left\langle \boldsymbol{E}^{\mathrm{i}}(\boldsymbol{f}_n(\boldsymbol{\rho})), \boldsymbol{w}_n(\boldsymbol{\rho}) \right\rangle &= \frac{\alpha_n}{j\omega\varepsilon_0(\varepsilon_{\mathrm{r}} - 1)} + \alpha_n \left(\frac{\eta\pi a_n}{2} J_0(k_0\rho_{nn}) H_1^{(2)}(k_0 a_n) - \frac{j\eta}{k_0} \right), \\ &= \alpha_n \left(\frac{\eta}{jk_0(\varepsilon_{\mathrm{r}} - 1)} + \frac{\eta\pi a_n}{2} J_0(k_0\rho_{nn}) H_1^{(2)}(k_0 a_n) - \frac{j\eta}{k_0} \right), \\ &= \alpha_n \left(\frac{\eta\varepsilon_{\mathrm{r}}}{jk_0(\varepsilon_{\mathrm{r}} - 1)} + \frac{\eta\pi a_n}{2} H_1^{(2)}(k_0 a_n) \right), \end{aligned} \tag{5.10a}$$

where n is the source cylinder index, while m is the observation cylinder index. Because the cylinders are electrically thin, the field is uniform inside a particular cylinder. This results in Galerkin method being equal to the point-matching method and, hence, we ignore the area term in the above equation. Similarly, the field scattered by the cylinder m outside its domain (when $m \neq n$) can be expressed as:

$$\left\langle \boldsymbol{E}^{\mathrm{i}}(\boldsymbol{f}_n(\boldsymbol{\rho})), \boldsymbol{w}_m(\boldsymbol{\rho}) \right\rangle = \alpha_n \left(\frac{\eta\pi a_n}{2} J_1(k_0 a_n) H_0^{(2)}(k_0\rho_{mn}) \right), \tag{5.11}$$

where ρ_{mn} denotes the vector length from the centre of the cylinder m to that of n. It would be pertinent to mention that Eqs. 5.10 and 5.11 have been normalised by the area of the test cylinder. Equations 5.10 and 5.11 can be arranged in a matrix form as follows:

$$\begin{bmatrix} \mathsf{Z}_{11} & \cdots & \mathsf{Z}_{1N} \\ \vdots & \ddots & \vdots \\ \mathsf{Z}_{N1} & \cdots & \mathsf{Z}_{NN} \end{bmatrix} \begin{bmatrix} \alpha_1 \\ \vdots \\ \alpha_N \end{bmatrix} = \begin{bmatrix} \mathsf{E}_1^{\mathrm{i}} \\ \vdots \\ \mathsf{E}_N^{\mathrm{i}} \end{bmatrix}, \tag{5.12}$$

where $\mathsf{E}_n^{\mathrm{i}}$ denotes the incident electric field in the centre of the cylinder n, and Z_{mn} denotes the coupling between the source cylinder n and the observation cylinder m.

$$\mathsf{Z}_{mn} = \begin{cases} -\frac{j\eta\varepsilon_{\mathrm{r}}}{k_0(\varepsilon_{\mathrm{r}}-1)} + \frac{\eta\pi a_n}{2} H_1^2(k_0 a_n), & m = n \\ \frac{\eta\pi a_n}{2} J_1(k_0 a_n) H_0^2(k_0 \rho_{mn}). & m \neq n \end{cases}$$

Once the unknown coefficients $(\alpha_1, \ldots \alpha_n)$ are known, the scattered field inside and outside the cylindrical regions can be calculated from Eq. 5.9.

5.2 Effective Medium Approximation

The Clausius-Mossotti and Maxwell-Garnett expressions (explained in the previous chapters) allow to homogenise composites based on the spherical inclusions. In this section, we derive a generalised expression for calculating the effective permittivity of composites that are composed of any shape of inclusions. Let us consider a stand-alone scatterer and set the primary current density equal to zero as (from Eq. 5.1):

$$\boldsymbol{J}_{\mathrm{eq}} = j\omega(\varepsilon - \varepsilon_0)(\boldsymbol{E}^{\mathrm{i}} + \boldsymbol{E}^{\mathrm{s}}). \tag{5.13}$$

By rearranging the above equation, we get the following expression for the homogenised permittivity:

$$\varepsilon_{\mathrm{eff}} = \frac{\boldsymbol{J}_{\mathrm{eq}}}{j\omega\varepsilon_0(\boldsymbol{E}^{\mathrm{i}} - \boldsymbol{E}^{\mathrm{dep}})} + 1. \tag{5.14}$$

In the above equation, $\boldsymbol{E}^{\text{dep}}$ represents the difference between the incident and total fields ($\boldsymbol{E}^{\text{i}} - \boldsymbol{E}^{\text{tot}}$) inside the inclusion scatterer. We substitute the equivalent relationship between the equivalent current and the polarisation density ($\boldsymbol{J}_{\text{eq}} = j\omega\boldsymbol{P}$) in Eq. 5.14 and simplify the resultant expression as follows:

$$\begin{aligned}\varepsilon_{\text{eff}} &= \frac{j\omega\boldsymbol{P}}{j\omega\varepsilon_0(\boldsymbol{E}^{\text{i}} - \boldsymbol{E}^{\text{dep}})} + 1, \\ &= \frac{\boldsymbol{P}}{\varepsilon_0(\boldsymbol{E}^{\text{i}} - \boldsymbol{E}^{\text{dep}})} + 1. \end{aligned} \tag{5.15}$$

Due to the fact that we consider all the vector quantities in one Cartesian direction (in this case along z-axis), we can safely omit the vector symbol and proceed with the scalar quantities in the rest of the derivations as follows:

$$\varepsilon_{\text{eff}} = \frac{\frac{P}{\varepsilon_0 E^{\text{i}}}}{1 - \frac{\varepsilon_0 E^{\text{dep}}}{P}\frac{P}{\varepsilon_0 E^{\text{i}}}} + 1, \tag{5.16a}$$

$$= \frac{\frac{P}{\varepsilon_0 E^{\text{i}}}}{1 - L\frac{P}{\varepsilon_0 E^{\text{i}}}} + 1, \tag{5.16b}$$

$$= \frac{\frac{n\alpha^{\text{p}} E^{\text{i}}}{\varepsilon_0 E^{\text{i}}}}{1 - L\frac{n\alpha^{\text{p}} E^{\text{i}}}{\varepsilon_0 E^{\text{i}}}} + 1, \tag{5.16c}$$

$$= \frac{\frac{n\alpha^{\text{p}}}{\varepsilon_0}}{1 - L\frac{n\alpha^{\text{p}}}{\varepsilon_0}} + 1, \tag{5.16d}$$

$$= \frac{f\alpha_{\text{n}}^{\text{p}}}{1 - fL\alpha_{\text{n}}^{\text{p}}} + 1. \tag{5.16e}$$

In the above equations, the superscript p is introduced to distinguish between the polarisability and the unknown coefficient, and $L = \frac{\varepsilon_0 E^{\text{dep}}}{P}$ is the depolarisation factor, where $P = (\varepsilon - \varepsilon_0)\boldsymbol{E}^{\text{tot}}$. The dipole moment can be given as $p = \alpha E$, and the dipole moment per unit volume $P = n\alpha E$ is the polarisation density, where n represents the number of scatterers per unit volume. The polarisability has been normalised with the free-space permittivity and the volume of the inclusion ($\mathcal{V}_{\text{i}}$) as $\alpha_{\text{n}}^{\text{p}} = \alpha^{\text{p}}/\varepsilon_0\mathcal{V}_{\text{i}}$. The volume fraction is $f = n\mathcal{V}_{\text{i}}$.

In the following, we derive Clausius-Mossotti and Maxwell-Garnett expressions for spherical inclusions based on Eq. 5.16. Also, we derive the effective permittivity expressions for cylindrical inclusions.

Spherical Inclusions

From the foregoing discussion, a generalised expression for the effective permittivity of composites of one type of inclusions is as follows:

$$\varepsilon_{\text{eff}} = \frac{f\alpha_{\text{n}}^{\text{p}}(\omega)}{1 - f\alpha_{\text{n}}^{\text{p}}(\omega)L} + 1. \tag{5.17}$$

For a sphere, the normalised static polarisability can be given as (see Eq. 6.8)

$$\alpha_{\text{n}}^{\text{p}} = 3\left(\frac{\varepsilon_{\text{r}} - 1}{\varepsilon_{\text{r}} + 2}\right). \tag{5.18}$$

The depolarisation factor L can be calculated as

$$\begin{aligned} L &= \frac{\varepsilon_0}{P}\left[1 - \frac{3}{2 + \varepsilon_{\text{r}}}\right], \\ &= \frac{\varepsilon_0}{\varepsilon_0(\varepsilon_{\text{r}} - 1)E^{\text{tot}}}\left[1 - \frac{3}{2 + \varepsilon_{\text{r}}}\right], \\ &= \frac{1}{3}. \end{aligned} \tag{5.19}$$

In the above equation $E^{\text{tot}} = 3/(\varepsilon_{\text{r}} + 2)$ is the total field inside the sphere [75]. By substituting the polarisability and depolarisation expressions for a sphere in Eq. 5.17, we get

$$\begin{aligned} \varepsilon_{\text{eff}} &= 1 + \frac{3f(\varepsilon_{\text{r}} - 1)}{(\varepsilon_{\text{r}} + 2)\left[1 - f\frac{(\varepsilon_{\text{r}} - 1)}{(\varepsilon_{\text{r}} + 2)}\right]}, \\ &= \frac{2f(\varepsilon_{\text{r}} - 1) + (\varepsilon_{\text{r}} + 2)}{(\varepsilon_{\text{r}} + 2) - f(\varepsilon_{\text{r}} - 1)}. \end{aligned} \tag{5.20}$$

The above expression is known as Maxwell-Garnett formula. In derivations of Eqs. 5.20 and 5.16, a standalone cubic unit-cell was assumed bearing a spherical inclusion in its centre. The result, therefore, dispels a common misconception that the CM or MG cater for the coupling among the scatterers in a composite. So, based on this discussion, the CM or MG is supposed to yield accurate results in the electrostatics limit and the periodic arrangement of inclusions but the relatively less accurate result for a random arrangement of scatterers.

Cylindrical Inclusion

We consider infinitely large cylinders for the derivation of the effective permittivity response. For the TM case, the polarizability of a stand-alone cylinder of infinite length can be derived based on the calculations in Section 4.1.

The unknown parameter α can be calculated from Eq. 5.10 as follows:

$$\begin{aligned}\alpha &= \frac{E^{\mathrm{i}}}{\left(\frac{\eta\varepsilon_{\mathrm{r}}}{jk_0(\varepsilon_{\mathrm{r}}-1)} + \frac{\eta\pi a}{2} J_0(k_0\rho)H_1^{(2)}(k_0 a)\right)},\\ &= \frac{E^{\mathrm{i}}}{\frac{\eta}{jk_0}\left(\frac{1}{\varepsilon_{\mathrm{r}}-1}\right)},\\ &= j\omega\varepsilon_0(\varepsilon_{\mathrm{r}}-1). \end{aligned} \tag{5.21}$$

From the above equation, the normalised polarisability is $\alpha_{\mathrm{n}}^{\mathrm{p}} = \varepsilon_{\mathrm{r}} - 1$. By multiplying the calculated parameter α with the field scattered by a cylindrical object, we can calculate the field scattered by the object as follows:

$$\begin{aligned} E^{\mathrm{s}} &= \alpha\left[\frac{\eta\varepsilon_{\mathrm{r}}}{jk_0(\varepsilon_{\mathrm{r}}-1)} + \frac{\eta\pi a}{2} J_0(k_0\rho)H_1^{(2)}(k_0 a)\right],\\ &= j\omega\varepsilon_0(\varepsilon_{\mathrm{r}}-1)\left[\frac{\eta\varepsilon_{\mathrm{r}}}{jk_0(\varepsilon_{\mathrm{r}}-1)} + \frac{\eta\pi a}{2} J_0(k_0\rho)H_1^{(2)}(k_0 a)\right],\\ &= 0. \end{aligned} \tag{5.22}$$

The above result could also be derived by using the electromagnetic boundary conditions as the tangential component is continuous along the boundary of the cylinders. This results the incident field equal to the total field inside the cylinder.

Since the internal and incident fields are equal, the depolarization factor is zero. By substituting the depolarization factor and the normalised polarizability of infinitely long cylinders in Eq. 5.16, we get the effective permittivity as:

$$\varepsilon_{\mathrm{eff}} = f\varepsilon_{\mathrm{p}} - f + 1, \tag{5.23}$$

where ε_{p} denotes the permittivity of an inclusion cylinder. The above expression is consistent with that available in the literature [76] for a composite medium composed of infinitely large cylinders in the free space. In 2D-homogenisation, the symbol f

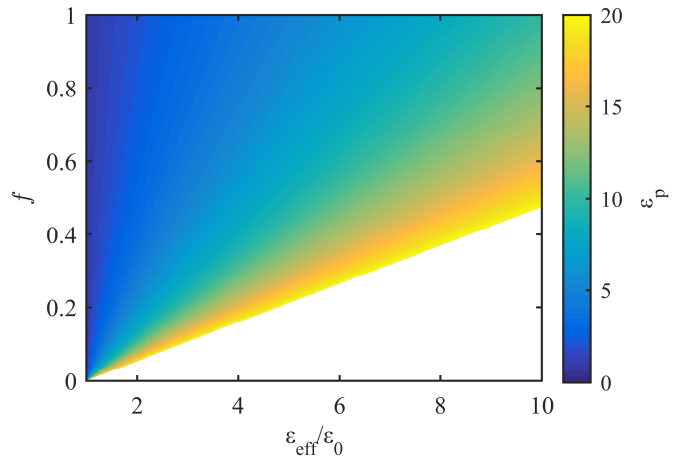

Figure 5.1: Selection rules for the effective permittivity modelling of a 2D material. A desired value of the effective permittivity can be achieved by using lossless dielectric wires in a host medium. Free-space is considered as the host.

represents the surface fraction instead of the volume fraction. The selection of the inclusion-cylinder permittivity and the corresponding surface fraction are not unique to achieve a specific effective permittivity value of the homogenised medium. This selection rule has been demonstrated in Fig. 5.1 based on Eq. 5.23.

5.3 2D Lüneburg Lens Design and Validation

We considered a 2D Lüneburg lens of radius equal to 3λ, and discretised it into 8 layers. The permittivity of each layer was calculated as per Lüneburg lens permittivity profile, which is expressed as:

$$\varepsilon_{\mathrm{l}} = 2 - \left(\frac{r}{R}\right)^2, \tag{5.24}$$

where r denotes the radial variation from the center(high permittivity) till the edge(ambient permittivity) and R denotes the lens radius. Each discrete layer was then engineered using infinitely long dielectric cylinders of radius $\lambda/60$, whose location was calculated according to a normal distribution. Equation 5.25 was employed to calculate the volume fraction of cylinders-to-host in a given layer. Discretization details will be discussed in Section 7.2 of Chapter 7 The lens design has been validated in comparison with the discrete but homogeneous dielectric-layers' design in CST. The simulation results using the proposed 2D-modelling method and that of CST have been juxtaposed in Fig. 5.2. The results are in good agreement with each other. The volume fraction can be designed from Eq. 5.23 as follows:

$$f = \frac{\varepsilon_{\text{eff}} - 1}{\varepsilon_{\text{p}} - 1}, \tag{5.25}$$

where ε_{p} denotes the permittivity of inclusion cylinder particle.

5.4 Absorber Design using Lüneburg Lens

An electromagnetic absorber suppresses the transmission and reflection of electromagnetic waves incident on it. Metamaterial and non-resonant design schemes are usually used for absorber designs. Metamaterial designs are usually efficient though narrowband, while non-resonant designs are usually broadband. We opt to design absorbers by using non-resonant wire medium for a broadband operation. Non-resonant absorbers are usually based either on microwave principles using metallic and dielectric elements or on the designs that utilise the potential of modern-material-manufacturing schemes. A recent absorber design using the advanced materials has been proposed in [77], where the size of the absorber is about a thousand times smaller than the operating wavelength, and the design renders a broadband device operation.

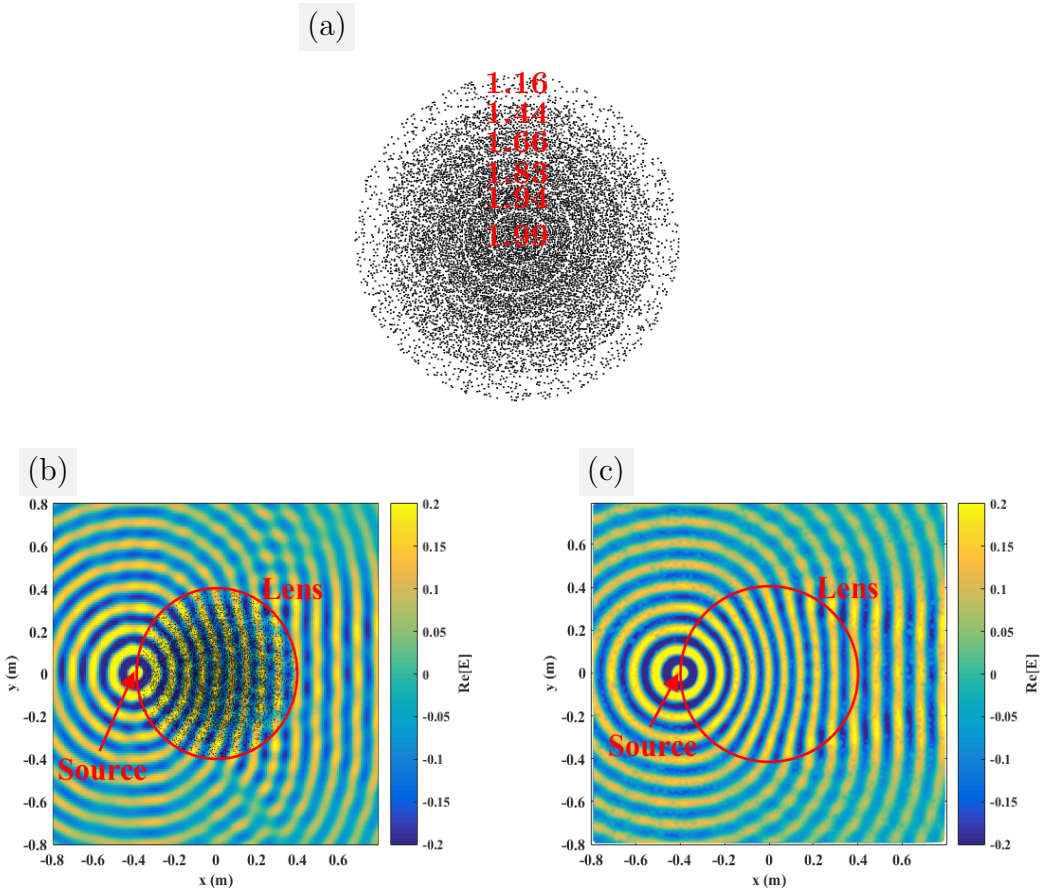

Figure 5.2: A 2D Lüneburg lens validation. The relative permittivity of the wires is 4, and the loss tangent is 0. The radius of the inclusion cylinders is $\lambda/60$ and that of the lens is 4λ. The simulation frequency is 3GHz. (a) The EM scattering from a metasurface composed of spherical meta-atoms (b) The 2D Lüneburg lens simulated electric field using MEDM (c) The 2D Lüneburg lens simulated electric field (normalised) using CST by representing each discretised layer as having uniform permittivity.

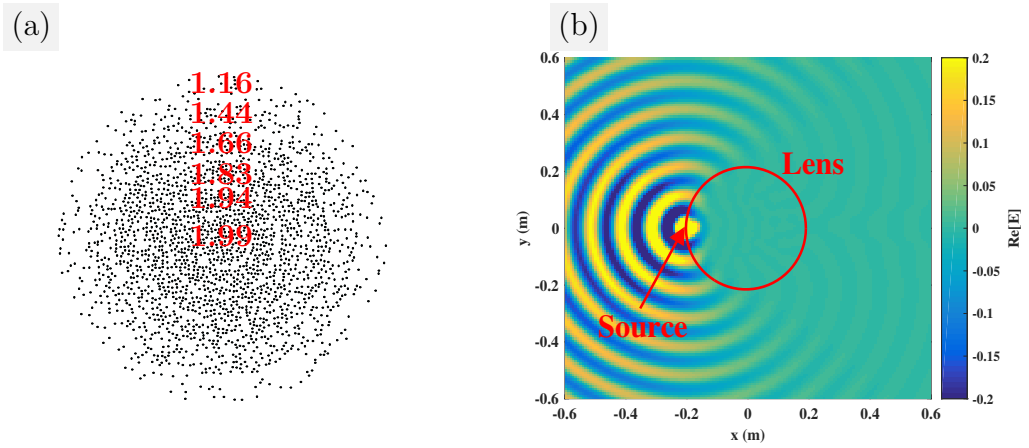

Figure 5.3: A microwave absorber design using a random arrangement of the wire medium. The relative permittivity of the wires is 4, and the loss tangent is 5. The simulation frequency is 3GHz. The radius of the inclusion cylinders is $\lambda/60$ and that of the lens is 2λ. (a) The geometry of the 2D Lüneburg lens. The cylinders are located based on normal distribution (b) Field values of the polarisation component (i.e., z-component).

Electromagnetic compatibility (EMC) is a necessary compliance requirement imposed by the Federal Communications Commission (FCC) and the relevant authorities in the non-US regions around the globe. Ever since the introduction of Moore's law, the speculated industrial trend in miniaturising a transistor with time and, as a consequence, scaling down the circuit size, has been consistent with the trends in the decades following the prediction [78]. Modern electronic devices operate at relatively higher frequencies and higher data rates, which worsens electromagnetic interference (EMI). The EMI in printed circuit boards (PCBs) predicates mainly on the electronic vias that are used to route the signal from one layer to another. High-speed routeing results in more EMI, particularly in multi-layered PCBs.

Fig. 5.3a depicts a planar top view of a random arrangement of infinitely long cylinders. We propose to use the Lüneburg lens to mitigate the effect of the EMI. The desired material functionality can be achieved by designing the Lüneburg lenses to perform like an absorber, which can be accomplished by using lossy inclusions in a free-space background medium. The discretised lens can be designed using the

lower Wiener bound, which is given in Eq. 6.1.

The stitching of the periphery of a PCB to mitigate the fringe fields off the PCB edges has been proposed in the past [79], but the drawbacks of the stitching scheme include the reflection off the PCB periphery, which changes the input impedance of the routeing vias in the circuit. However, Lüneburg-lens-based cylinders can be used for stitching the periphery for the absorption of the field incident on it. Besides, a woodpile array of Lüneburg-lens-based cylinders would result in complete absorption of the perpendicular incident waves independent of the polarisation of the incident wave.

5.5 Maxwell's Fisheye Lens

Maxwell's Fisheye lens is an imaging device that reproduces an image of the source, placed at one of its surface points, at the opposite point at the surface that is placed at a distance of diameter from the source point. The permittivity profile of the Fisheye lens is given as:

$$\varepsilon = \left(\frac{1}{1 + \left(\frac{r}{R}\right)^2} \right)^2 , \tag{5.26}$$

where R denotes the radius of the lens while r is a radial parameter from 0 to R. In Fig. 5.4, we show a discretised version of the Fisheye lens and its function as an imaging device.

The proposed 2D scheme based on the infinite lenth cylinders can be put into practice by using two parallel metallic plates that are separated by an electrically small distance, and the metallic or dielectric wires of electrically small thickness are present in between the planes in a direction perpendicular to the plates [80].

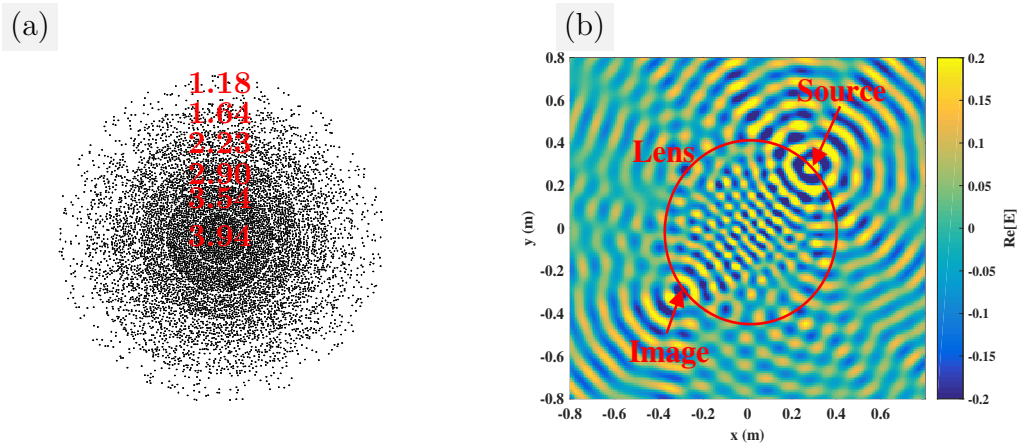

Figure 5.4: A 2D version of Maxwell's Fisheye lens using a random arrangement of the wire medium, where the wires were located according to a normal distribution. The relative permittivity of the wires is 8, and the loss tangent is 0. The simulation frequency is 3GHz. The radius of the inclusion cylinders is $\lambda/60$ and that of the lens is 4λ. (a) The geometry of the 2D Maxwell's Fisheye lens. The cylinders are located based on normal distribution (b) Field values of the polarisation component (i.e., z-component).

5.6 Summary

The scatter-based modelling scheme for cubic scatterers has been proposed in the preceding chapter. In this chapter, we proposed a 2D material modelling scheme based on infinitely large cylinders as a basis. In practical terms, the scheme is useful to simulate applications where two parallel metallic plates are separated by an electrically small distance, and the metallic or dielectric wires of electrically small thickness are present in between the planes in a direction perpendicular to the plates. Consistent with the 3D-modelling scheme, the self-term in the moment matrix was calculated analytically, and the cross-coupling terms were calculated by testing the field scattered by a standalone cylinder in the centres of the rest of the cylinders. All cross-coupling terms were calculated by following the same procedure. The Clausius-Mosotti formula was derived in Chapter 2 using the traditional approach that exists in the literature. However, in this chapter, we derived a generalised closed-form

expression from Maxwell's equations for calculating the effective permittivity in terms of the polarizability of the inclusions. The expression boils down to the Maxwell-Garnett formula for 3D-composites, and the lower Wiener bound for 2D-composites.

Several applications of design scheme have been proposed: A Lüneburg lens has been devised in both 2D and 3D using composite material design scheme. The lens has been simulated based on the scatterer-based composites by the proposed 2D modelling method proposed in this chapter, and the results were found in perfect agreement to that of discrete dielectric layers in CST.

Chapter 6

Effective Medium Modelling Using Full-Wave Point-Dipole Method

In this chapter, a homogenization scheme for periodic and random materials is proposed. The proposed scheme is demonstrated (and validated) to extract the effective properties of gradient composites. Materials with the desired EM properties are suggested to design by tweaking the geometric parameters and properties of the participating materials. Towards this end, material parameters such as lattice constant, scatterer size and permittivity are varied in periodic materials, and the volume fraction and scatterer properties are varied in random materials; and the trends in the effective properties are analysed.

6.1 Homogenization

Recent advances in electromagnetic applications requiring non-natural material properties, such as transformation optics [10] and field transformation [81], have accentuated the importance of material design. Luneberg lens and its variant

Maxwell's fish-eye lens, for example, require continuously varying material properties; namely, their refractive index varies smoothly along the radial direction from high (in the centre) to low (at the edge). One possible practical realisation of Maxwell's fisheye at THz is the use of metamaterials, that is, using metallic elements that mimic the required dielectric properties by varying the impedance of two parallel metallic plates. A rather straightforward avenue to vary the impedance of a parallel plate is to radially vary the separation between the plates [82, 83]. The main disadvantage of using metallic components to design the effective properties is the material loss in the conducting elements. Alternatively, a material with the desired electromagnetic properties can be designed, in principle, by varying the volume fraction of the inclusion-to-host materials, or by altering their dielectric contrast [84]. The effective permittivity of the resultant material remains in between the minimum and maximum values of the inclusion and host materials depending on the following bounds:

$$\varepsilon_{\max} = \sum_{i=1}^{n} v_i \varepsilon_i, \tag{6.1a}$$

$$\varepsilon_{\min} = \frac{\sum_{i=1}^{n} \varepsilon_i}{\sum_{i=1}^{n} v_i \left(\prod_{\substack{j=1 \\ j \neq i}}^{n} \varepsilon_j \right)} \tag{6.1b}$$

where $v_1 \ldots v_{n-1}$ are the volume fractions (inclusions to total volume of the composite) of $\varepsilon_1 \ldots \varepsilon_{n-1}$, respectively; and $v_n = v_{\text{total}} - (v_1 + \ldots + v_{n-1})$ is the volume fraction of the host with permittivity ε_n. It is worth mentioning that these bounds have limited validity, i.e., in the quasi-static regime only. In this context, only two off-the-shelf materials can be utilised to span a range of dielectric or magnetic properties. In greater generality, the inclusion and host materials can be considered as two primary building blocks, called metamaterial bits, and a spatial arrangement of these bits dubbed a metamaterial byte results in homogenised properties that can be judiciously manipulated to any permittivity value in between the Wiener

bounds [85]. The design procedure, however, requires improved material modelling schemes that can be efficiently used for material homogenization. The current homogenization schemes have their pros and cons; predominately, the homogenization schemes are formulated based on analytic treatments for given arrangement of circumstances only. For instance, an infinitely large periodic structure can be homogenised, below the diffraction limit, by using the powerful tools of Bloch analysis originally developed in solid state physics. Though this procedure provides the accurate and numerically efficient solution to infinite many elementary particles in a crystal, it deviates from accurate results in the case of finite size arrays, which is a typical scenario in solving mesoscale electromagnetic problems. Besides, mutual coupling in periodic boundary conditions can only be approximated, for an exact model would require computing the mutual interaction between the scatterers as well. Here, we introduce a point-dipole-based model, presented in Chapter 3, for the homogenization of the periodic or aperiodic composites. In its formulation, the volumetric polarisation currents inside the dielectric body are replaced by equivalent dipole moments whose weights are determined by enforcing a consistency condition for the electric fields inside the dielectric body. As a result, the method does not suffer from the singularities encountered in the conventional method of moment formulations that are based on Green's function approaches [86], where a superposition is made of the fields generated by infinitely small concentrated current sources.

6.2 Brief Description of Classic Homogenization Techniques

We briefly review other classical techniques that we will use for comparison with the proposed scheme in the results section. One widely known permittivity extraction technique is Nicolson-Ross-Weir (NRW), which involves the calculation of the

scattering parameters from the test sample; except for a few analytical solutions of well-defined shapes for the reflection and transmission coefficients, the extraction is usually performed using numerical calculations. Effective parameters are then calculated using the closed-form expressions given in Chapter 3. However, the extraction of the effective parameters when the sample thickness is close to the wavelength (resulting in Bragg resonances) has been a matter of concern while using the NRW technique. We use a commercial software (CST) which uses an improved homogenization model based on the reflection and transmission coefficients [88] and performs accurately even close the Bragg resonances. The two scale convergence homogenization (TSCH) technique (discussed at length in [89]) is based on the numerical resolution of an annex static problem to compute the effective permittivity of a periodic medium with arbitrary shaped inclusions.

6.3 Proposed Homogenization Scheme

Most of the classical homogenization techniques have one commonality, that is, the effective parameters they extract are based on an infinitely large arrangement of periodic scatterers, where we either ignore or calculate the approximate interaction field between the scatterers. Practical problems, however, mostly involve finite size geometries. We propose to solve finite size array of custom-arranged scatterers by replacing each inclusion scatterer in the composite by its equivalent dipole moment for the scattered field representation outside the scatterer, and perform analytical treatment of the field scattered inside the unit-cell. Unlike conventional surface-based discretization using the RWG (Rao-Wilton-Glisson) basis in full-wave electromagnetic models, the proposed method considers each scatterer as a basis. The mutual interaction between the scatterers and the self-impedance can thus be calculated analytically. The numerical computation involved is minor, that is, inversion

of the coupling matrix. Once the scattered field is known, the effective parameter extraction involves the homogenization of the field in the considered unit-cell and homogenization of the equivalent current in the test scatterer. By the application of the field consistency condition, we have

$$\boldsymbol{J}_{\mathrm{eq}}(\boldsymbol{r}) = i\omega(\varepsilon - \varepsilon_0)\boldsymbol{E}_{\mathrm{loc}}, \text{ for } \boldsymbol{r} \in \mathcal{V}_{\mathrm{b}} \tag{6.2}$$

where $\mathcal{V}_{\mathrm{b}}$ is the volume of the test scatterer. Field-consistency condition lets us calculate the effective values of the permittivity of the material.

$$(\varepsilon_{\mathrm{eff}})_{\mathrm{Pol}} = \frac{(J_{\mathrm{eq}})^{\mathrm{Basis}}_{\mathrm{Pol}}}{j\omega\varepsilon_0 E^{\mathrm{cell}}_{\mathrm{Pol}}} + 1, \tag{6.3}$$

where $\mathrm{Pol} \in \{x, y, z\}$ is the polarisation, and the average local field is calculated in a cubic unit cell of edge-length which is equal to the period, P, of the lattice. For a centrosymmetric scatterer placed at the origin of the rectangular coordinate system, we can calculate the total field in the cell as

$$E^{\mathrm{cell}}_x = \int_{-P/2}^{P/2}\int_{-P/2}^{P/2}\int_{-P/2}^{P/2} \hat{\boldsymbol{x}} \cdot \boldsymbol{E}(\boldsymbol{r}) dxdydz, \tag{6.4a}$$

$$E^{\mathrm{cell}}_y = \int_{-P/2}^{P/2}\int_{-P/2}^{P/2}\int_{-P/2}^{P/2} \hat{\boldsymbol{y}} \cdot \boldsymbol{E}(\boldsymbol{r}) dxdydz, \tag{6.4b}$$

$$E^{\mathrm{cell}}_z = \int_{-P/2}^{P/2}\int_{-P/2}^{P/2}\int_{-P/2}^{P/2} \hat{\boldsymbol{z}} \cdot \boldsymbol{E}(\boldsymbol{r}) dxdydz. \tag{6.4c}$$

The cell-field includes in part the Rayleigh scattering field, and in part the dipole radiation field. The optimal calculations for finite size geometries thus require the full-wave modelling treatment. The equivalent current in the definition of Eq. 6.3 also includes the mutual interactions among the particles. By definition, this field is constant inside the test scatterer and zero elsewhere, which allows us to integrate the equivalent current inside a basis of radius r only.

$$(J_{\mathrm{eq}})^{\mathrm{Basis}}_x = \frac{4}{3}\pi r^3 \hat{\boldsymbol{x}} \cdot \boldsymbol{J}_{\mathrm{eq}}, \tag{6.5a}$$

$$(J_{\mathrm{eq}})^{\mathrm{Basis}}_y = \frac{4}{3}\pi r^3 \hat{\boldsymbol{y}} \cdot \boldsymbol{J}_{\mathrm{eq}}, \tag{6.5b}$$

$$(J_{\mathrm{eq}})^{\mathrm{Basis}}_z = \frac{4}{3}\pi r^3 \hat{\boldsymbol{z}} \cdot \boldsymbol{J}_{\mathrm{eq}}. \tag{6.5c}$$

Notice that the symbols E_x^{cell} and $(J_{\text{eq}})_x^{\text{Basis}}$ represent the field and current in a unit-cell volume, that is, in the units of volts·meter^2 and amperes·meter, respectively. Analytical considerations of the proposed homogenization procedure (i.e., Equation 6.3) reveal that the averaging implicitly caters for the phase of the scattered field as well as equivalent current; in consequence, while the proposed method inherently sidesteps the low frequency breakdown problem, it also allows the calculation of the effective permittivity at considerable high frequencies.

The effective permeability of the composite can be calculated by duality, but the proposed scheme need to be effectively adapted to cater for the electric and magnetic dipole coupling to include both the electric and magnetic dipole moments simultaneously. Moreover, the dynamic expressions for the self-term and the dipole scattered fields can efficiently calculate the dipole moments (DMs) of both the dielectric and metallic scatterers. We vindicate this assertion by calculating the dipole moments (using the proposed modelling scheme) for a standalone dielectric- and metallic-scatterer; the results are as follows:

$$DM\,|_{\text{dielectric}} = i\omega 3\varepsilon_0 E_0 \mathcal{V}_0 \frac{\varepsilon_{\text{r}} - 1}{\varepsilon_{\text{r}} + 2}, \tag{6.6a}$$

$$DM\,|_{\text{metallic}} = i\omega 3\varepsilon_0 E_0 \mathcal{V}_0. \tag{6.6b}$$

In the above equations, $\mathcal{V}_0$ is the volume of the scatterer, and E_0 represents the amplitude of the incident field. The calculated values are consistent with those provided in the Eqs. 6.110 and 6.115 of the reference [90]; note that the Eq. 6.6b was evaluated by the application of high-conductivity limit.

6.4 Results

We considered a d-periodic arrangement of spherical scatterers in three-dimensional free space (relative permittivity = 1) with the aim to establish the relation or identify

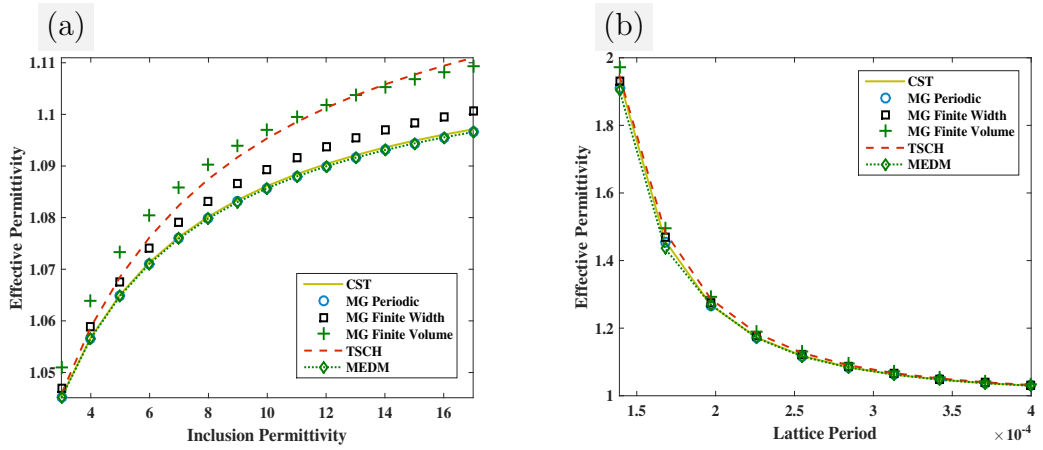

Figure 6.1: Effective permittivity extraction of a periodic material using various homogenization techniques. We used full wave finite element method to simulate based Nicolson Ross Weir (FEM-NRW) technique, Maxwell-Garnett (MG) periodic, MG finite along one dimension (z-direction), MG finite (finite along each direction), two scale convergence homogenization (TSCH) technique and the proposed technique (MEDM) to extract the effective parameters. A cubic sample of the composite is considered, and the full geometric and simulation settings are given in Table 6.1. (a) Effective permittivity as a function of the permittivity of the inclusion material. The lattice period d is three-times the edge-length of the basis a (b) Effective permittivity as a function of the lattice period. Relative permittivity of the inclusion is 6.

differences among various homogenization schemes(Fig. 6.1).

We used Maxwell-Garnett for fully periodic medium (unit-cell, volume fraction $f = a^3/d^3$), finite width $h = (N-1)d + a$ in z direction ($f = Na^3/hd^2$), and finite size in three dimensions ($f = (Na)^3/h^3$). The proposed scheme involved a finite volume of periodic scatterers in three orthogonal dimensions and considered a unit-cell in the centre of the array to include a considerable amount of interaction with the neighbouring scatterers. The effective permittivity calculations (Eq. 6.3) thus resulted in close agreement to that of the existing schemes, except close to high volume fraction of inclusion to host (Fig. 6.1b), where the problem is a poor approximation of the local field (Eq. 2.4). Bearing in mind the electrostatic nature of the

MG, we compared it to the proposed homogenization scheme and found promising results even for smaller lattice constant and high dielectric contrast between the inclusion and background media. Though the TSCH scheme has the ability to discretize arbitrarily shaped objects in periodic boundary condition settings, we found it not as accurate as the MG or MEDM.

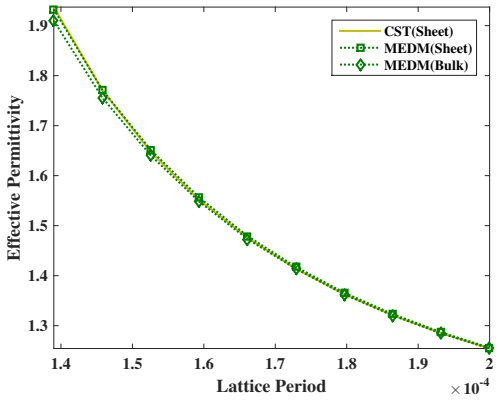

Figure 6.2: The effect of the finite thickness of the sample on the extracted parameters. The extracted permittivity of two-dimensional arrangement of scatterers (in good agreement for both CST and the proposed scheme) is higher than the bulk permittivity. Full geometric and simulation settings are the same as Fig. 6.1b except the single layer consideration.

For numerical homogenization, we used periodic boundary conditions in two orthogonal axes that are perpendicular to the plane of incidence and used finite size array (5-layers) in the plane of incidence. The results can be discerned from the MEDM due to the finite size of the array in the incidence plane, which treats the material as a film rather than bulk. To explain this in more detail, we considered a single layer of scatterers periodic in the other two dimensions; we observed that the effective permittivity is higher in the case of sheet and approaches to that of the bulk permittivity when the interaction from the neighbouring layers is considered as shown in Fig. 6.2. The results are consistent to that of the published data which claims that the effective parameter values are higher in sheets and reduce to that of bulk parameter values when the contribution from the neighbouring layers

is considered [91]. A commercial electromagnetic software (CST) was used in the frequency domain to extract the effective parameters. The CST simulation time (21 seconds) was comparable to that of the MEDM (19 seconds), which was implemented in Matlab. The computer having the following specifications was used: CORE(TM) i7-3770CPU@3.4GHz processor and 16 GB of RAM. We will demonstrate in the following subsection that the simulation time improves dramatically in simulating inhomogeneous composites such as composite gradients, where the commercial software can not leverage the computations by applying the periodic boundary conditions.

6.4.1 Gradient Index Materials

Consider a rectangular sample of spherical scatterers as discussed in the previous section, but now we consider periodic conditions along the two orthogonal directions, while a logarithmically varying period along the third orthogonal direction (z-axis) of a Cartesian coordinate system.

The homogenization calculations along gradient direction revealed that the effective permittivity is a function of the spacing between the scatterers: it varies from high (close to the greater concentration extent of the scatters) to low (close to the lower concentration of the scatters) depending on the concentration of the inclusions. In comparison, the MG calculations provided relatively poor approximations of the extracted parameters, particularly close to the higher concentration of the scatterers and close to the edges of the considered specimen. We demonstrated this by extracting the scattering parameters of the gradient material. The simulation setup consisted of a waveguide filled with a material of relative permittivity equal to four. A sample of thickness 'd' along the gradient direction(Fig. 6.3a) was inserted at a zero phase reflection location in the waveguide. The extracted reflection parameters

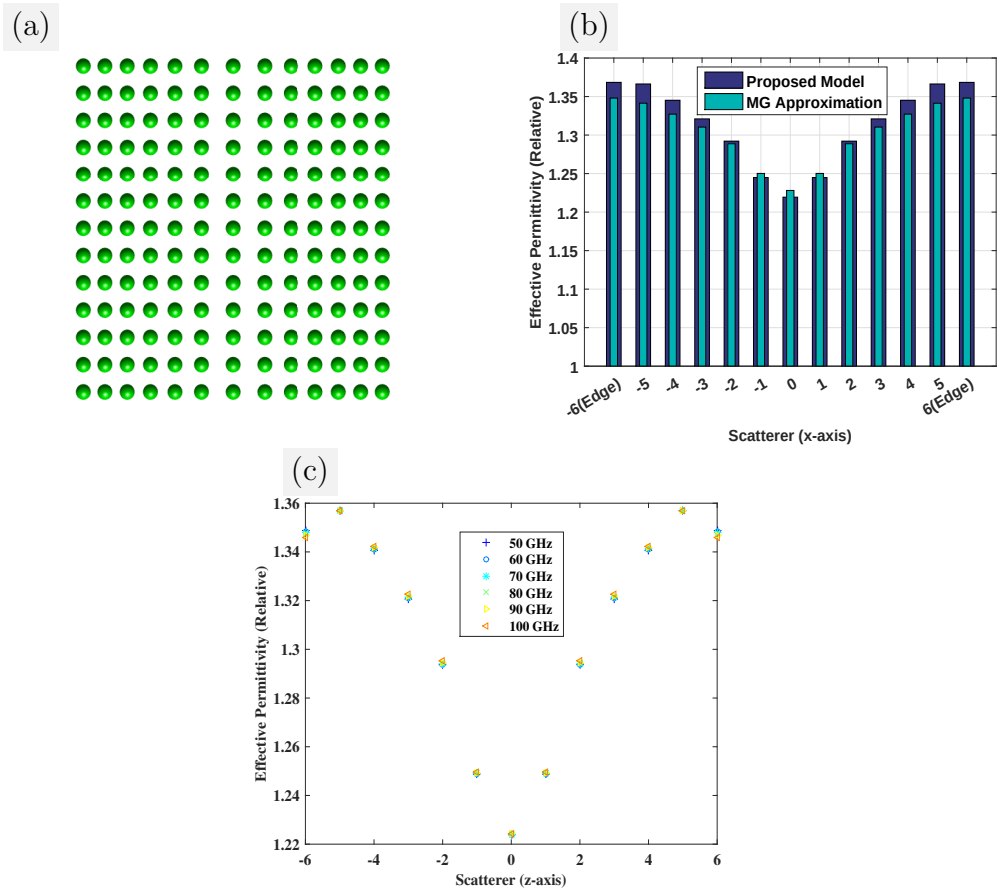

Figure 6.3: Effective permittivity of a gradient material; lattice spacing along x- and y-directions is fixed, but variable along the z-direction. See Table 6.1 for the simulation parameters. (a) Fixed lattice spacing along x- and y-axis, but varies logarithmically along the z-direction (horizontal axis) of the Cartesian coordinate system (b) Effective permittivity of the gradient material (c) Frequency dependence of the effective permittivity layers.

of the actual geometry and that of the equivalent slabs of the extracted permittivity agree as expected, but the MG model was found less accurate in comparison to the proposed scheme. A similar material of interest is a material which has a higher permittivity in the centre and logarithmically reduces to a minimum close to its edges as in Fig. 6.4a. Though we found it difficult to simulate the finite size geometry of 13×13×13 scatterers using a commercial software on a desktop computer having the following specifications: CORE(TM) i7-3770CPU@3.4GHz processor and 16 GB of RAM, the proposed scheme solved for the unknown currents in only 14.79 seconds on the same computer. For full specifications of the simulation parameters, see Table 6.1.

Table 6.1: Specifications of the simulated geometries. The superscript 3 indicates the periodicity in the three orthogonal directions; likewise for the superscript 2. Host relative permittivity is set to one in each case. $z^a \in \{178.62\ 182.16\ 189.40\ 198.45\ 211.95\ 241.70\ 263.30\ 241.70\ 211.95\ 198.45\ 189.40\ 182.16\ 178.62\}$ and $z^b \in \{228.16\ 224.44\ 216.38\ 206.71\ 194.17\ 172.77\ 158.58\ 172.77\ 194.17\ 206.71\ 216.38\ 224.44\ 228.16\}$

Figure Reference	Solution Frequency (Hz)	Scatterer Radius (μm)	Periodicity (μm)	Inclusion Permittivity (Rel.)
6.1a	100e6	62.035	$(300)^3$	3-17
6.1b	100e6	62.035	$(100-400)^3$	6
6.3b	100e9	62.035	$(215.44)^2 \times z^a$	20
6.4b	100e9	62.035	$(215.44)^2 \times z^b$	20

6.5 Random Medium

Apart from the periodic arrangement of the inclusion scatters, the proposed scheme allows calculating the accurate scattering due to randomly arranged scatters as

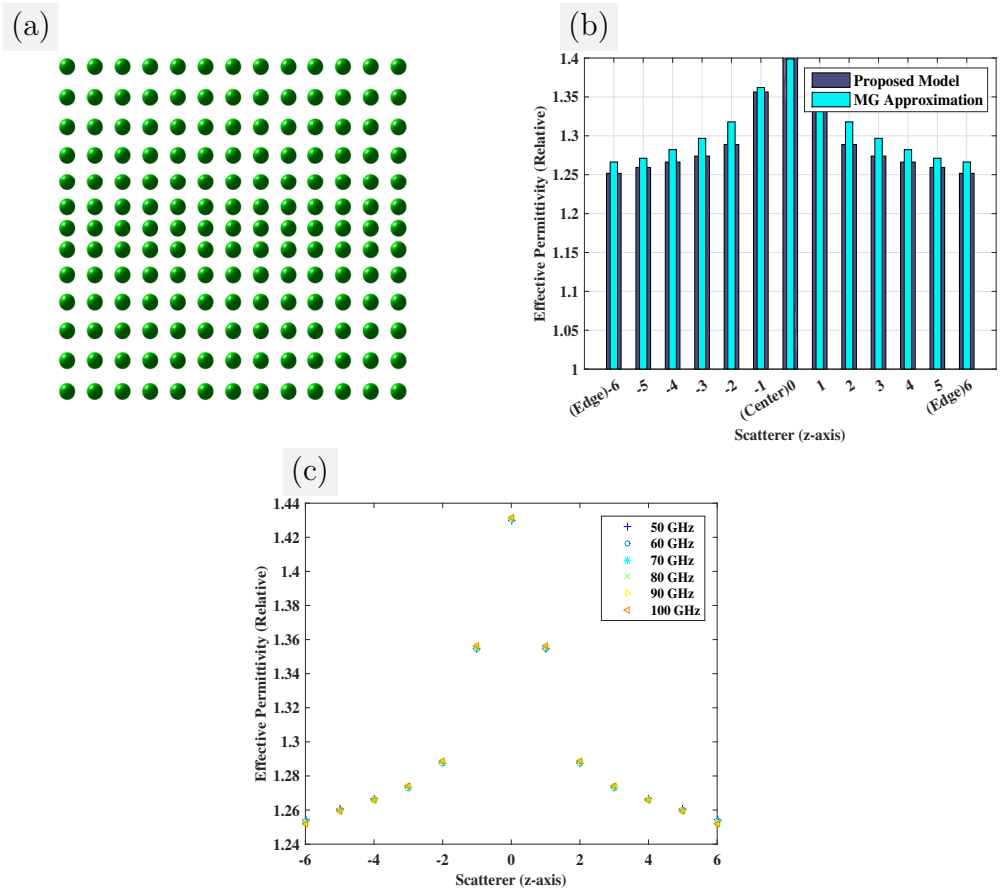

Figure 6.4: Effective permittivity of a gradient material; lattice spacing along x- and y-directions is fixed, but variable along the z-direction. See Table 6.1 for the simulation parameters. (a) Fixed lattice spacing along x- and y-axis, but varies logarithmically along the z-direction (horizontal axis) of the Cartesian coordinate system (b) Effective permittivity of the gradient material (c) Frequency dependence of the effective permittivity layers.

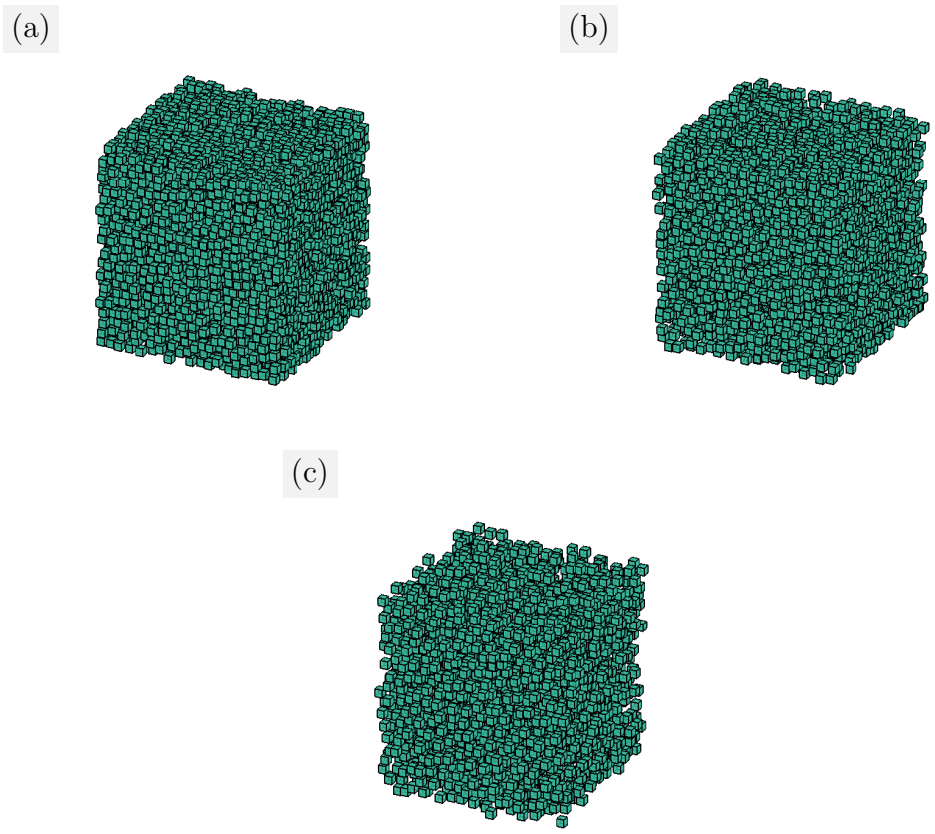

Figure 6.5: The geometry of the cube composed of cubic meta-atoms placed in a random arrangement according to a Gaussian distribution; the volume fraction is decreasing gradually as follows: (a) 0.1, (b) 0.2, (c) 0.3. The relative permittivity of the inclusions is 6, inclusion edge-length is 30mm, and sample-cube edge-length is 750mm.

well. For analysis, we fill a cubic specimen with randomly generated scatters using a Gaussian distribution. The scattering can be analysed in Fig. 6.6. As the volume fraction of the inclusion-to-host increases, the scattering inside the sample increases as well.

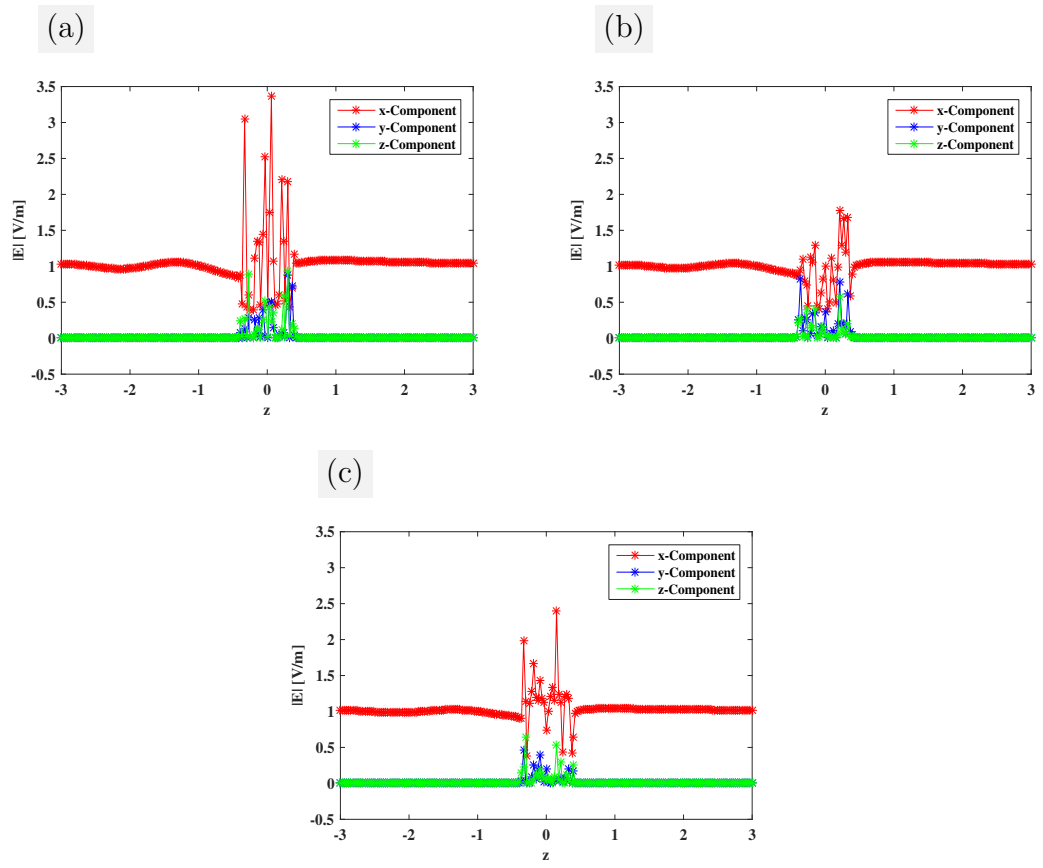

Figure 6.6: Computed values of absolute electric field scattered from random composites in Fig. 6.5 using the dipole averaging method. The operating frequency is 0.1GHz in each case. Absolute value of the scattered field along z-axis and passing through the centre of the cube of the following volume fractions: (a) 0.1 (b) 0.2 (c) 0.3.

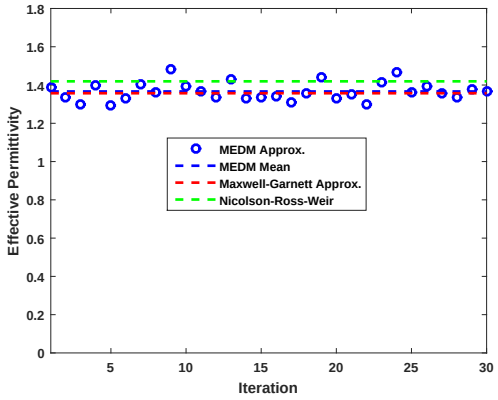

Figure 6.7: Effective permittivity values of a random composite using the dipole averaging method. The effective permittivity values are computed over a number of random arrangements of the inclusions, and the ensemble is averaged to get the effective permittivity of the random composite.

6.5.1 Homogenization of Random Materials

The local field in the interior of a random composite can be calculated by extracting a scatterer close to the centre of the sample. The field in the cavity region is then calculated for different samples of the randomly generated scatterers. The ensemble field can then be averaged in the case of uniformly distributed scatterers. The same averaging procedure is used to calculated the average equivalent current in the test scatterer, and the effective permittivity can be calculated by the application of the field consistency condition in this case as well. Figure 6.8 summarises our analysis of the variation of the inclusion to host permittivity, dielectric contrast and frequency.

Specifications of the simulated problems have been provided in Table 6.2.

6.5.2 Sample Size Consideration

The calculations used to generate the results given in Figs. 6.8 are based upon the finite size of the heterogeneous sample, which is cube-shaped. Accurate calculations

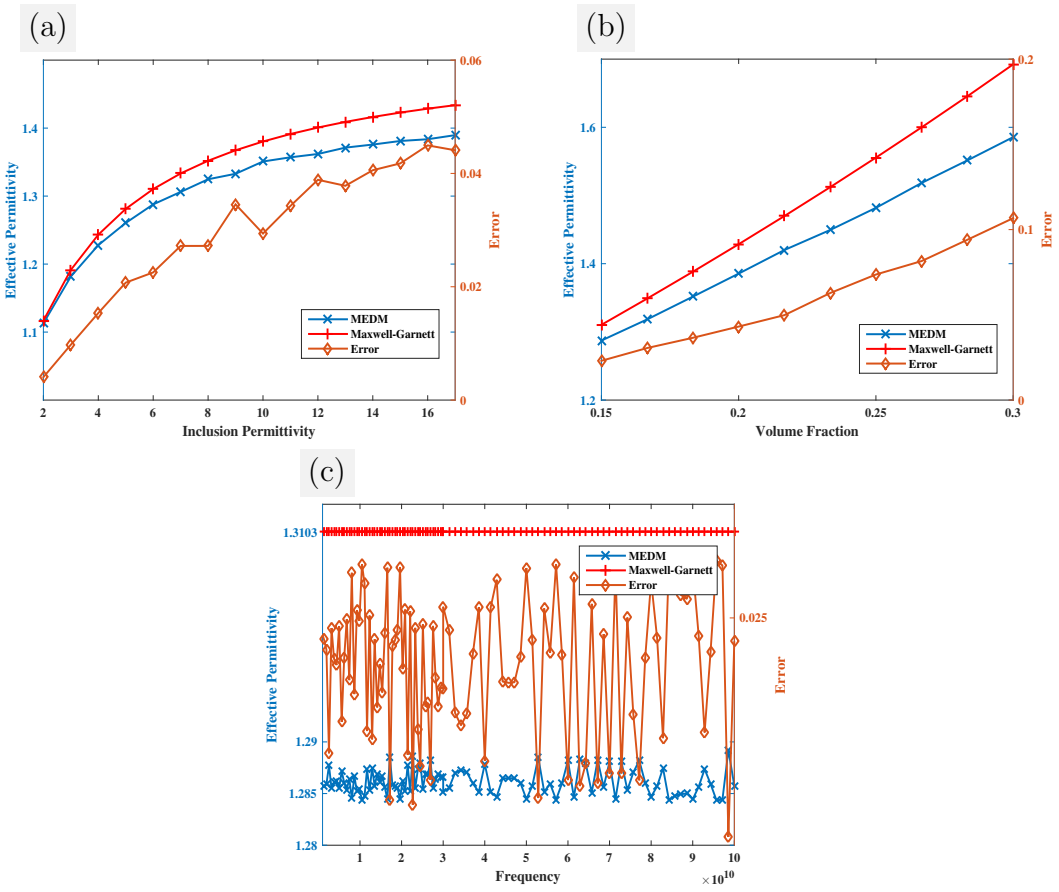

Figure 6.8: Effective permittivity extraction of a random material using the Maxwell-Garnett and the method of equivalent dipole moment. A cubic sample is considered whose characteristics are given in Table 6.1. (a) Effective permittivity as a function of the permittivity of the inclusion material (b) Effective permittivity as a function of the volume fraction of inclusion-to-host (c) Effective permittivity as a function of frequency.

Table 6.2: Specifications of the simulated problems.

Figure Reference	Solution Frequency (Hz)	Periodicity (μm)	Volume Fraction	Inclusion Permittivity (Rel.)
6.8a	1e6	N-A	0.15	2-17
6.8b	1e6	N-A	0.15-0.3	6

of the effective parameters, however, also involves the scattered field of the large-distance scatterers. In Fig. 6.9, we have demonstrated that long-distance scatterers do not contribute significantly at the centre of the sample. We, therefore, safely selected our sample size to 20x20x20 cubic scatterers. As discussed earlier that we consider a cubic sample for the effective-permittivity extraction, the analysis of the size of the box becomes indispensable for the accurate homogenization. We vary the size of the basis cube and observe its impact on the accuracy of the extracted homogenised permittivity. Based on these observations, it can be mentioned that only five immediate neighbours are enough for the accurate representation of the extracted permittivity as shown in Figure 6.9.

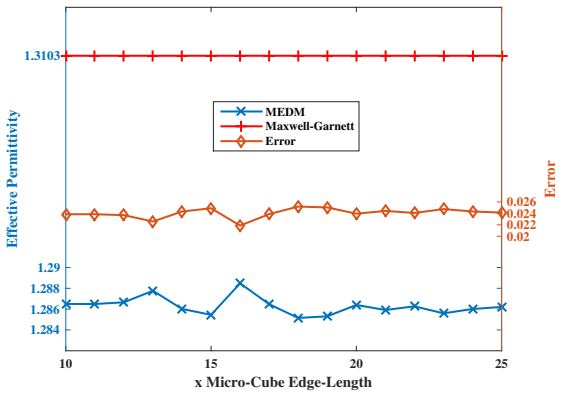

Figure 6.9: Analysis of the influence of the long distance scatterers at the test scatterer. The horizontal axis represents the increase in the edge-length of the cubic sample in terms of the edge-length of the cubic scatterer. Ten iterations were averaged to calculate each data sample. For specifications of the considered problem, see Table 6.1

6.6 Sphere Versus Cube

In this section, we prove via a rigorous mathematical procedure that for an electrically small inclusion, the inclusion shape plays an insignificant role and for a sphere and a cube of the same volume, the dipole moment, and hence, the scattered field is

the same. Let us calculate the self-coupling term from a single scatterer. Using 4.29, we get:

$$\begin{aligned} Z &= \frac{a^3}{j\omega(\varepsilon - \varepsilon_0)} - \frac{a^3}{j\omega 3\varepsilon_0}, \\ &= a^3 \frac{2\varepsilon_0 + \varepsilon}{j\omega 3\varepsilon_0(\varepsilon - \varepsilon_0)} \end{aligned} \tag{6.7}$$

Matrix inversion equation gives:

$$\begin{aligned} \alpha &= Z^{-1}V, \\ &= \frac{j\omega 3\varepsilon_0(\varepsilon - \varepsilon_0)}{2\varepsilon_0 + \varepsilon}. \end{aligned} \tag{6.8}$$

Scattered field can then be calculated as a product of the unknown coefficient and the calculated scattered field:

$$\begin{aligned} E^s &= \frac{j\omega 3\varepsilon_0(\varepsilon - \varepsilon_0)}{2\varepsilon_0 + \varepsilon} \left(\frac{-1}{j\omega 3\varepsilon_0} \right), \\ &= -\frac{\varepsilon - \varepsilon_0}{2\varepsilon_0 + \varepsilon}. \end{aligned} \tag{6.9}$$

The total field inside the scatter can thus be given as:

$$\begin{aligned} E &= 1 - \frac{\varepsilon - \varepsilon_0}{2\varepsilon_0 + \varepsilon}, \\ &= \frac{3\varepsilon_0}{2\varepsilon_0 + \varepsilon}. \end{aligned} \tag{6.10}$$

The above equation is a well-known expression for the field internal to an-electrically-small spherical-scatterer.

6.7 Summary

Closed-form analytical expressions for material homogenization were proposed in the preceding chapter. Here we propose a field- and current-averaging approach based on the calculations in the point-dipole-based numerical-modelling scheme. The proposed method was theoretically demonstrated to be equally valid for both dielectric-

and metallic-scatterer-based composites. The effect of the inclusion-scatterer permittivity and the spacing between the scatterers has been analysed, and the results have been compared to various existing analytic and numerical homogenization schemes. It has also been demonstrated that the proposed scheme can accurately extract the permittivity of the composite surfaces, and the results were validated in comparison with that of a commercial software CST. It was also demonstrated that the homogenisation of gradient composites based on the closed-form MG formula is not as accurate as compared to that of the proposed full-wave point-dipole-based homogenization scheme. Several random structures based on the volume fraction have been simulated, and the scattered electric field has been analysed inside the material. The analysis allowed us to develop a random material homogenization scheme, and it was observed that the effective permittivity of a random material is smaller than that of the periodic materials. This phenomenon occurs due to the random scattering between the inclusions which results in the scattered-field values flip-flop between negative and positive field. It was also observed that only a few neighbouring scatters contribute to an effective value of the permittivity.

Chapter 7

Applications of the Proposed Homogenisation Scheme

We propose a material design scheme based on the homogenization techniques for periodic and random materials. The proposed scheme is demonstrated (and validated) to extract the effective properties of gradient composites. Materials with the desired EM properties are suggested to design by tweaking the geometric parameters and properties of the participating materials. Towards this end, material parameters such as lattice constant, scatterer size and permittivity are varied in periodic materials, and the volume fraction and scatterer properties are changed in random materials; and the trends in the effective properties are analysed.

7.1 Introduction

Broadband control over electromagnetic (EM) waves is challenging and long sought due to a variety of disruptive applications, a few of which have been proposed even before the inception of Maxwell's equations such as Maxwell's Fisheye lens (an imag-

ing device). A variant of the Fisheye lens called a Lüneburg lens (a beam focusing or point source collimating device) was proposed in 1944 [92]. A Lüneburg lens has a variety of applications including satellite communications. It can formulate multiple beams when multiple feeds are used for focussing the radiation beams in different directions. The interest in this field has been heightened in the recent past due to speculated possibility to engineer the left-handed metamaterials, or to allow for continuously varying material properties to steer the incident wave at will such as for the transformation optics (TO) [10]. Certain beamforming or direction of arrival estimation schemes require flattening of the annular focal surface of a Lüneburg lens, which can be achieved by using the TO [93, 94], this flattened surface covers the focal point of the plane wave incident from wider scan angles. The TO scheme is primarily limited by the permittivity and permeability values that are inhomogeneous and anisotropic, and even due to the demand on the refractive index values that are less than one, which renders this scheme inherently narrowband. A quasi-conformal mapping technique can be applied to mitigate the anisotropy in graded permittivity in the TO formulation, but it is an approximation which results at the cost of slight performance degradation [95]. Alternatively, to mitigate the anisotropy, as well as the permeability requirements, a field transformation scheme, was proposed [81], which relies only on isotropic permittivity values in graded permittivity profile to guide the incoming wave in the desired direction as well as to control the phases of the incoming and outgoing waves. The posed challenges for inhomogeneous permittivity realisation include the limitations of numerical modelling tools for rapid analysis of the design scheme and limitations of manufacturing techniques. We propose to design materials using composites: the desired electromagnetic properties can be engineered by judiciously varying the volume fraction of the inclusion-to-host materials, by manipulating the geometric arrangement of inclusions, or by altering their dielectric contrast [84]. The analysis of the interaction between the electromagnetic wave with the scatter-based composite is usually performed by representing the

composite as a continuum [96] and using the commercial full-wave electromagnetics software for the simulation. Herein, we opt to use a full-wave dipole-moment-based method (presented in Chapter 3) for the precise analysis of the interaction between the incident wave and the inclusion scatterers in the composite.

A Lüneburg lens can be compressed using the transformation electromagnetics techniques, a slim version of the lens has been proposed in the Refs. [97], [98]. A beam steering function using a patch antenna was achieved by varying the feeding antenna across lens dimensions. The transformation optics design proposed in Ref. [99] produces flat Lüneburg lens by manually setting the transformed permittivity values that are less than unity to one. However, the proposed homogenization design using plasmonic scatterers allows us to achieve even permittivity values that are less than one. The use of dielectric materials for the lens fabrication results in a wider operational bandwidth of the device [100], [14].

We demonstrate the applicability of the proposed scheme by designing a composite-based Lüneburg lens. The variation in permittivity can be achieved by drilling holes in finite-thick dielectric slices in such a manner that the hole size is small in the centre and radially increases till the edge [101]. Though the underlying principle to achieve the effective response of this material is acceptable, but the cost and time involved (drilling different sized holes in different slices and then etching them back so as to form the radial lens) is unsuitable for the application at hand. Further, the scheme itself is intricate to design spherically symmetric lens. Besides, the performance of the design would be limited by the size of the holes, that is, the operating wavelength must be at least one-tenth of the size of the largest hole in the structure for a satisfactory operation of the device. Similarly, graded photonic crystals have complex design requirements, that is, the crystal size varies from centre till the edge [102]. Recent advances in the 3D printing or additive manufacturing prompted photopolymer jetting to design the lens by considering a unit-cell and

then radially varying the size of that cell to achieve a variable permittivity for the desired design [103]. The unit-cell used is usually direction dependent and, hence, results in spatial dispersion and limitations on the operating frequency.

In optics, the materials requiring continuously varying permittivity profile can be engineered using plasmonic inclusions imbued in a background material. One such realisation in two-dimensions has been mentioned in [104]. However, despite many papers have been published demonstrating a Lüneburg lens in the microwave regime, a manufacturing scheme for a 3D Lüneburg lens in the visible has never been demonstrated in the visible frequency range, in the authors' knowledge. One realisation at 48THz has been proposed using the same concept as the 3D printed Lüneburg lens in the microwaves [105], that is, by linearly varying the dimensions of the unit cell from the centre till the edge; principally, the unit-cell used is inherently direction and polarisation dependent.

In the following section, we introduce the principles of the composite design and the fundamentals of the Lüneburg lens. Unlike metamaterials, the unit-cell (in the composite) has been employed to perform below the resonance frequency, whereby low-loss and broadband operation of the composite has been achieved.

7.2 Principle and design of composites

A Lüneburg lens is a device that collimates the rays of a point source at the input of the lens by controlling the permittivity of the lens so as to follow the Fermat's principle. The permittivity profile of a conventional Lüneburg lens is expressed as follows:

$$\varepsilon_1 = 2 - \left(\frac{r}{R}\right)^2, \tag{7.1}$$

where r denotes the radial variation from the center(high permittivity) till the edge(ambient permittivity) and R denotes the lens radius. The realization of continuously varying permittivity is usually performed by discretizing the permittivity profile into small portions. This results in the graded permittivity profile:

$$\varepsilon_{ln} = 2 - \left(\frac{r_n}{R}\right)^2, \tag{7.2}$$

where $R = N\Delta r$, N is the total number of layers and $n(\in \{1, \ldots, N\})$ denotes the indexed layer; the preceding considerations result in $r_n = n\Delta r - \Delta r/2$, and by substituting these equivalent expressions in Eq. 7.2, we get:

$$\begin{aligned} \varepsilon_{ln} &= 2 - \left(\frac{n\Delta r - \Delta/2}{R}\right)^2, \\ &= 2 - \left(\frac{2n-1}{2N}\right)^2. \end{aligned} \tag{7.3}$$

We propose to design each layer of the indexed permittivity profile by a controlled

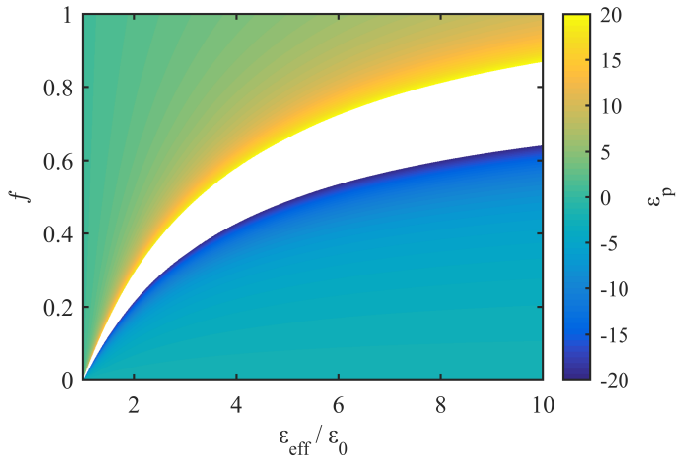

Figure 7.1: Selection rules for the effective permittivity modelling. A desired value of the effective permittivity can be achieved by using either dielectric inclusions (in microwaves) or plasmonic inclusions (in optics). Dielectric inclusions require higher volume fraction as compared to that of plasmonic inclusions. Both the dielectric and plasmonic inclusions are considered lossless.)

variation of the volume fraction of the inclusion-to-host. Unlike discretized material-layers [such as in Figure 7.2a], the random arrangement of scatterers and variation in

the volume fraction allows for the seamless transition of the EM waves. We recall the Maxwell-Garnett technique to find the appropriate volume fraction of the scatterers in a host medium for realizing the discretized permittivity values given in Eq. 7.3. The MG formula describes the effective permittivity of the composite in terms of the permittivity of the inclusion scatterers and volume fraction of inclusions-to-host media as follows [96]:

$$\frac{\varepsilon_{\text{eff}} - \varepsilon_0}{\varepsilon_{\text{eff}} + 2\varepsilon_0} = f\frac{\varepsilon_0\varepsilon_{\text{p}} - \varepsilon_0}{\varepsilon_0\varepsilon_{\text{p}} + 2\varepsilon_0}, \tag{7.4}$$

where $f = n_0 v_0$ represents the volume fraction of inclusion-to-host, v_0 is the volume of an inclusion scatterer, n_0 is the total number of inclusion scatterers per unit volume, ε_{r} is the permittivity of the inclusion scatterers, and ε_0 is the permittivity of the host medium. The above equation can be cast to express the effective permittivity of the composite in terms of the polarizability [Clausius-Mossoti (CM) formula] of a standalone scatterer (α) as:

$$\varepsilon_{\text{eff}} = \varepsilon_0\left(\frac{1 + \frac{2n_0\alpha}{3\varepsilon_0}}{1 - \frac{n_0\alpha}{3\varepsilon_0}}\right), \tag{7.5a}$$

$$= \varepsilon_0\left(-2 + \frac{3\varepsilon_0\varepsilon_{\text{p}} + 6\varepsilon_0}{\varepsilon_0\varepsilon_{\text{p}} + 2\varepsilon_0 - f(\varepsilon_0\varepsilon_{\text{p}} - \varepsilon_0)}\right), \tag{7.5b}$$

where the polarizability of a stand-alone scatterer is:

$$\alpha = 3\varepsilon_0 v_0\frac{\varepsilon_0\varepsilon_{\text{p}} - \varepsilon_0}{\varepsilon_0\varepsilon_{\text{p}} + 2\varepsilon_0}. \tag{7.6}$$

The MG and CM formulas (Eqs. 7.4 and 7.5) can be rearranged to express the inclusion-to-host volume fraction in the following forms:

$$f = \frac{\varepsilon_{\text{eff}} - \varepsilon_0}{\varepsilon_{\text{eff}} + 2\varepsilon_0}\left(\frac{3\varepsilon_0 v_0}{\alpha}\right), \tag{7.7a}$$

$$= \frac{\varepsilon_{\text{eff}} - \varepsilon_0}{\varepsilon_{\text{eff}} + 2\varepsilon_0}\left(\frac{\varepsilon_0\varepsilon_{\text{p}} + 2\varepsilon_0}{\varepsilon_0\varepsilon_{\text{p}} - \varepsilon_0}\right), \tag{7.7b}$$

$$= \frac{\varepsilon_0\varepsilon_{\text{p}} + 2\varepsilon_0}{\varepsilon_0\varepsilon_{\text{p}} - \varepsilon_0}\left(1 - \frac{3\varepsilon_0}{\varepsilon_{\text{eff}} + 2\varepsilon_0}\right). \tag{7.7c}$$

Further equivalents of the above expressions can be derived, which could provide useful caveats while selecting the suitable inclusion particles and the effective permittivity of the composite. In essence, by using the MG (Eq. 7.4), we can express

the scatterer permittivity in terms of the effective permittivity and volume fraction as:

$$\varepsilon_0\varepsilon_{\mathrm{p}} = \frac{\varepsilon_0 f(\varepsilon_{\mathrm{eff}} + 2\varepsilon_0) + 2\varepsilon_0(\varepsilon_{\mathrm{eff}} - \varepsilon_0)}{f(\varepsilon_{\mathrm{eff}} + 2\varepsilon_0) + \varepsilon_0 - \varepsilon_{\mathrm{eff}}}. \tag{7.8}$$

Analysis of the relationships among the effective permittivity, volume fraction, and the permittivity of the inclusion-scatterers (Eq. 7.8, Figure 7.1) reveals that instead of varying the volume fraction of the inclusions-to-host media to realise the desired values of the effective permittivity, we can change the permittivity of the inclusion-scatterers. In conventional dielectrics, the higher the volume fraction, the lower the value of the desired inclusion-scatterer permittivity is to achieve a particular value of the effective permittivity level of the homogenised material. In principle, a desired value of the effective permittivity can be realised by tuning the volume-fraction and permittivity values of the inclusions, but we also observe that by employing the plasmonic inclusions the desired effective value of the permittivity can be achieved at lower volume fractions of the inclusions. The underlying physics principle is that the plasmonic inclusions cover a wider scattering cross-section as compared to that of conventional dielectrics. The disadvantage of using plasmonic scatterers, however, is that the desired values of permittivity with low-loss can be obtained in optics regime only. Further, plasmonic inclusions involve higher dispersion rates [84]. Nonetheless, if the application at hand requires a narrowband operation in optics, plasmonic inclusions are still a suitable option. The proposed scheme allows tuning the values of the effective permittivity only by varying the fraction of the inclusions in the mixture. This procedure is cost and time effective as compared to the additive 3D printing techniques, where the size of the unit cell needs to be varied in the radial direction [106].

For the plasmonic composites, we can imbue small-sized plasmonic-scatterers in a background medium. The permittivity of a plasmonic material can be calculated

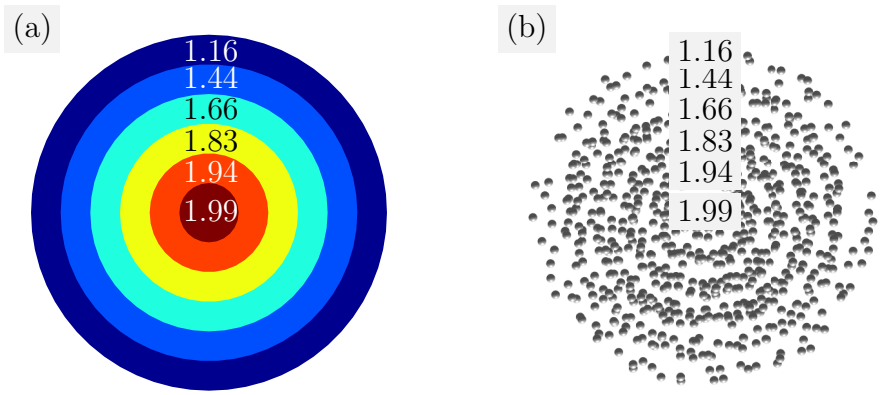

Figure 7.2: Graded-permittivity profile of Lüneburg lens using six layers. The graded permittivity in each layer is the homogenized version of the permittivity value in the center of the layer. (a) Lüneburg lens profile using 6 discrete dielectric layers. The labeled numbers represent the effective values of the relative permittivities of the discretized rings. (b) Lüneburg lens graded-permittivity profile using six distinct composite layers. The graded permittivity in each layer is the homogenized version of the permittivity value in the center of the layer.

by free-electron Drude model as:

$$\varepsilon_{\mathrm{p}}(\omega) \approx \varepsilon_{\mathrm{b}} - \frac{\omega_{\mathrm{p}}^2}{\omega(\omega + i\tau^{-1})}, \tag{7.9}$$

where ε_{b} is the background polarization of the plasmonic cores, $\omega_{\mathrm{p}} = \sqrt{ne^2/m_0\varepsilon_0}$ is the plasma frequency, τ^{-1} is the relaxation rate of the free-electron movement, and m_0 is the free electron mass. Relaxation rate of the free electrons corresponds to the loss and the term $\omega\tau^{-1}$ decreases in comparison with ω^2 with an increase in frequency, rendering the loss suppression at relatively high frequencies (for gold and silver in optics), which limits the practical-design manifestation to optics only.

7.3 Result and discussions

A Lüneburg lens using six discrete dielectric layers has been designed in the microwaves (at 4GHz), where the lens radius is 2λ, the inclusion-scatterer radius is 0.0414λ, and the inclusion relative permittivity is 40. A Hertzian dipole was placed at a focal point of the lens to form a beam in the direction of the lens. The design resulted in about 30 thousand inclusion scatterers, which rendered the numerical solution using a commercial software intractable; because a commercial software needs to discretize each inclusion scatterer using surface basis functions [usually Rao-Wilton-Glisson (RWG) basis], which dramatically increases the computational complexity. To prevent the computational breakdown in such problems, we treat each scatterer as a dipole to calculate the coupling between the individual scatterers and to calculate the self-coupling term analytically. The point-dipole model allows the precise solution to the full-wave mathematical formulation by matrix inversion method as in the method of moments (MoM).

The near-field calculations of the field values using the proposed random-scatterer-based scheme have been compared with those of discrete-layer-lens simulation in a commercial EM software CST (see Figure 7.3). Packing a high volume fraction of spherical inclusions in a random order was challenging for higher volume fractions, especially in the centre of the lens, which required to relaxed the volume fraction limit and resulted in a small phase delay at the output of the lens. But due to the large scattering cross-section of the plasmonic lens, exact volume fraction was permitted and, hence, relatively small delay in the output of the lens in comparison with the delay at the output of dielectric-inclusion-based lens. Besides, the design parameters based on the MG are approximate, and the approximation relaxes accuracy particularly for densely packed and randomly distributed inclusion particles because the MG rests on the calculations using periodically arranged scatterers; and its validity is limited to electrostatics only, though it can be well-approximated in a

quasi-static limit. The lens operation as well as the focus is more obvious in Fig. 7.4.

The proposed scheme provides a means to realise composite designs based on off-the-shelf materials. In microwaves, zirconium tin titanate (ZST, chemical formula: $Zr_{0.8}Sn_{0.2}TiO_4$) ceramic can be synthesised to achieve a relative dielectric constant of 37.1 for a quality factor of 5000 at 10GHz [107]. Small-sized dielectric scatterers of the ZST can be dispersed into a low-dielectric matrix to design volume-fraction-based EM devices. We scale the lens parameters mentioned in the preceding paragraphs for practical realisation of the proposed lens design. The lens radius is 2λ, and the inclusion particle radius is 0.0414λ. The location of the excitation source (a Hertzian dipole) is varied along the focal curve in the azimuthal plane from 180° to 360° in 10 equal steps (see Figure 7.6). The average antenna gain in the direction of the lens is 16.38dB (standard deviation is 0.32dB) when the radius of the lens is 2λ. The half power beamwidth(HPBW) of the lens is 14.32°, while the first significant sidelobe occurred about 14dB below the main beam. A small standard deviation from a mean value of the gain was observed while scanning the beam due to the random nature of the device, but this dispersion can be compromised in comparison with the periodic structure based devices [108]. The gain increases with an increase in the size of the lens, and for a radius of 2.5λ, the gain rose to 18.82dB. Unlike the Lüneburg lens manifestation based on the additive manufacturing techniques, the proposed scheme is independent of the polarisation in the tangent plane of the lens and can scan any direction in space, based on the location of the input source at the focal point of the lens. Further, the homogenised response of the scatterers still engenders an aberration-free operation of the lens both in microwaves and optics. The frequency dependence of the lens has been demonstrated in Figure 7.8. The gain of the lens increases with increase in the size of the lens and vice versa.

The plasmonic inclusions are demonstrated to yield the similar result as dielectric inclusions (see Figure 7.3b), though at a low volume fraction of inclusions-to-host.

The proposed lens design can be translated into the optics regime, where we make use of low-loss plasmonic inclusions to demonstrate the functionality of the Lüneburg lens. The inclusion-nanoparticle permittivity can be calculated via Eq. 7.9 and the parameter values used were the following: $\omega_p = 2\pi \times 2.15e15$Hz, $\hbar\tau^{-1} = 0.5$ [109] is the phenomenological electron-motion damping rate adjusted to match the imaginary part of ε. We choose the permittivity value at 429.8THz, because at this frequency the gold permittivity has low loss value, as demonstrated by the experimental results as well. The relative value of the calculated permittivity using Eq. 7.9 is -16 and that of the imaginary part (extinction coefficient) is 0.7033. Gold (Au) nanoparticles of diameter 93nm were used to obtain the same feature as a composite with dielectric scatterers in microwaves. Gold nanoparticle-based composites, however, are much more dispersive(as evident from Eq. 7.9) and there exist only certain values of frequency where low-loss permittivity can be achieved. The demonstrated optical lens can perform, therefore, in a narrow frequency band only. The gain of the proposed optical Lüneburg lens for different scan angles has been shown in Figure 7.7 for a lens of diameter 2.8μm. The mean antenna gain in the direction of the lens is about 17.62dB when the radius of the lens is 2λ and the source is varied in the azimuthal plane, similar to the gain of a microwave lens of diameter 2λ, but the standard deviation of the average gain values (0.22dB) is smaller than that of a microwave lens(0.32dB) because of the large cross-sectional area of the plasmonic scatterers. Further, the gain increased with an increase in the size of the lens, and for a radius of 2.5λ, the gain increased to 19dB. Moreover, the frequency dependence of the optical lens has been demonstrated in Fig. 7.9. The Drude model was used to cater for the frequency dependence of the inclusions. Unlike the microwave Lüneburg lens, the gain of the optical Lüneburg lens increased with increase in frequency and then decreases after certain frequency due to Drude model response of the inclusions.

A Lüneburg lens that is flat on one side can be used in a variety of applications.

One such application may include capturing the panoramic view using a handheld device(a mobile phone, for instance) without the need to move the device manually. Also, the proposed lens design may usher in control over wireless power transfer, the desired functionality for charging wireless handheld devices.

The proposed scatterer-host volume-fraction-based scheme is universal and applies to the geometries that are tweaked to perform a different EM function, for instance, a Lüneburg lens with a flat focal surface for electronic beam scanning application [110] and even for an all-dielectric TO cloak realisation [111]. The host is free-space in all the designs mentioned in this section.

7.4 Summary

A 2D-material design scheme was presented in Chapter 5, and a few applications of the homogenization scheme proposed. In this chapter, we discuss a material design scheme based on spherical scatterer-based 3D composites. It has been demonstrated that unlike 2D design scheme, where only dielectric inclusions are required to achieve a certain value of the permittivity, the 3D-design scheme allows us to achieve a specific value of permittivity by employing either dielectric (where the required volume fraction is relatively high) or plasmonic (where the required volume fraction is relatively low) inclusions. Based on the permittivity-selection rule a Lüneburg lens has been designed and simulated using both the dielectric and plasmonic inclusions, and both the dielectric- and plasmonic-inclusion-based design were in good agreement with each other. The results were further compared to that of the discrete layers design simulated in CST, and the agreement between the scatterer-based lens and that of the discrete layers lens was satisfactory. The 3D lens function was demonstrated for a beam forming application at a few frequency points; also, the lens function was demonstrated for the plane wave focussing application at a freq fre-

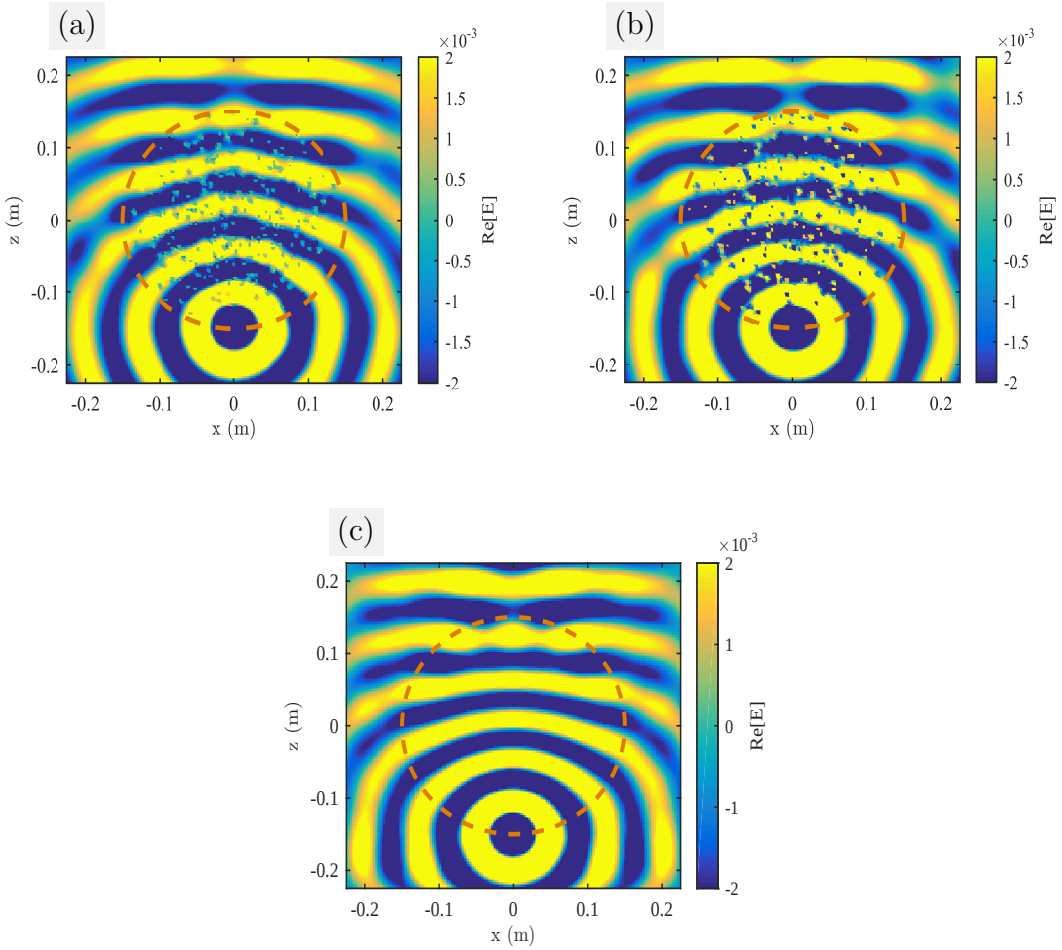

Figure 7.3: Component y of electric field values. The excitation source (a y-polarised Hertzian dipole) is placed at the focal point $(x = 0, y = 0, z = -0.18)$. The diameter of the lens is 0.34m and that of the scatterers is 0.006m. The relative permittivity of the inclusion scatterers is 40. Simulation frequency is 4GHz. (a) Near electric field in $y = 0$ plane using a composite based on dielectric inclusions (using point-dipole method) (b) Near electric field in $y = 0$ plane using a composite based on plasmonic inclusion (relative permittivity of -16) (c) Near electric field of dipole (with lens) in $y = 0$ plane at 4GHz using discrete dielectric layers in CST (commercial EM software).

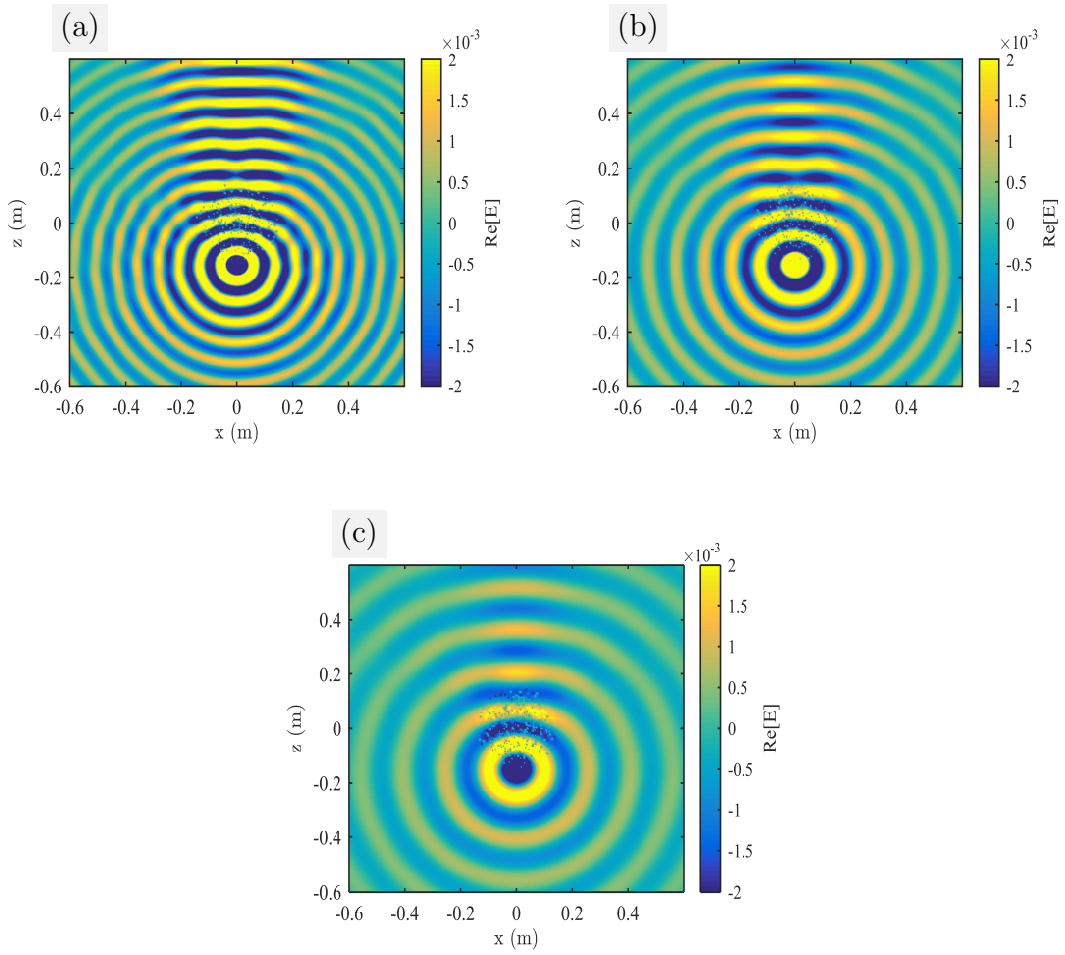

Figure 7.4: Component y of the electric-field. Dipole is placed at the focus ($x = 0, y = 0, z = -0.18$) and is polarized along y-axis. The lens is placed symmetrically at the origin of the Cartesian coordinate system. The diameter of the lens is 0.34m, and that of the scatterers is 0.006m. The relative permittivity of the scatterers is 40. (a) Dipole field (with lens) at 4GHz (b) Dipole field (with lens) at 3GHz (c) Dipole field (with lens) at 2GHz.

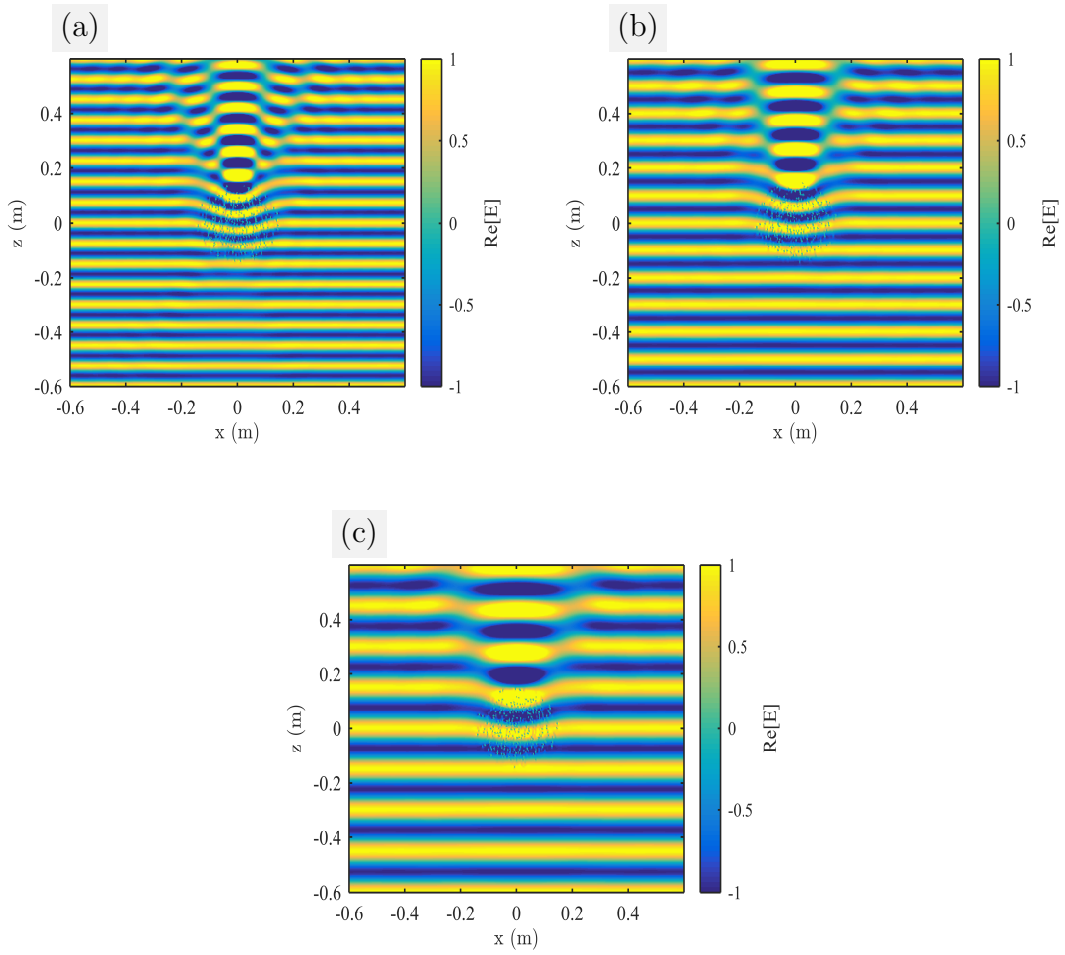

Figure 7.5: Component x of electric field values. The incident plane wave is polarized along x-axis. The diameter of the lens is 0.34m, and that of the scatterers is 0.006m. (a) A plane wave incident on the lens which is placed symmetrically at the origin of the Cartesian coordinate system. The wave frequency is 4GHz (b) A plane wave incident on the lens which is placed symmetrically at the origin of the Cartesian coordinate system. The wave frequency is 3GHz (c) A plane wave incident on the lens which is placed symmetrically at the origin of the Cartesian coordinate system. The wave frequency is 2GHz.

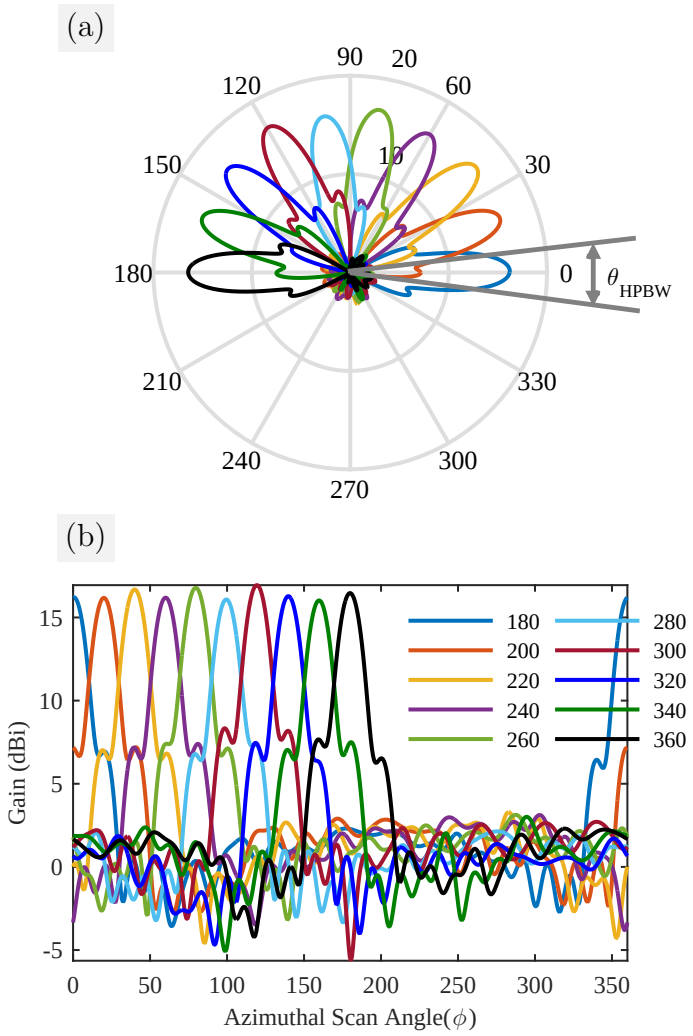

Figure 7.6: Dipole gain in the presence of a microwave Lüneburg lens. The lens radius is 2λ. The inclusion scatterer radius is 0.0414λ; the inclusion relative permittivity is 37.1 and the quality factor is 5000. A y-polarized dipole is varied on the focal curve in 10 steps (from 180° to 360°) in the azimuthal plane. The design was simulated at 10GHz. The legend in the linear plot indicates the source location angle in the azimuthal plane while the source is located at the surface of the lens. (a) Labels on the outer circle indicate the ϕ variation (in degrees) in the azimuthal plane, gain labels on circles are in dB, and the gain values below 0dB have been suppressed (b) Gain (Linear plot).

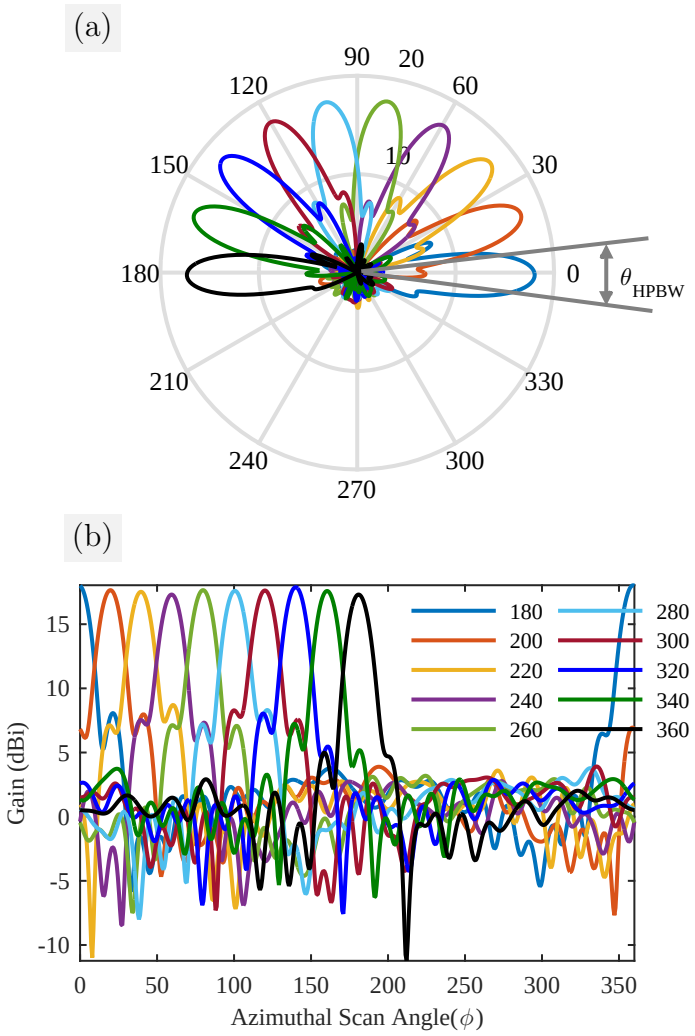

Figure 7.7: Dipole gain in the presence of an optical Lüneburg lens. The lens radius is 1.4um. The inclusion scatterer radius is 46.5nm; the inclusion relative permittivity is -16 and the imaginary part of permittivity is 0.7033. A y-polarized dipole is varied on the focal curve in 10 steps (from 180° to 360°) in the azimuthal plane. The design was simulated at 429.8THz. The legend in the linear plot indicates the source location angle in the azimuthal plane while the source is located at the surface of the lens. (a) Labels on the outer circle indicate the ϕ variation (in degrees) in the azimuthal plane, gain labels on circles are in dB, and the gain values below 0dB have been suppressed (b) Gain (Linear plot).

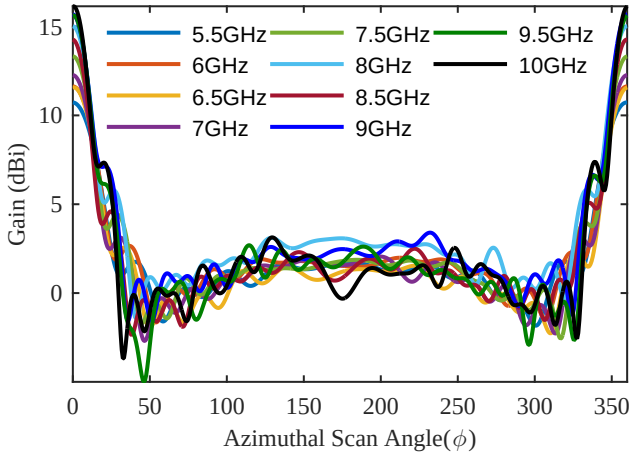

Figure 7.8: Dipole gain (from 5.5GHz to 10GHz in 10 equal steps) in the presence of a microwave Lüneburg lens. The lens radius is fixed to 2λ at 10GHz. The inclusion scatterer radius is 0.0414λ; the inclusion relative permittivity is 37.1 and the quality factor is 5000. A y-polarized dipole is placed in the azimuthal plane at $\phi = 180°$. The variable "f" indicates the simulation frequency.

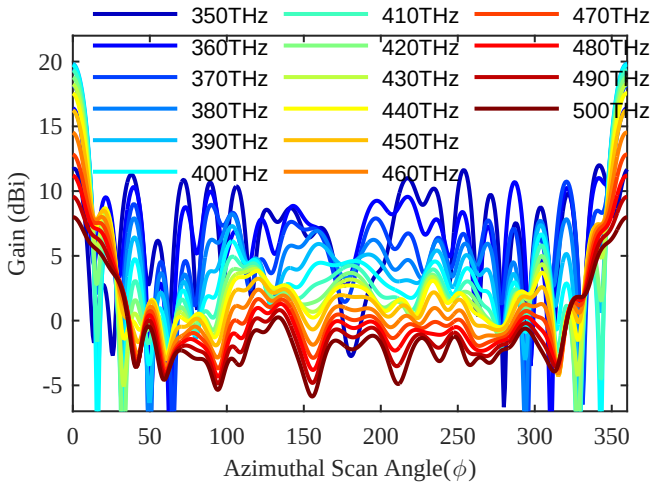

Figure 7.9: Dipole gain (from 350THz to 500THz in 16 equal steps) in the presence of a optical Lüneburg lens. The lens radius is fixed to 2λ at 429.8THz. The inclusion scatterer radius is 46.5nm; the inclusion relative permittivity is is calculated from the Drude model. A y-polarized dipole is placed in the azimuthal plane at $\phi = 180°$.

quency points. The lens yielded the expected value of the gain value, that is, 17dB. It was demonstrated that the proposed random-scatter-based lens design bears insignificant spatial dispersion as compared to that of the periodic-scatterer-based

designs. The lens function at various frequency points was displayed, and it was observed that the lens provides a reasonable value of the gain when its diameter is greater than or equal to 3 wavelengths.

Chapter 8

Frequency Dispersion in Material's Homogenization and EM Modelling

Homogenisation models perform accurately in the diffraction-limited regimes, but they can also be used to homogenise the arrays of resonant particles. We demonstrate the applicability of the proposed method at frequencies close to the resonances, and derive a closed-form expression for extracting the first resonance in inclusion scatterers.

8.1 Introduction

Kramers-Kronig relations (discussed in Chapter2) explain not only a tie in the bond between the real and imaginary parts of the complex dielectric function, but it also explains the dispersive nature of the dielectric function, that is, a change in the real part of the dielectric function must be compensated by the change in the dielectric

function of the rest of the frequencies, so that the total spectrum remains a constant.

Due to increasing number of applications requiring non-natural material properties (such as metamaterials), the research in this field has heightened, recently. Metallic resonance based materials are losing attraction due to ohmic losses incurred in the passive resonant structure [112]. Dielectric-composite-based resonances, however, are more attractive due to moderate losses in the homogenised material [113]. Materials with the desired properties can be synthesised, in principle, by mixing two or more distinct materials; and the permittivity of the resultant material can be tuned by varying the volume fraction, spatial arrangement, and the choice of the constituent materials [85]. We, therefore, opt to design dielectric materials to control the material dispersion so as to guide the incident wave (e.g., transformation optics), or to custom make materials using off-the-shelf materials. In general, material properties can be tuned by manipulating the volume fraction of the inclusion scatterers in a host medium according to a judicial or random placement [84]. However, the understanding of the electromagnetic waves interaction with the particles, constituting material, at microscale is one of the key aspects considered for designing the materials; and this requires accurate and computationally efficient numerical modelling techniques which are on a less firm footing at present.

Materials at the core level are composed of atoms, molecules or ions placed randomly (as in liquids and gases) or in a certain arrangement (as in solids), but those geometrical details can not be resolved at the visible wavelengths. This limitation is imposed by the diffraction limit of light which can be well-understood by the nature of Laplacian and Helmholtz fields [114]. At wavelengths larger than a quarter the length of the separation between two objects, the wave reflected off the objects can not distinguish between the objects at a distance farther from the object. On the contrary, the wavelengths shorter than the separation between the objects result in the radiation lobes or bandgaps. This can be well-understood by considering the

Green's function for Laplace and Helmholtz equations expanded in spherical harmonics [115]; for the observation distance R larger than the source distance R' from the reference origin, the static and dynamic multipolar expansion of the static and dynamic Green's functions can be given as:

$$\frac{1}{|\boldsymbol{r}-\boldsymbol{r}'|} = \sum_{n=0}^{\infty}\sum_{m=0}^{n} \epsilon_m \frac{(n-m)!}{(n+m)!} P_n^m(\cos\theta') P_n^m(\cos\theta) \cos m(\phi-\phi') \frac{(R')^n}{R^{n+1}}, \quad (8.1a)$$

$$\frac{e^{ik|\boldsymbol{r}-\boldsymbol{r}'|}}{|\boldsymbol{r}-\boldsymbol{r}'|} = -jk_0 \sum_{n=0}^{\infty}\sum_{m=0}^{n} \epsilon_m \frac{(n-m)!}{(n+m)!} P_n^m(\cos\theta') P_n^m(\cos\theta) \cos m(\phi - \phi')(2n+1) j_n(k_0R') h_n^{(2)}(k_0R), \quad (8.1b)$$

where ϵ_m is equal to 1 for $m = 0$, and 2 for $m \geq 1$. Replace R with R' and vice versa for $R < R'$. The angle information is contained in the Legendre polynomials P_n^m, while the intensity information is contained in the spherical Bessel and Hankel functions, which at large distances can be approximated as

$$j_n(k_0R) = \frac{1}{k_0R} \cos\left[k_0R - \frac{\pi}{2}(n+1)\right], \quad (8.2a)$$

$$h_n^{(2)}(k_0R) = \frac{i^{n+1}}{k_0R} e^{-ik_0R}. \quad (8.2b)$$

Laplacian Green's function, when expanded in spherical harmonics (Eq. 8.1a), clearly indicates a decay in the intensity ($1/R^{n+1}$) of the higher order multipoles at distances far from the source point. On the other hand, Helmholtz Green's function expansion in spherical harmonics (Eq. 8.1b) results in propagating modes: Hankel functions of the second kind ($h_n^{(2)}(k_0R)$) with increasing order according to the respective mode. The nature of Hankel and Bassel functions assures that the higher order modes contribute at long distances (cf. Eq. 8.2). With increasing order

of Hankel and Bessel functions, however, some spatial information is lost, which sets the limit that exact information contents of the scattered field can not be decoded at large distances even by the application of time-harmonic fields.

We discuss the diffraction limited (long-wavelength) regime only. There exist many analytical and numerical techniques to extract the properties of the resultant material, Nicolson-Ross-Weir method [87] and Maxwell-Garnett are one of the most prominent among them. We will review some of the classic homogenization techniques that are predominantly being used within the microwave community. Under these schemes, we derive closed-form expressions to represent a nanostructured material as a homogeneous object. Effective medium techniques have a long-standing history that dates back to 19th century when Ottaviano-Fabrizio Mossotti analysed the relationship between the dielectric constants of two different media and Rudolf Clausius derived an explicit expression in terms of indices of refraction of the host and inclusion materials [116, 117]. It was a contemporary work by four scientists who claimed independent contribution and therefore is named after quartet as Clausius-Mossotti or Lorentz-Lorenz equation.

One disadvantage of the application of electrostatics to the homogenization of heterogeneous materials is the loss of frequency-dependent information and the omission of the losses in the homogenised material. Frequency-dependent homogenization has been introduced to satisfy the Kramer-Kronig relations [118], but no mention of the loss computation was presented. A contemporary work by the same author introduced an analytical model for the homogenization that could take the electromagnetic coupling into account as well [119].

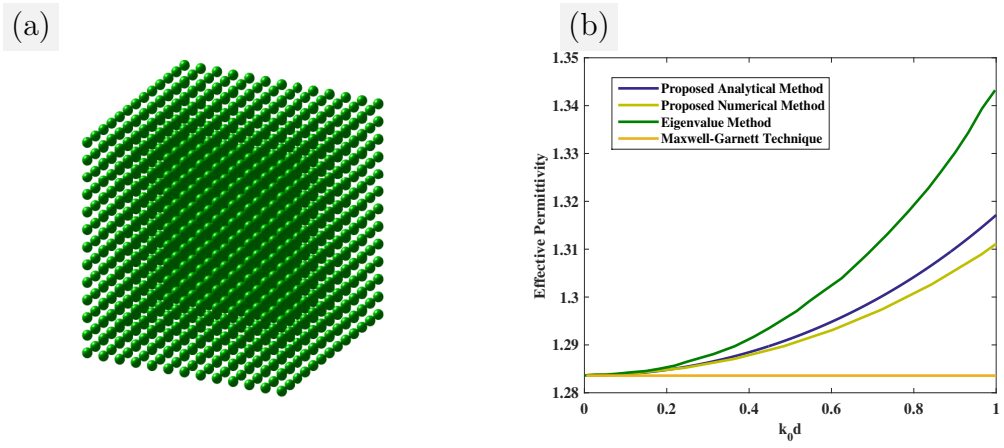

Figure 8.1: The dispersion characteristics of a three-dimensional arrangement of scatterers. The symbol k_0 denotes the free-space wavenumber and d denotes the period of the lattice. The relative permittivity of the inclusions is 20. The host medium is considered free space. (a) The EM scattering from a cubic arrangement of spherical meta-atoms in three dimensions. The radius of the inclusion is $62.03\mu m$. The lattice period is $215.44\mu m$ (b) Dispersion characteristics using the proposed analytical method, the proposed numerical method that also considers the coupling between the inclusions, the eigenvalue method presented in Ref. [120, 121], and the Maxwell-Garnett technique.

8.2 Dispersion in a Periodic Array of Scatterers

The dispersion characteristics of the three-dimensional periodic arrangement of scatterers (as discussed before) can also be studied using the proposed method. We compared the results generated by the proposed method to that of a full-wave extraction method and found that the proposed method, though considers only the fundamental harmonic in homogenization, can be used to extract the dispersion characteristics at relatively low frequencies [120].

It is evident that the proposed scheme extracts not only the real part of the permittivity, but it also extracts the imaginary part of permittivity and both are intimately related according to Kramers-Kronig relations.

The previous analysis involved analysis in a quasi-electrostatics regime. In contrast, the dispersion analysis includes the calculation of the higher order terms of the Taylor-series as well. At low frequencies, we can proceed with the calculation of the rest of the terms in the Taylor-series expansion.

Let us recall the expression for the field radiated by the equivalent current as follows:

$$\boldsymbol{E}^{\mathrm{s}}(\boldsymbol{r},\boldsymbol{J}_{\mathrm{eq}}) = \underbrace{-j\omega\mu_0 \iiint\limits_{\mathcal{V}} \boldsymbol{J}_{\mathrm{eq}}(\boldsymbol{r}')\frac{e^{-jk_0|\boldsymbol{r}-\boldsymbol{r}'|}}{4\pi|\boldsymbol{r}-\boldsymbol{r}'|}\,\mathrm{d}V'}_{\text{VP (Vector-Potential) Term}} \underbrace{-\frac{1}{j\omega\varepsilon_0}\iiint\limits_{\mathcal{V}} \boldsymbol{\nabla}'\cdot\boldsymbol{J}_{\mathrm{eq}}(\boldsymbol{r}')\boldsymbol{\nabla}'\left(\frac{e^{-jk_0|\boldsymbol{r}-\boldsymbol{r}'|}}{4\pi|\boldsymbol{r}-\boldsymbol{r}'|}\right)\mathrm{d}V'}_{\text{SP (Scalar-Potential) Term}}. \quad (8.3)$$

The kernel in the above equation represents a multipolar field (see the multipolar expansion in Eq. 8.1). An inspection of Eq. 8.1 reveals that only the basic dipolar-term contributes to the electric field at the centre of the sphere (observation point $\boldsymbol{r} = 0$) while the rest of the modes vanish at the centre of the sphere. So we evaluate only the contribution of the dipolar term and add the contribution of each wave harmonic from the radial plane wave.

Taylor series expression of the plane wave can be given (around $k_0R = 0$) as $e^{-jk_0R} = 1 - jk_0R - k_0^2R^2/2 + jk_0^3R^3/6 - k_0^4R^4/24 + \mathcal{O}(R^5)$. Substituting the series elements in the gradient of the Green's function, we get the following expression for the first four Taylor terms

$$\boldsymbol{\nabla}'\left(\frac{e^{-jk_0R}}{4\pi R}\right) = (\boldsymbol{r}-\boldsymbol{r}')\left[1 + k_0^2R^2/2 - jk_0^3R^3/3 - k_0^4R^4/8 + \mathcal{O}(R^5)\right]\frac{1}{4\pi R^3}, \quad (8.4)$$

We calculate the contribution of each term in the above equation towards calculating the scalar potential. The first term in the above equation involves singularity at the

origin, and for a cube of the equivalent volume as sphere the extracted value of the electric field is the same as that of the sphere. First, we calculate the contribution of the first term by substituting it into the SP expression as follows:

$$\begin{aligned}\mathrm{SP}_1 &= -\frac{1}{j\omega\varepsilon_0}\iiint_{\mathcal{V}} \boldsymbol{\nabla}'\cdot\boldsymbol{J}_{\mathrm{eq}}(\boldsymbol{r}')\frac{(\boldsymbol{r}-\boldsymbol{r}')}{4\pi|\boldsymbol{r}-\boldsymbol{r}'|^3}\,\mathrm{d}V',\\ &= \frac{1}{j\omega\varepsilon_0}\left[\iint_{S+}\cos\theta'\frac{(\boldsymbol{r}-\boldsymbol{r}')}{|\boldsymbol{r}-\boldsymbol{r}'|^3}|\boldsymbol{r}'|^2\sin\theta' d\theta' d\phi' - \iint_{S-}\cos\theta'\frac{(\boldsymbol{r}-\boldsymbol{r}')}{4\pi|\boldsymbol{r}-\boldsymbol{r}'|^3}|\boldsymbol{r}'|^2\sin\theta' d\theta' d\phi'\right].\end{aligned} \tag{8.5}$$

Evaluating the above integral at the centre of the cube as:

$$\begin{aligned}\mathrm{SP}_1|_{\boldsymbol{r}=0} &= \frac{2\pi}{j\omega\varepsilon_0}\left[\int_0^{\pi/2}\cos\theta'\frac{(-\boldsymbol{r}')}{4\pi|\boldsymbol{r}'|^3}|\boldsymbol{r}'|^2\sin\theta' d\theta' d\phi' - \int_{\pi/2}^{\pi}\cos\theta'\frac{(-\boldsymbol{r}')}{4\pi|\boldsymbol{r}'|^3}|\boldsymbol{r}'|^2\sin\theta' d\theta' d\phi'\right],\\ &= \frac{1}{j2\omega\varepsilon_0}\left[\int_0^{\pi/2}\cos\theta'\frac{(-\boldsymbol{r}')}{|\boldsymbol{r}'|}\sin\theta' d\theta' d\phi' - \int_{\pi/2}^{\pi}\cos\theta'\frac{(-\boldsymbol{r}')}{|\boldsymbol{r}'|}\sin\theta' d\theta' d\phi'\right],\\ &= \frac{\hat{\boldsymbol{z}}}{j2\omega\varepsilon_0}\left[-\int_0^{\pi/2}\cos^2\theta'\sin\theta' d\theta' d\phi' + \int_{\pi/2}^{\pi}\cos^2\theta'\sin\theta' d\theta' d\phi'\right],\\ &= \frac{2\hat{\boldsymbol{z}}}{j2\omega\varepsilon_0}\left|\frac{\cos^3\theta}{3}\right|_0^{\pi/2},\\ &= -\frac{\hat{\boldsymbol{z}}}{j\omega 3\varepsilon_0}\end{aligned} \tag{8.6}$$

To calculate the second term in Eq. 8.4, we substitute the second expression in the SP as follows:

$$\begin{aligned}\mathrm{SP}_2 &= -\frac{1}{j\omega\varepsilon_0}\frac{k_0^2}{8\pi}\iiint_{\mathcal{V}} \boldsymbol{\nabla}'\cdot\boldsymbol{J}_{\mathrm{eq}}(\boldsymbol{r}')\frac{(\boldsymbol{r}-\boldsymbol{r}')}{|\boldsymbol{r}-\boldsymbol{r}'|}\,\mathrm{d}V'.\\ &= \frac{2k_0^2}{j\omega\varepsilon_0 8\pi}\left[\iint_{s+}\cos\theta'\frac{(\boldsymbol{r}-\boldsymbol{r}')}{|\boldsymbol{r}-\boldsymbol{r}'|}|\boldsymbol{r}'|^2 sin\theta'\,\mathrm{d}\theta'\,\mathrm{d}\phi'\right].\end{aligned} \tag{8.7}$$

Evaluating the above expression at the centre of the sphere as:

$$\begin{aligned}\mathrm{SP}_2|_{\boldsymbol{r}=0} &= -\frac{4\pi k_0^2 r^2}{j\omega\varepsilon_0 8\pi}\left[\int_0^{\pi/2}\cos\theta'\hat{\boldsymbol{r}'}\sin\theta'\,\mathrm{d}\theta'\right],\\ &= \frac{2k_0^2 r^2}{j\omega\varepsilon_0 4}\left[\int_0^{\pi/2}\hat{\boldsymbol{z}}\cos\theta\sin\theta'\,\mathrm{d}\theta'\right],\\ &= \frac{-k_0^2 r^2}{j\omega 6\varepsilon_0}\hat{\boldsymbol{z}}. \end{aligned} \tag{8.8}$$

In the above equation, the x- and y-components vanish because the field is polarised along the z-axis.

Adding the third Taylor term in the SP results in the following:

$$\begin{aligned}\mathrm{SP}_3 &= \frac{1}{j\omega\varepsilon_0}\frac{jk_0^3}{4\pi}\iiint_{\mathcal{V}}\boldsymbol{\nabla}'\cdot\boldsymbol{J}_{\mathrm{eq}}(\boldsymbol{r}')\frac{(\boldsymbol{r}-\boldsymbol{r}')}{|\boldsymbol{r}-\boldsymbol{r}'|}\,\mathrm{d}V',\\ &= -\frac{2k_0^2}{j\omega 3\varepsilon_0 4\pi}\left[\iint_{s+}\frac{(\boldsymbol{r}-\boldsymbol{r}')}{|\boldsymbol{r}-\boldsymbol{r}'|}|\boldsymbol{r}'|^2 sin\theta'\,\mathrm{d}\theta'\,\mathrm{d}\phi'\right],\\ &= \frac{k_0^3 r^3}{\omega 9\varepsilon_0}\hat{\boldsymbol{z}}. \end{aligned} \tag{8.9}$$

Similarly

$$\mathrm{SP}_4 = \frac{k_0^4 r^4}{j\omega 24\varepsilon_0}\hat{\boldsymbol{z}}. \tag{8.10}$$

Now we one-by-one substitute the first 4 Taylor terms in the VP expression as follows:

$$\begin{aligned}\mathrm{VP}_1|_{\boldsymbol{r}=0} &= -j\omega\mu_0\iiint_{\mathcal{V}}\frac{1}{4\pi|\boldsymbol{r}-\boldsymbol{r}'|}\,\mathrm{d}V',\\ &= -j\omega\mu_0\frac{r^2}{2}\hat{\boldsymbol{z}}. \end{aligned} \tag{8.11}$$

$$\begin{aligned}\mathrm{VP}_2|_{\boldsymbol{r}=0} &= -j\omega\mu_0\iiint_{\mathcal{V}}\frac{-jk_0|\boldsymbol{r}-\boldsymbol{r}'|}{4\pi|\boldsymbol{r}-\boldsymbol{r}'|}\,\mathrm{d}V',\\ &= \frac{-j\omega\mu_0 k_0}{4\pi}\frac{4\pi r^3}{3}\hat{\boldsymbol{z}},\\ &= -\omega\mu_0 k_0\frac{r^3}{3}\hat{\boldsymbol{z}}. \end{aligned} \tag{8.12}$$

$$\mathrm{VP}_3|_{\boldsymbol{r}=0} = -j\omega\mu_0 \iiint_{\mathcal{V}} \frac{-k_0^2|\boldsymbol{r}-\boldsymbol{r}'|^2}{8\pi|\boldsymbol{r}-\boldsymbol{r}'|}\,\mathrm{d}V', \\ = j\omega\mu_0 k_0^2 \frac{r^4}{8}\hat{\boldsymbol{z}}. \tag{8.13}$$

$$\mathrm{VP}_4|_{\boldsymbol{r}=0} = \frac{\omega\mu_0 k_0^3 r^5}{30}\hat{\boldsymbol{z}}. \tag{8.14}$$

Summing all the scalar- and vector-potential terms together, we get:

$$\boldsymbol{E}^{\mathrm{s}}(\boldsymbol{r}, \boldsymbol{J}_{\mathrm{eq}})|_{\boldsymbol{r}=0} = \hat{\boldsymbol{z}}\alpha^{\mathrm{p}} \underbrace{\left[j\omega\mu_0\frac{r^2}{2} - \omega\mu k_0\frac{r^3}{3} + j\omega\mu_0 k_0^2\frac{r^4}{8} + \frac{\omega\mu_0 k_0^3 r^5}{30}\hat{\boldsymbol{z}}\right]}_{\text{VP (Vector Potential) Term}} \\ + \hat{\boldsymbol{z}} \underbrace{\left[-\frac{1}{j\omega 3\varepsilon_0} - \frac{k_0^2 r^2}{j\omega 6\varepsilon_0} - \frac{k_0^3 r^3}{\omega 4\varepsilon_0}\right]}_{\text{SP (Scalar Potential) Term}}. \tag{8.15}$$

We now calculate the total field E^{tot}, the depolarisation factor L, and the effective permittivity from Eq. 5.16.

8.3 Frequency Dependent Effective Properties of Composites

The CM formula provides a dynamic expression to calculate the effective values of a composite, but the MG is an electrostatic expression giving the effective electrostatic values of the permittivity which is sometimes applied at relatively low-frequency regimes. By employing the first terms of the VP and SP in Eq. 8.3, we can calculate a dynamic expression for the MG that can extract the first (dipolar) resonance in the effective-medium model.

The coupling term can be given as:

$$Z = \alpha \left[\frac{1}{j\omega(\varepsilon - \varepsilon_0)} - \frac{1}{j\omega 3\varepsilon_0} - \frac{j\omega\mu_0 r^2}{2} \right], \tag{8.16}$$

$$= \frac{6\varepsilon_0 - 2(\varepsilon - \varepsilon_0) + k^2 r^2 3(\varepsilon - \varepsilon_0)}{j\omega 6\varepsilon_0(\varepsilon - \varepsilon_0)}. \tag{8.17}$$

We take the inverse to calculate the polarisability as:

$$Z^{-1} = \frac{j\omega 6\varepsilon_0(\varepsilon - \varepsilon_0)}{6\varepsilon_0 - 2(\varepsilon - \varepsilon_0) + k^2 r^2 3(\varepsilon - \varepsilon_0)}. \tag{8.18}$$

From the above equation, the normalised polarisability can be given as:

$$\alpha_{\mathrm{n}}^{\mathrm{p}} = \frac{6(\varepsilon - \varepsilon_0)}{6\varepsilon_0 - 2(\varepsilon - \varepsilon_0) + k^2 r^2 3(\varepsilon - \varepsilon_0)}, \tag{8.19}$$

and the scattered field can be given as:

$$E^{\mathrm{s}} = \frac{j\omega 6\varepsilon_0(\varepsilon - \varepsilon_0)}{6\varepsilon_0 - 2(\varepsilon - \varepsilon_0) + k^2 r^2 3(\varepsilon - \varepsilon_0)} \left[\frac{2 - j\omega 3\varepsilon_0(j\omega\mu_0 r^2)}{j\omega 6\varepsilon_0} \right], \tag{8.20}$$

$$= \frac{(\varepsilon - \varepsilon_0)(2 + 3k_0^2 r^2)}{6\varepsilon_0 - 2(\varepsilon - \varepsilon_0) + k^2 r^2 3(\varepsilon - \varepsilon_0)}, \tag{8.21}$$

and the total field is

$$E^{\mathrm{tot}} = \frac{6\varepsilon_0 - 2(\varepsilon - \varepsilon_0) + k^2 r^2 3(\varepsilon - \varepsilon_0) + (\varepsilon - \varepsilon_0)(2 + 3k_0^2 r^2)}{6\varepsilon_0 - 2(\varepsilon - \varepsilon_0) + k^2 r^2 3(\varepsilon - \varepsilon_0)}. \tag{8.22}$$

Substituting the above results in the expression for the effective permittivity given in Chapter 5 as follows:

$$\varepsilon_{\mathrm{eff}} = \frac{f 6(\varepsilon - \varepsilon_0)}{6\varepsilon_0 - 2(\varepsilon - \varepsilon_0) + k^2 r^2 3(\varepsilon - \varepsilon_0) + f(2 + 3k_0^2 r^2)} + 1. \tag{8.23}$$

The above equation is a dynamic expression to calculate the frequency-dependent effective-permittivity of the composite. The closed-form expression is derived using the fundamental wave harmonic only i.e., using a quasi-static approximation, but can well approximate the first (dipolar) resonance. The procedure to calculate the dynamic expression is self-consistent and inherently satisfies Kramers-Kronig

relations. This is in contrast with the work published in the Ref. [118], where only the contribution of the SP was calculated and the contribution from the VP was engineered to satisfy the Kremers-Kronig relations.

The calculated values of the effective parameters have been shown in the Fig. 8.2. Each value of effective permittivity is calculated by adding the consecutively following term in the previous sum. The effective values of the permittivity depend weakly on the angle of incidence when only the dipolar contribution is considered for its calculation; the direction dependence is pronounced when the contribution of higher-order terms is significant.

8.4 Discussion on Frequency-Dependent MG

In a past work by Andrea Alu et al. [118, 122, 123], the SP-terms have been calculated, and the affect of the VP-terms has been engineered using a Lorentz-type addition. One immediate implication of this scheme is that it can not handle lossless inclusions. An additional limitation to the calculation of the effective permittivity is the appearance of grating lobes when the operating wavelength becomes comparable to that of the spacing between the inclusions. The grating lobes cause inaccuracies in the calculation of the effective values of material constitutive parameters. For accuracy of calculations, it is recommended that the wavenumber k be much less than $\pi/d\sin(\theta_{\mathrm{i}})$ for d denoting the period of the lattice and θ_{i} denoting the wave incidence angle.

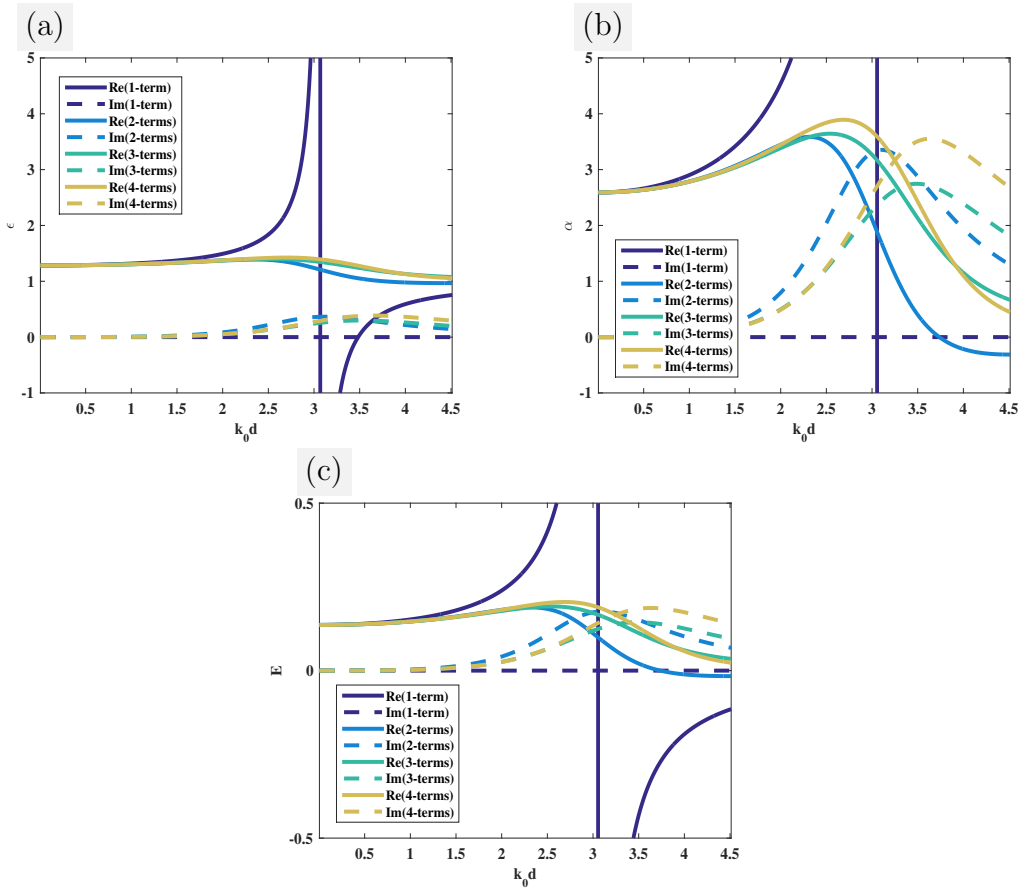

Figure 8.2: Frequency dependent extraction of the effective parameters of a composite composed of a periodic arrangement of scatterers. The radius of the inclusion is 62.035μm; the lattice period is 215.44μm, and the relative permittivity of the inclusions is 20. The matrix is free space. (a) Extracted values of the permittivity (b) Extracted values of the polarisability (c) Extracted values of the electric field inside the inclusion scatterer.

8.5 Summary

The previous chapters focused mainly on the material homogenization in the low-frequency regimes. In this chapter, we focus on the effect of frequency on the effective permittivity of the composites. For the derivation of the effective permittivity of a composite, only the scalar potential term is considered at low frequencies. However, at high frequencies the effect of the vector-potential term is inevitable. Because it is this inevitable relationship between the scalar and vector potential that results in the resonance phenomenon in the dielectric scatterers. The problem with the existing homogenization approaches is that the vector potential term is usually ignored.

Chapter 9

Summary and Future Work

An overview of the major contributions and findings presented in the previous chapters is provided. Key contributions in overcoming the challenges are highlighted. Recommendations to take the study into a further progressive direction are provided.

9.1 Summary

The scope of the thesis has been covered by a detailed review of the literature and by delineating the recent progress in the field. Rigorous modelling and homogenization schemes have been proposed to composite modelling and homogenization, respectively. Certain applications of the composite materials have been proposed.

Theory

The literature about the material homogenization is distributed in different fields, and the description of the different parametric methods is usually discussed in separate research areas. We conducted a systematic literature review of classical and state-of-the-art homogenization techniques and classified them according to their optimal performance in particular frequency regimes.

Modelling

2D- and 3D-material modelling schemes have been presented. The volume-equivalence principle was employed to represent the electric field integral equation in a weak form, and the pulse-shaped basis was used for discretizing the geometry of the problem. The self-term in the 2D case was evaluated analytically, and the cross-coupling terms were calculated by representing the cylinder's field in terms of a Hankel function. In 3D case, the sphere singularity is evaluated analytically using only the fundamental term in the wave function (quasi-static approximation), while the contribution of cross-coupling terms was calculated by representing the field scattered by a sphere as that of scattered by a dipole placed at the centre of the sphere.

A rigorous analytical scheme is proposed for the material homogenization. The scheme coincides with the available analytical closed-form expressions for 2D- and 3D-material homogenisation in electrostatics. Also, we derived analytical expressions from extracting the dispersive properties of the homogenised materials that can calculate the first resonance in spherical dielectric inclusions in a composite. The Maxwell-Garnett and Clausius-Mossotti formulas have wrongly been assumed to account for the coupling between the inclusions in a composite; the proposed self-

consistent derivations dispelled those claims. The proposed 3D-modelling scheme accounted for the exact calculations of the coupling between the inclusions, and the effect of coupling was compared to that of non-coupled inclusions in a composite for the material homogenization.

Applications

Several electromagnetic applications of the proposed material modelling and material design schemes have been proposed such as the simulation of finite-sized electrically small and large structures. Lüneburg lens has been designed based on the composites both in the 2D and 3D, and the exact structure of the lens has been simulated both in 2D and 3D. An absorbing material has been designed, based on the Lüneburg lens, for the reduction of electromagnetic interfere. Maxwell's Fisheye has been designed based on composites in 2D, and its operation has been demonstrated by simulating it for imaging functionality. Besides, a rigorous closed-form expression has been proposed for the extraction of dipolar resonance in spherical inclusions in composites.

9.2 Key Contribution

The technical contributions are the following:

- Classified various homogenization schemes according to their applicability in the respective material state and the frequency of operation.
- 2D-material modelling based on the cylindrical scatterer as a basis. The inclusion cylinders can be located according to a given distribution function.

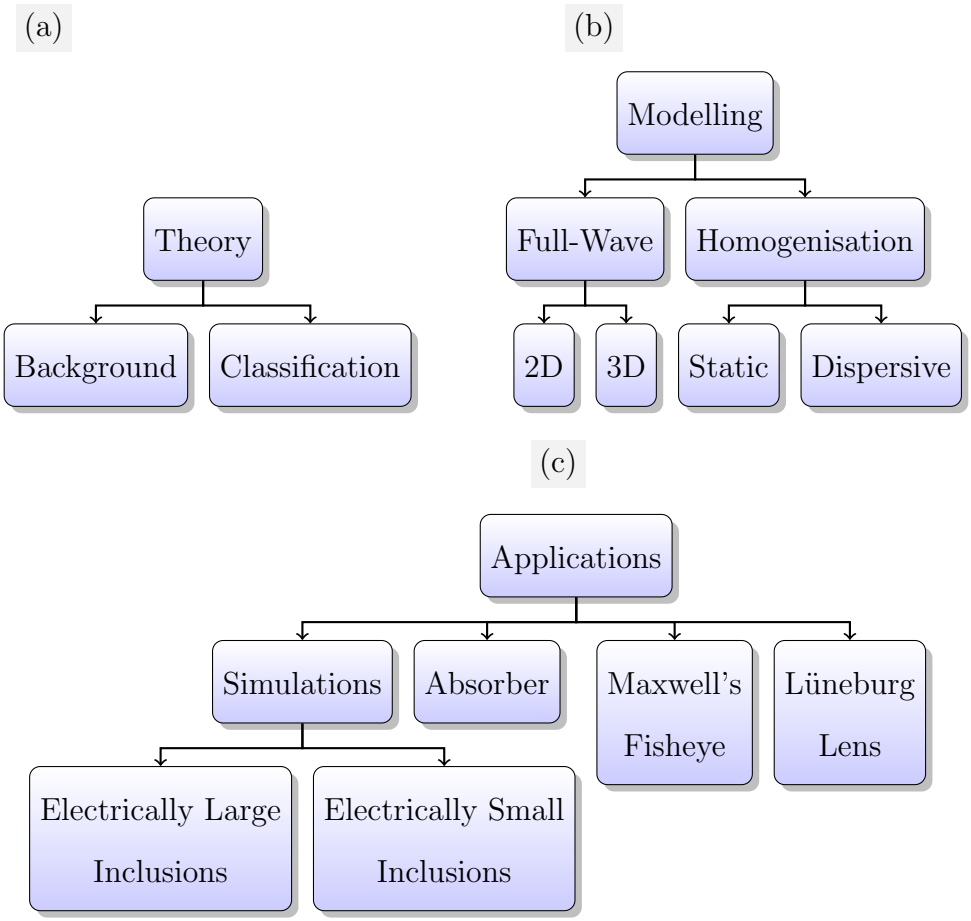

Figure 9.1: Theory, modelling, and applications of advanced electromagnetic materials. (a) The background of the problem has been discussed, and the material homogenization schemes have been classified based on their applications in the specified frequency regime (b) Rigorous modelling and homogenization schemes have been proposed to composite modelling and homogenization, respectively (c) The applications of the material modelling and design schemes.

- 3D-material modelling based on the spherical scatterer as a basis. The inclusion spheres can be located in 3D based on a given distribution function.
- Simulation time and storage requirement of scatterer-based composites were improved both in 2D- and 3D-modelling schemes.
- 2D-material homogenization method. A rigorous mathematical procedure was followed to derive a homogenization scheme based on circular cylindrical inclusions.
- 3D-material homogenization procedure. A rigorous mathematical procedure was followed to derive a homogenization scheme based on both the cubic as well as spherical scatterers as inclusions.
- Dispersive modelling of 3D composite materials. The generalised expression for the effective permittivity in terms of the polarizability of the inclusions was derived, where the expression for the polarizability of the inclusion was based on the fundamental harmonics of both the scalar and vector potentials. The resultant closed-form expression resulted in the calculation of the dispersion properties of the effective permittivity.
- Applications:
  - 3D-modelling of composites consisting of a large number of spherical inclusions.
  - 2D-modelling of composites consisting of a large number of cylindrical inclusions.
  - Simulating finite-sized and electrically large structures composed of arbitrarily shaped inclusions.
  - Lüneburg lens design using composite layers' modelling of indexed lens design.

- Absorber design based on lossy Lüneburg lens designed using composite layers' modelling.
- Maxwell's Fisheye design using composite layers' modelling of indexed lens design.

9.3 Future Work

The following extensions to the presented work are possible:

- The material modelling scheme can be extended to include various types of inclusions as a basis such as spheroids, rectangles, and tetrahedra.
- Coupled-field (electric and magnetic) model can be introduced to homogenise magneto-dielectric materials accurately. The coupling between both the electric and magnetic dipolar fields in the moment matrix would be required for this purpose.
- The proposed applications can be manufactured, and the proposed features can be measured.
- The proposed dipole-moment-based modelling method can be extended for the analysis of periodic geometries that are infinite in extent in one- or two-dimensions. The extension could be achieved by employing a periodic version of the free-space Green's function in the formulation of the method. The method could further be extended to include arbitrarily shaped unit vectors by the application of the characteristic basis function method.

In addition to the above mentioned suggestions to take the study into a forward direction, the following devices are proposed to be designed and manufactures for various industrial applications.

9.3.1 Beam Focusing Device for Energy Harvesting

A photovoltaic cell operations by the incidence of photons on the n-type region of a photovoltaic cell. However, the efficiency of the device is limited due to the reflection of the incident light off the surface of the coating layer that is used to protect the cell against ambient weather. The light incident on the electrodes of the cell results in reflection of light instead of absorption, which further limits the cell efficiency. Also, a smaller electrode width would be bad for collecting the photo-generated carriers because of a smaller collection area for collecting carriers [124]. We propose to overcome these problems by employing a cylindrical Lüneburg lens with its focus on the region between the electrodes and, hence, covering the electrodes. The proposed lens design overcomes both the issues: First, the lens collects the energy incident on it and focuses it on one line; second, it staves off reflection from electrodes by covering the cell with the lens. It also mitigates the reflection of the covering layer of the cell because the outer lens layer can be matched to that of the coating. However, because the sunlight is unpolarized, the polarization component of the incident light that is not parallel to the cylindrical lenses would be uncontrolled.

9.3.2 Radiation Shielding Box

As discussed in Section 5.4 of Chapter 5, a 2D Lüneburg-lens-based cylinders can be used for stitching the periphery of a printed circuit board for the absorption of the field incident on it. Also, an array of Lüneburg-lens-based cylinders would result in complete absorption of the perpendicular incident waves, if the polarization is parallel to the lenses. However, a 3D version of the Lüneburg lens can be used to build a Faraday cage that could absorb the field incident on it from any direction and independent of the polarisation of the incident wave. An array of Lüneburg lens can be manufactured with the shielding box of the electronic device to function as

an absorber. A schematic of the proposed shielding scheme based on 3D Lüneburg lenses is shown in Fig. 9.3

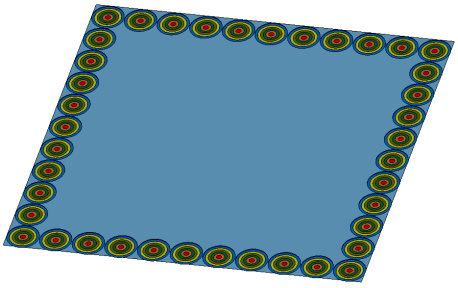

Figure 9.2: A single layer of absorbing Lüneburg lenses stitching the periphery of the printed circuit board. For better operation of the device the separation between the lenses is less than a quarter the operating wavelenth

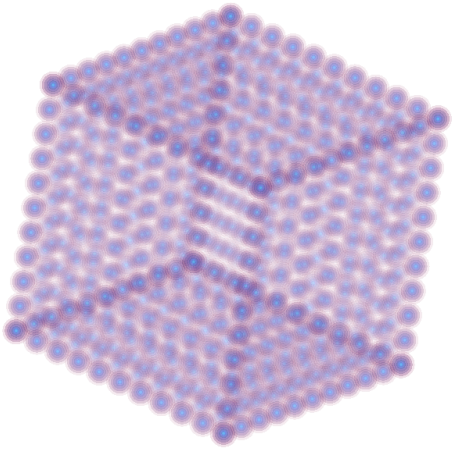

Figure 9.3: A single layer of array of absorbing 3D Lüneburg lenses. The device can absorb any polarization incident on it from any direction. It isolates the internal electronic circuitry from outside and vice versa.

Bibliography

[1] A. M. NICOLSON and G. F. ROSS, "Measurement of the intrinsic properties of materials by time-domain techniques," *IEEE Trans. on Instrumentation and Measurement*, vol. IM-19, no. 4, 1970.

[2] V. G. Veselago, "The electrodynamics of substances with simultaneously negative values of ε and μ," *Soviet Physics Uspekhi*, vol. 10, no. 4, 1968.

[3] J. B. Pendry, A. J. Holden, D. J. Robbins, and W. J. Stewart, "Magnetism from conductors and enhanced nonlinear phenomena," *IEEE Transactions on Microwave Theory and Techniques*, vol. 47, no. 11, 1999.

[4] D. R. Smith, W. J. Padilla, D. C. Vier, S. C. Nemat-Nasseer, and S. Schultz, "Composite medium with simultaneously negative permeability and permittivity," *Physical Review Letters*, vol. 84, no. 18, 2000.

[5] S. O'Brien and J. B. Pendry, "Photonic band-gap effects and magnetic activity in dielectric composites," *Journal of Physics: Condensed Matter*, vol. 14, no. 4035, 2002.

[6] Q. Zhao, L. Kang, B. Du, H. Zhao, Q. Xie, X. Huang, B. Li, J. Zhou, and L. Li, "Experimental demonstration of isotropic negative permeability in a three-dimensional dielectric composite," *Physical Review Letters*, vol. 101, no. 027402, 2008.

[7] Q. Zhao, J. Zhou, F. Zhang, and D. Lippens, "Mie resonance-based dielectric metamaterials," *materialstoday*, vol. 12, no. 12, 2009.

[8] D. R. Smith and J. B. Pendry, "Homogenization of metamaterials by field averating," *Optical Society of America*, vol. 23, no. 3, 2006.

[9] J. B. Pendry and D. R. Smith, "Reversing Light With Negative Refraction," pp. 37–43, June 2004.

[10] J. B. Pendry, D. Schurig, and D. R. Smith, "Controlling Electromagnetic Fields," *Science*, vol. 312, no. 5781, pp. 1780–1782, Jun. 2006.

[11] ——, "Controlling electromagnetic fields," *Science*, vol. 312, 2006.

[12] J. B. Pendry, A. Aubry, D. R. Smith, and S. A. Maier, "Transformation optics and subwavelength control of light," *Science*, vol. 337, 2012.

[13] D. Schurig, J. J. Mock, B. J. Justice, S. A. Cummer, J. B. Pendry, A. F. Starr, and D. R. Smith, "Metamaterial electromagnetic cloak at microwave frequencies," *Science*, vol. 314, 2006.

[14] O. Q.-Teruel, W. Tang, R. C. M.-Thomas, A. Dyke, H. Dyke, L. Zhang, S. Haq, and Y. Hao, "Transformation optics for antennas: Why limit the bandwidth with metamaterials?" *Scientific Reports*, vol. 3, no. 1903, 2013.

[15] H. Raether, "Surface plasmons on smooth and rough surfaces and on gratings," *Springer Tracts in Modern Physics*, vol. 111, 1986.

[16] A. E. Miroshnichenko, "Fano resonance in nanoscale structures," *Reviews of Modern Physics*, vol. 82, 2010.

[17] R. Sardar, A. M. Funston, P. Mulvaney, and R. W. Murray, "Gold naoparticles: Past, present and future," *Langmuir Perspective*, vol. 25(24), pp. 13 840–13 851, Jun. 2009.

[18] S. Kubo, A. Diaz, Y. Tang, and T. S. Mayer, "Tunability of the refractive index of gold nanoparticle dispersions," *Nano Letters*, vol. 7, no. 11, pp. 3418–3423, Oct. 2007.

[19] Z. Qian, "Augmented surface integral equation method for low-frequency electromagnetic analysis," Ph.D. dissertation, 2009.

[20] V. Myroshnychenko, J. R.-Fernandez, I. P.-Santos, A. M. Funston, C. Novo, P. Muvaney, L. M. L.-Marzan, and F. J. G. de Abajo, "Modelling the optical response of gold nanoparticles," *Chem. Soc. Rev.*, vol. 37, pp. 1792–1805, Jul. 2008.

[21] L. Brillouin, *Wave Propagation and Group Velocity*, 1st ed. Academic Press, 1960.

[22] C. Kittel, *Introduction to Solid State Physics*, 8th ed. John Wiley and Sons, 2005.

[23] K.-H. D. C. O. A. L. Tsang, J. A. Kong, *Scattering of Electromagnetic Waves: Numerical Simulations*, 1st ed. John Wiley and Sons, 2001.

[24] D. Stroud, "The effective medium approximations: Some recent developments," *Superlattices and Microstructures*, vol. 23, no. 3/4, pp. 567–573, Nov. 1998.

[25] J. C. M. Garnett, "Colours in metal glasses and metal films," *Philos. Trans. R. Soc. London, Sect A*, vol. 3, pp. 385–420, 1904.

[26] S. Bosch, J. F.-Borrull, N. Leinfellner, and A. Canillas, "Effective dielectric function of mixtures of three or more materials: A numerical procedure for computations," *Surface Science*, vol. 453, pp. 9–17, Feb. 2000.

[27] M. Y. Koledintseva, R. E. DuBroff, and R. W. Schwartz, "A maxwell garnett

model for dielectric mixtures containing conducting particles at optical frequencies," *Progress in Electromagnetics Research*, vol. 63, pp. 223–242, 2006.

[28] L. Lewin, "The electrical constants of a material loaded with spherical particles," *Electrical Engineers - Part III: Radio and Communication Engineering, Journal of the Institution of*, vol. 94, no. 27, pp. 65–68, January 1947.

[29] L. Taylor, "Dielectric properties of mixtures," *Antennas and Propagation, IEEE Transactions on*, vol. 13, no. 6, pp. 943–947, Nov 1965.

[30] W. R. Tinga, W. A. G. Voss, and D. F. Blossey, "Generalized approach to muliphase dielectric mixture theory," *J. Appl. Phys.*, vol. 44, no. 9, pp. 3897–3902, Jan. 1973.

[31] A. H. Sihvola and J. A. Kong, "Effective permittivity of dielectric mixtures," *IEEE Trans. on Geoscience and Remote Sensing*, vol. 26, no. 4, pp. 420–429, Jul. 1988.

[32] A. Sihvola, *Electromagnetic Mixing Formulas and Applications*. Electromagnetic Waves Series, 1999, vol. 47.

[33] D. Bruggeman, "Berechnung verschiedener physikalischer konstanten von heterogenen substanzen: I dielektrizittskonstanten und leitfhigkeiten der mischkrper aus isotropen substanzen," *Annalen der Physik*, vol. 24, pp. 636–664, 1935.

[34] J. P. Calame, A. Birman, Y. Carmel, D. Gershon, B. Levush, A. A. Sorokin, V. E. Semenov, D. Dadon, L. P. Martin, and M. Rosen, "A dielectric mixing law for porous ceramics based on fractal boundaries," *Journal of Applied Physics*, vol. 80, no. 7, pp. 3992–4000, Oct. 1996.

[35] J. P. Calame, "Evolution of davidson-cole relaxation behavior in random conductor-insulator composites," *Journal of Applied Physics*, vol. 94, no. 9, pp. 5945–5957, Nov. 2003.

[36] A. Nussbaum, *Electromagnetic and quantum properties of materials.* Englewood Cliffs N.J.: Prentice-Hall, 1966.

[37] D. E. Aspnes, "Local-field effects and effective-medium theory: A microscopic perspective," *American Journal of Physics*, vol. 50, no. 8, p. 704, 1982.

[38] K. Tsang, Leung, Jin Au, Kong, *Scattering of Electromagnetic Waves, Theories and Applications.* New York: Wiley, 2000.

[39] J. C. Maxwell Garnett, "Colours in Metal Glasses and in Metallic Films," *Transactions of the Royal Society*, vol. CCIII, pp. 385–420, 1904.

[40] E. F. Kuester, M. A. Mohamed, M. P.-May, and C. L. Holloway, "Averaged transition conditions for electromagnetic fields at a metafilm," *IEEE Trans. on Antennas and Propagation*, vol. 51, no. 10, pp. 2641–2651, Oct. 2003.

[41] C. L. Holloway, M. A. Mohamed, E. F. Kuester, and A. Dienstfrey, "Reflection and transmission properties of a metafilm: With an application to a controllable surface composed of resonant particles," *IEEE Trans. on Electromagnetic Compatibility*, vol. 47, no. 4, pp. 853–865, Nov. 2005.

[42] C. L. Holloway, A. Dienstfrey, E. F. Kuester, J. F. O'Hara, A. K. Azad, and A. J. Taylor, "A discussion on the interpretation and characterization of metafilms/metasurfaces: The two-dimensional equivalent of metamaterials," *Metamaterials (Elsvier)*, vol. 3, pp. 100–112, Aug. 2009.

[43] C. L. Holloway, D. C. Love, E. F. Kuester, J. A. Gordon, and D. A. Hill, "Use of generalized sheet transition conditions to model guided waves on metasurfaces/metafilms," *IEEE Trans. on Antennas and Propagation*, vol. 60, no. 11, pp. 5173–5186, Nov. 2012.

[44] C. L. Holloway, E. F. Kuester, J. A. Gordon, J. O'Hara, J. Booth, and D. R. Smith, "An overview of the theory and applications of metasurfaces: The two-

dimensional equivalents of metamaterials," *IEEE Antennas and Propagation Magazine*, vol. 54, no. 2, pp. 10–35, Apr. 2012.

[45] A. K. Jonscher, *Dielectric Relaxation in Solids*, 1st ed. Chelsea Dielectric Press, London, 1983.

[46] P. Debye, *Polar Molecules*, 1st ed. The Chemical Catalog Company, Inc., 1929.

[47] A. Von Hippel, *Dielectrics and waves*. New York ;London: Wiley;;Chapman & Hall, 1954.

[48] K. S. Cole and R. H. Cole, "Diespersion and absorption in dielectrics i. alternating current characteristics," *The Journal of Chemical Physics*, vol. 9, 341, pp. 341–351, 1941.

[49] D. W. Davidson and R. H. Cole, "Dielectric relaxation in glycerol, propylene glycol, and n-propanol," *The Journal of Chemical Physics*, vol. 19, no. 12, pp. 1484–1490, 1951.

[50] S. Havriliak and S. Negami, "A complex plane representation of dielectric and mechanical relaxation processes in some polymers," *Polymer*, vol. 8, pp. 161–210, 1967.

[51] J. H. Calderwood, "A physical hypothesis for cole-davidson behavior," *IEEE Transactions on Dielectric and Electrical Insulation*, vol. 10, no. 6, pp. 1006–1011, 2003.

[52] A. K. Jonscher, "The universal dielectric response," *Nature*, vol. 267, pp. 673–679, Jun. 1977.

[53] V.-T. Truong, A. R. Codd, and M. Forsyth, "Dielectric properties of conducting polymer composites at microwave frequencies," *Journal of Materials Science*, vol. 29, pp. 4331–4338, 1994.

[54] V.-T. Truong and G. Ternan, "Complex conductivity of a conducting polymer composite at microwave frequencies," *Polymer*, vol. 36, no. 5, pp. 905–909, 1995.

[55] D. P. Almond and B. Vainas, "The dielectric properties of random r-c networks as an explanation of the universal power law dielectric response of solids," *J. Phys.: Condens. Matter*, vol. 11, pp. 9081–9093, 1999.

[56] C. R. Bowen and D. P. Almond, "Modelling the universal dielectric response in heterogeneous materials using microstructural electrical networks," *Materials Science and Techonology*, vol. 22, no. 6, pp. 719–724, 2006.

[57] R. E. Hummel, *Electronic Properties of Materials*, 4th ed. Springer, 2011.

[58] H. M. H. M. Nussenzveig, *Causality and dispersion relations*. New York : Academic Press, 1972.

[59] M. L. Brongersma, J. W. Hartman, and H. A. Atwater, "Electromagnetic energy transfer and switching in nanoparticle chain arrays below the difraction limit," *Physical Review B*, vol. 62, no. R16356, 2000.

[60] E. O. Reilly, *Quantum Theory of Solids*. Masters Series in Physics and Astronomy, 2002, vol. 47.

[61] A. Bondeson, T. Rylander, and P. Ingelstrom, *Computational Electromagnetics*. Springer, 2005.

[62] M. N. O. Sadiku, *Numerical Techniques in Electromagnetics*, 2nd ed. CRC Press, 2001.

[63] D. G. Swanson, J. Wolfgang, and J. R. Hoefe, *Microwave Circuit Modeling Using Electromagnetic Field Simulation*. Artech House Boston, London, 2003.

[64] M. Naeem, "Scattering and absorption analysis of radomes using the method of equivalent dipole moments," 2011.

[65] K. S. Yee, "Numerical solution of initial boundary value problems involving maxwell's equations in isotropic media," *IEEE Trans. Antennas Propag.*, vol. AP-14, no. 3, May 1966.

[66] R. F. Harrington, *Field Computation by Moment Methods.* New York: The MacMillan Company, 1968.

[67] S. I. Bozhevolnyi and V. S. Volkov, "Multiple-scattering dipole approach to modeling of surface plasmon polariton band gap structures," *Optics Communications*, vol. 198, pp. 241–245, 2001.

[68] M. Naeem, R. Maaskant, G. W. Kant, P. Kildal, and R. Mittra, "The method of equivalent dipole moments (medm) combined with cbfm for the fast and accurate solution of dielectric scattering problems," *Electromagnetics in Advanced Applications (ICEAA), 2011 International Conference on*, Sep. 2011.

[69] R. Maaskant, R. Mittra, and A. Tijhuis, "Fast analysis of large antenna arrays using the characteristic basis function method and the adaptive cross approximation algorithm," *IEEE Trans. Antennas Propag.*, vol. 56, no. 11, 2008.

[70] V. V. Prakash and R. Mittra, "Characteristic basis function mehod: A new technique for efficient solution of method of moments matrix equations," *Microwave and Optical Technology Letters*, vol. 36, no. 2, Jan. 2003.

[71] R. Maaskant, R. Mittra, and A. Tijhuis, "Fast analysis of large antenna arrays using the characteristic basis function method and the adaptive cross approximation algorithm," *IEEE Trans. Antennas Propag.*, vol. 56, no. 11, 2008.

[72] T. Dong, X. Ma, and R. Mittra, "Modeling large non-uniform optical antenna arrays for metasurface application," *Journal of Applied Physics*, vol. 114, no. 043103, 2013.

[73] J. H. Richmond, "Scattering by a Dielectric Cylinder of Arbitrary Cross Section Shape," vol. 33, no. 616, 1964.

[74] A. F. Peterson, S. L. Ray, and R. Mittra, *Computational Methods for Electromagnetics*. New York NY: IEEE Press, 1998.

[75] M. KERKER, *The Scattering of Light and Other Electromagnetic Radiation*. New York and London: Elsevier, 1969.

[76] F. J. Garc, "Effective Medium Theory of the Optical Properties of Aligned Carbon Nanotubes," pp. 4289–4292, 1997.

[77] F. Shahzad, M. Alhabeb, C. B. Hatter, B. Anasori, S. Man Hong, C. M. Koo, and Y. Gogotsi, "Electromagnetic interference shielding with 2D transition metal carbides (MXenes)," *Science*, vol. 353, no. 6304, pp. 1137–1140, 2016.

[78] G. E. Moore, "Cramming more components onto integrated circuits (Reprinted from Electronics, pg 114-117, April 19, 1965)," *Proceedings Of The Ieee*, vol. 86, no. 1, pp. 82–85, 1965.

[79] X. Ye, D. M. Hockanson, M. Li, Y. Ren, W. Cui, J. L. Drewniak, and R. E. Dubroff, "EMI Mitigation With Multilayer Power-Bus Stacks and via Stitching of Reference Planes," vol. 43, no. 4, pp. 538–548, 2001.

[80] Y.-j. Zhang, G. Feng, J. Fan, and S. Member, "A Novel Impedance Definition of a Parallel Plate Pair for an Intrinsic Via Circuit Model," vol. 58, no. 12, pp. 3780–3789, 2010.

[81] S. Jain, M. Abdel-mageed, and R. Mittra, "Flat-Lens Design Using Field Transformation and Its Comparison With Those Based on Transformation Optics and Ray Optics," *IEEE Antennas and Wireless Propagation Letters*, vol. 12, pp. 4–7, 2013.

[82] J. Liu, R. Mendis, and D. M. Mittleman, "A Maxwell's fish eye lens for the terahertz region," *Applied Physics Letters*, vol. 103, no. 3, 2013.

[83] R. Mendis and D. M. Mittleman, "Artificial dielectrics," *IEEE Microwave Magazine*, vol. 15, no. 7, pp. 34–42, 2014.

[84] S. Kubo, A. Diaz, Y. Tang, T. S. Mayer, I. C. Khoo, and T. E. Mallouk, "Tunability of the refractive index of gold nanoparticle dispersions," *Nano Letters*, vol. 7, no. 11, pp. 3418–3423, 2007.

[85] C. Della Giovampaola and N. Engheta, "Digital Metamaterials," *Nature Materials*, vol. 13, no. September, pp. 1115–1121, 2014.

[86] R. D. Graglia, "On the numerical integration of the linear shape functions times the 3-D Green's function or its gradient on a plane triangle," vol. 41, no. 10, pp. 1448–1455, Oct. 1993.

[87] a. M. Nicolson and G. F. Ross, "Measurement of the Intrinsic Properties of Materials by Time-Domain Techniques," *IEEE Transactions on Instrumentation and Measurement*, vol. 19, no. 4, 1970.

[88] X. Chen, T. M. Grzegorczyk, B.-I. Wu, J. Pacheco, and J. A. Kong, "Robust method to retrieve the constitutive effective parameters of metamaterials," *Phys. Rev. E*, vol. 70, p. 016608, Jul 2004.

[89] S. Guenneau and F. Zolla, "Homogenization of Three-Dimensional Finite Photonic Crystals," *Progress in Electromagnetics Research*, no. PIER 27, pp. 91–127, 2000.

[90] R. F. Harrington, *Time-Harmonic Electromagnetic Fields*. New Jersey: IEEE Press, 2001.

[91] C. A. Grimes, "The effective permeability of granular thin films," *IEEE Transactions on Magnetics*, vol. 29, pp. 4092–4094, November 1993.

[92] R. K. Luneburg and H. Max, *Mathematical theory of optics*. Brown University, 1944.

[93] H. F. Ma and T. J. Cui, "Three-dimensional broadband and broad-angle transformation-optics lens," *Nature Communications*, vol. 1, no. 8, pp. 124–127, 2010.

[94] N. Kundtz and D. R. Smith, "Extreme-angle broadband metamaterial lens," *Nature Materials*, vol. 9, no. 2, pp. 129–132, 2009.

[95] J. Li and J. B. Pendry, "Hiding under the Carpet : A New Strategy for Cloaking," *Physical Review Letters*, vol. 203901, no. November, pp. 1–4, 2008.

[96] M. Naeem and Y. Hao, "Homogenization of composites using full-wave point-dipole model," *EPJ Appl. Metamat*, vol. 3, 2016.

[97] A. Demetriadou and Y. Hao, "Slim Luneburg lens for antenna applications," vol. 19, no. 21, pp. 211–219, 2011.

[98] A. Demetriadou, Y. Hao, and S. Member, "A Grounded Slim Luneburg Lens Antenna Based on Transformation Electromagnetics," *IEEE Antennas and Propagation Letters*, vol. 10, pp. 1590–1593, 2011.

[99] C. Mateo-segura, A. Dyke, H. Dyke, S. Haq, and Y. Hao, "Flat Luneburg Lens via Transformation Optics for Directive Antenna Applications," vol. 62, no. 4, pp. 1945–1953, 2014.

[100] R. Yang, W. Tang, and Y. Hao, "A broadband zone plate lens from transformation optics," vol. 19, no. 13, pp. 12 348–12 355, 2011.

[101] S. Rondineau, M. Himdi, and J. Sorieux, "A Sliced Spherical Lüneburg Lens," *IEEE Antennas and Propagation Letters*, vol. 2, pp. 163–166, 2003.

[102] E. Akmansoy, F. Gaufillet, and E. Akmansoy, "Graded Photonic Crystals for Luneburg Lens," *IEEE Photonics Journal*, vol. 8, no. 1, 2016.

[103] M. Liang, S. Member, W.-r. Ng, K. Chang, K. Gbele, M. E. Gehm, H. Xin, and S. Member, "A 3-D Luneburg Lens Antenna Fabricated by Polymer Jetting Rapid Prototyping," *IEEE Transactions on Antennas and Propagation*, vol. 62, no. 4, pp. 1799–1807, 2014.

[104] B. Vasić and R. Gajić, "Tunable gradient refractive index optics using graded plasmonic crystals with semiconductor rods," *J. Opt. Soc. Am. B*, vol. 29, pp. 79–87, 2012.

[105] Y.-y. Zhao, Y.-l. Zhang, M.-l. Zheng, and X.-z. Dong, "Three-dimensional Luneburg lens at optical frequencies," *Laser Photonics Rev.*, vol. 672, no. 4, pp. 665–672, 2016.

[106] Y. Li and Q. Zhu, "Luneburg lens with extended flat focal surface for electronic scan applications," *OPTICS EXPRESS*, vol. 24, no. 7, pp. 1706–1713, 2016.

[107] M. T. Sebastian, *Dielectric Materials for Wireless Communication.* Elsevier, 2008.

[108] M. V. Rybin, D. S. Filonov, K. B. Samusev, P. a. Belov, Y. S. Kivshar, and M. F. Limonov, "Phase diagram for the transition from photonic crystals to dielectric metamaterials," *Nature Communications*, vol. 6, no. May, pp. 1–6, 2015.

[109] V. Myroshnychenko, J. Rodríguez-Fernández, I. Pastoriza-Santos, A. M. Funston, C. Novo, P. Mulvaney, L. M. Liz-Marzán, and F. J. García de Abajo, "Modelling the optical response of gold nanoparticles." *Chemical Society reviews*, vol. 37, no. 9, pp. 1792–1805, 2008.

[110] T. Driscoll, G. Lipworth, J. Hunt, N. Landy, N. Kundtz, D. N. Basov, and F. Zolla, "Performance of a three dimensional transformation-optical-flattened Luneburg lens," *OPTICS EXPRESS*, vol. 20, pp. 13 262–13 273, 2012.

[111] J. Valentine, J. Li, T. Zentgraf, G. Bartal, and X. Zhang, "An optical cloak made of dielectrics," *Nature Materials*, vol. 8, no. 7, pp. 568–571, 2009.

[112] D. Schurig, J. J. Mock, B. J. Justice, S. A. Cummer, J. B. Pendry, A. F. Starr, and D. R. Smith, "Reports 7." *Science*, vol. 11186, no. 2003, 2005.

[113] Q. Zhao, J. Zhou, F. Zhang, and D. Lippens, "Mie resonance-based dielectric metamaterials," *Materials Today*, vol. 12, no. 12, pp. 60–69, 2009.

[114] W. C. Chew, "Computational electromagnetics : smooth versus oscillatory fields," *The Royal Society*, vol. 362, no. 1816, pp. 579–602, 2010.

[115] J. Bladel, "Electromagnetic fields," Hoboken, N.J. :;[Chichester] :, 2007.

[116] L. Brillouin, *Wave propagation and group velocity.* New York: Academic Press, 1960.

[117] C. Kittel, *Introduction to solid state physics.* Hoboken NJ: Wiley, 2004.

[118] A. Alù, A. D. Yaghjian, R. a. Shore, and M. G. Silveirinha, "Causality relations in the homogenization of metamaterials," *Physical Review B - Condensed Matter and Materials Physics*, vol. 84, no. 5, pp. 1–16, 2011.

[119] A. Alù, "First-principles homogenization theory for periodic metamaterials," *Physical Review B - Condensed Matter and Materials Physics*, vol. 84, no. 7, pp. 1–18, 2011.

[120] S. A. Tretyakov and A. J. Viitanen, "Plane waves in regular arrays of dipole scatterers and effective-medium modeling," *J. Opt. Soc. Am. A*, vol. 17, no. 10, pp. 1791–1797, Oct 2000.

[121] S. Tretyakov, *Analytical Modeling in Applied Electromagnetics*, ser. Artech House electromagnetic analysis series. Artech House, 2003.

[122] A. Alù, "Restoring the physical meaning of metamaterial constitutive parameters," *Physical Review B*, vol. 83, no. 8, p. 081102, Feb. 2011.

[123] X.-x. Liu and A. Al, "Generalized retrieval method for metamaterial constitutive parameters based on a physically driven homogenization approach," vol. 235136, pp. 1–7, 2013.

[124] M. H. Juang, H. Y. Huang, and S. L. Jang, "Effects of contact electrode size on the characteristics of polycrystalline-Si p i n solar cells," vol. 32, no. 3, pp. 3–6, 2011.

[125] J. A. Stratton, *Electromagnetic Theory*. McGRAW-HILL, 1941.

[126] C. A. Balanis, *Advanced Engineering Electromagnetics*. New York: John Wiley and Sons, Inc., 1989.

[127] S. M. Rao and D. R. Wilton, "Electromagnetic scattering by surfaces of arbitrary shape," *IEEE Trans. Antennas Propag.*, vol. AP-30, no. 3, May 1982.

[128] R. Maaskant, "Analysis of large antenna systems," Ph.D. dissertation, Eindhoven University of Technology, 2010.

[129] R. F. Harrington, *Time-Harmonic Electromagnetic Fields*. McGRAW-HILL, 1961.

[130] B. A. Finlayson, *The Method of Weighted Residuals and Variational Principles With Applications in Fluid Mechanics, Heat and Mass Transfer*. Academic Press, INC, 1972, vol. 87.

[131] T. K. Sarkar, A. R. Djordjevic, and E. Arvas, "On the choice of expansion and weighting functions in the numerical solution of operator equations," *IEEE Trans. Antennas Propag.*, vol. AP-33, no. 9, Sep. 1985.

[132] J. S. and, "Direct solvers for the second and fourth order equations using legendre polynomials," *SIAM J. Sci. Comp.*, no. 15, pp. 1489–1505, 1994.

[133] P. E. Gill, W. Murray, and M. H. Wright, *Practical Optimization.* Academic Press, INC, 1981.

[134] T. K. Sarkar, "A note on the choice weighting functions in the method of moments," *IEEE Trans. Antennas Propag.*, vol. AP-33, no. 4, Apr. 1985.

[135] D. R. Wilton, S. M. Rao, A. W. Glisson, D. H. Schaubert, O. M. Al-Bundak, and C. M. Butler, "Potential integrals for uniform and linear source distributions on polygonal and polyhedral domains," vol. 32, no. 3, pp. 276–281, Mar. 1984.

[136] J. F. White, *HIGH FREQUENCY TECHNIQUES—An Introduction to RF and Microwave Engineering.* John Wiley & Sons, Inc., 2004.